UNIVERSITY OF CALIFORNIA
RIVERSIDE

A Novel Surface Plasmon Polaritons (SPPs) Induced Near-Field Raman Spectroscopy Imaging Technique Performed by Ultra-Sharp Tip Silver Nanowires (AgNWs)

A Dissertation submitted in partial satisfaction
of the requirements for the degree of

Doctor of Philosophy

in

Electrical Engineering

by

Xuezhi Ma

September 2019

Dissertation Committee:
Dr. Ming Liu, Chairperson
Dr. Jianlin Liu
Dr. Albert Wang

The Dissertation of Xuezhi Ma is approved:

_____

_____

_____

Committee Chairperson

University of California, Riverside

Acknowledgments

I would like to express my gratitude to my research advisor, Dr. Ming Liu, wholeheartedly, for his academic mentorship and constant supports during my Ph.D. studies. His visions in electrical engineering and research advice have guided me throughout my Ph.D. research activities. The beauty, the majesty, the power of his physical image lighted up my academic career. It's been a great pleasure and fortune for me to have him as my advisor.

I would like to thank the Department of Electrical and Computer Engineering at University of California, Riverside, especially the members of my dissertation committee, Dr. Jianlin Liu, and Dr. Albert Wang, for their support on my dissertation research. I would like to thank all my laboratory mates with whom I have conducted research together, Qiushi Liu, Sanggon Kim, Peter Bryler, Yangzhi Zhu, Da Xu, Ning Yu, Leonard Apontti, Yaodong Xu, and Boqun Liang. The consistent sustains from all of them is the assurance that my work can be done smoothly. I would like to express my gratitude to my friends, Xiangdong Li, Siyu Deng, Dakuan Zhang, Yanwei He, Hao Tian, Zhenjun Cui, Erfu Liu, Ben Niu. I have been encouraged, sustained, and inspired by all of them. Lanlan Zhong, who has been with me for most of the time in my doctoral career, encouraged, supported, and tolerated me and made me be a better person. Good luck to her without me in the future. I would like to express my deepest gratitude to my family: my father, my mother, my sister, and many other my relatives. Thanks for their generous and endless love to me. I want to acknowledge the National Science Foundation for its support for my Ph.D. research.

ABSTRACT OF THE DISSERTATION

A Novel Surface Plasmon Polaritons (SPPs) Induced Near-Field Raman Spectroscopy Imaging Technique Performed by Ultra-Sharp Tip Silver Nanowires (AgNWs)

by

Xuezhi Ma

Doctor of Philosophy, Graduate Program in Electrical Engineering
University of California, Riverside, September 2019
Dr. Ming Liu, Chairperson

With the rapid development of nano-science and nano-technology, Tip-Enhanced Raman Spectroscopy (TERS) becomes one of the most important and highest performances demanded characterization techniques among many optical microscopes. TERS combines both the Raman spectroscopy, which provide atoms vibration modes of materials and the scanning probe microscopes (SPMs), which can revile the topography of materials surface with nano- or sub-nano-spatial resolution. Although the large success has been achieved by TERS since it was proposed in 1985 and was first demonstrated in 2000, traditional TERS configurations, the directly-excited ones, are suffering from the large background signal leading to degradation of the spatial resolution and arising high chance of sample damaging by the large uncoupled far-field laser energy flux. Separating the incident laser exciting point and the Raman signal scattering point, i.e. the Remote-excited TERS (RE-TERS) configuration, seems to be a reasonable way to tackle the problem. Focused ion

beam (FIB) milling has been used to etch the pre-designed nano-grating on the sidewall of a tapered metal (gold) probe, the so-called adiabatic nanofocusing TERS probe, have been demonstrated the 0.1% to 9% coupling efficiency and TERS mapping images with sub-10 nanometers spatial resolution. However, the time-consuming, complicated fabrication process, high-cost and low reproducibility of the probes restricted their applications. Thanks for the high reproducibility and high yield chemical synthesized AgNWs have the crystallized smooth surface and ultra-sharp tip, leading to the superb plasmon performance and the abilities for nanofocusing compressed SPPs mode for an extremely confined nano-light source. To test the AgNW based SPMs performant, an ultra-sharp tip AgNWs based high spatial resolution (HR) and high aspect ratio (HAR) AFM has been achieved. Furthermore, the AgNW-AgNC bundle has been demonstrated high coupling efficiency (4%). Combing with the AgNW-AFM, high spatial resolution and high TERS contrast (largely suppressed background signal) RE-TERS has been achieved. As a benchmark, single-walled carbon nanotube (SWCNT) with ~1nm diameter served as a test sample and its D-, G- and 2D- peaks mapping image has been achieved with 9.7nm spatial resolution.

Besides the near-field TERS imaging, the vapor-assisted clean-stamp transfer method has been developed for TERS sample preparation. Using this method, we prepared graphene-based transistors with low charge-neutral concentration (3×10^{10} cm^{-2}) and high carrier mobility (up to 48 820 cm^2 V^{-1} s^{-1} at room temperature with SiO_2 supported, which is keeping the world record) and heterostructure optoelectronics with high operation speed.

Contents

List of figures

Chapter 1 AgNWs based Scanning Probe Microscopy (SPM) and Tip-Enhanced Raman Spectroscopy (TERS)

1.1 Introduction

With the rapid development of the nano-science and nano-technology, Tip-Enhanced Raman Spectroscopy (TERS) becomes one of the most important and highest performances demanded characterization techniques among many optical microscopes. Raman spectroscopy, named after the Indian physicist C.V. Raman, can provide the information of materials vibration modes, and serve as the "fingerprint" to identify the molecules[1-5]. Driven by the "scaling down" of the nano-science, like a single molecule, single-walled carbon nanotube, and many other novel nano-materials, Raman spectrum with nanometer scale, or even angstrom scale spatial resolution is demanded[6]. However, due to the loss of the high-K (large angle momentum) information during the far-field laser incident and the Raman scattering signal acquirement processes, two points closer than around half of incident wavelength cannot be distinguished, which is known as the Abbe's law, demonstrated by the German physicist Ernst Abbe in 1873[7]. In 1985, J. Wessel proposed a technique, Tip-Enhanced Raman spectroscopy (TERS)[8], using a gap mode between metal sharp tip and sample to achieve an large enhanced (up to 10^8) and ultra- confined (down to angstrom scale) electromagnetic field 15 years later, R. Zenobi group, S. Kawata group, and M. S. Anderson demonstrated the technique, separately.[9-11] By combining with the scanning probe microscopes (SPMs), such as atomic force microscopy (AFM), shear-force microscopy (SFM) and scanning tunneling microscopy (STM), linear polarized laser is sent into the gap between metal tip of SPMs probes and samples , and electromagnetic field

would be largely enhanced and confined at the gap, leading to strong scattered Raman signal. One can scan over each pixel while the Raman spectrum can be obtained at every point, which means in each pixel it contained full Raman spectrum information at the exact point on the sample. It enables constructing Raman information mapping image for the sample at a relatively large area (dimension of several hundred nanometers to several micrometers).The constructed image includes Raman peak intensity, Raman peak position and even the difference between two peaks, which is important to analysis TMDs samples (for example, the difference between E^1_{2g} and A_{1g} peaks indicate the number of layers and intrinsic strain of MoS_2 flakes). There are two configurations, aperture probe TERS[12, 13], and apertureless probe TERS, also known as scattering TERS[14, 15]. The most typical design for the former configuration is attaching a metal film coated tapered optical fiber with several tens nanometers aperture tip on a tuning fork and sending laser into the fiber to generate a subwavelength scale nano-light at the apex of the fiber[12]. Enhanced by the gap mode between metal tip and substrate, the inside large electrical field would excite the Raman signal of a local area of the sample. The smaller aperture would result in higher spatial resolution. However, low transmission of light restricts the performance of the aperture TERS probe, especially when the aperture diameter is shrinking below 50nm, the transmission coefficient would be as low as 10^{-4} and result in weak Raman signal and high thermal noise. To tackle this problem, the other configuration, the apertureless probe TERS, has been demonstrated. A sharp metal tip was used to serve as an SPM probe to get the gap mode, a linear polarized laser beam was tightly focused at the gap and was largely enhanced, leading to strong near-field Raman signal[14, 16, 17]. Rely no aperture to deliver the laser, sub-

10nm diameter sharp tip could be utilized, and high spatial resolution could be achieved. Despite of its appealing advantage and many cases of success, low signal to noise ratio is becoming the biggest restriction with the apertureless probe TERS. Only little partial of the incident laser can be coupled into the gap and contribute the TERS signal, even though those coupled power would be enhanced over 10^2 to 10^6 fold, the rest laser illumine around the tip generating large background signal with dimension of several hundred nanometers, which would degrade the spatial resolution and signal to noise ratio and arise the chance damaging the sample by large background laser. Recently, in a new configuration reported, a remote plasmon antenna was used to convert the incident laser into surface plasmon polaritons (SPPs) and re-exited it at the apex of sharp tip, the so-called remote excited TERS (RE-TERS). At the design of the prototype, the plasmon antenna was a pre-designed grating that is fabricated on the probe sidewall and several micrometers far away from the probe apex. 0.1% to 9% coupling efficiency of the antenna has been reported depending on different designs[18-22]. The excited SPPs propagate towards the sharp tip probe apex along with the tapered and metal coated probe and become compressed by the conical geometries, as known the adiabatic nanofocusing process. Both high spatial resolution and high signal to noise ratio can be achieved spontaneously because of the unique design: the sharp tip and the separation of the incident region and exciting region. Although, the grating-assisted RE-TERS has been demonstrated with great success, complicated fabrication process, time-consuming and low reproducibility of scanning probes limited its application. A cheap, time-saving, easy fabrication and high reproducibility TERS probe fabrication technique is demanded.

In general, TERS probes are prepared via vacuum deposition of a thin layer of metal, such as gold, silver or aluminum, on tapered optical fiber or AFM cantilever. The choice of the metal depends on the requirement of the plasmon resonance wavelength. Comparing the gold have strong enhancement for longer wavelength (red or longer spectral region) and the aluminum for UV and deep UV region, the silver shows good performance in the blue and green spectral region, which is more favorable for TERS experiments. On the other hand, the probes with deposited metal suffer from both low reproducibility[5] and short-lifetime[23], especially for the ultra-sharp tip with exposing the high laser power. Chemical synthesized crystalline silver nanowires (AgNWs) have high crystallinity, low defect level and automatically flat surfaces that result in the outstanding mechanical, electrical and optical properties. AgNWs attached on AFM cantilevers, STM tungsten probes, tapered optical fiber have been proved with good performance for high-aspect-ratio and high-resolution AFM (HAR-HR AFM), STM, AFM or STM based TERS imaging and RE-TERS.

In the chapter, we will review the probe fabrication, AgNWs based SPMs, probe apex influence the enhancement factor and TERS contrast, the remote-excited TERS (RE-TERS) and the state-of-the-art technique of AgNW based TERS in the chapter 1.2. In the chapter 1.3, some applications will be introduced including one and two dimensional materials.

1.2 Concepts of the AgNWs based TERS

1.2.1 AgNW TERS probe fabrication

In this section, we will review some methods for AgNW TERS probe fabrication. Comparing with some conventional TERS probe preparation method, like coating thin metal on a tapered tip or etch metal tip into the tapped profile, AgNWs have crystalized smooth surface, the subwavelength apex of tip, high electrical conductivity and good mechanical performance, which make AgNWs a good candidate to serve as SPM-TERS probes tip. To date, AFM cantilever, sharp tip tungsten STM probe, and gold coated tapered optical fiber, have been combined with AgNWs to perform TERS experiments taking advantage of both ready designs for SPM feedback with commercial probes and the promising performance of AgNWs as probe tip.

In order to fabricate a TERS probe with good performance, two key aspects should be taken into consideration are attachment of AgNW to SPM probes and the apex of the AgNW tip. The attachment includes the method of putting an AgNW on an SPM probe, the adhesion between AgNW and the sidewall of the SPM probe, the protruding length of the AgNW beyond the SPM probe which are all crucial in probe fabrication. Besides fabrication, the apex of the AgNW tip would influence the spatial resolution of both of the SPM and TERS imaging, the electromagnetic field enhancement factor of the probe and the reproducibility of the probe.

The first AgNW SPM-TERS probe was made by using an alternating current electrophoresis (AC-DEP) method by Z. Shen group in 2009[24]. A schematic shown in

Figure 1, a copper ring served as the ethanol drop holder and one of the electrode while a tapered sharp tip tungsten tip acted as another electrode, 1 MHz and 10V AC voltage were applied and the current in the loop of W tip-AgNWs solution-copper ring would drive AgNWs to place with lower electrical potential, i.e. apex of W tip or copper ring. They found the best condition for attaching one AgNWs on W tip was solution concentration of ~1e9 NWs per liter and ~1s reaction time, leading to more than 50% success rate. It worth to note that this AC-DEP method can be applied for many other metal tips or metal coated tips with the conductivity beings the only requirement.

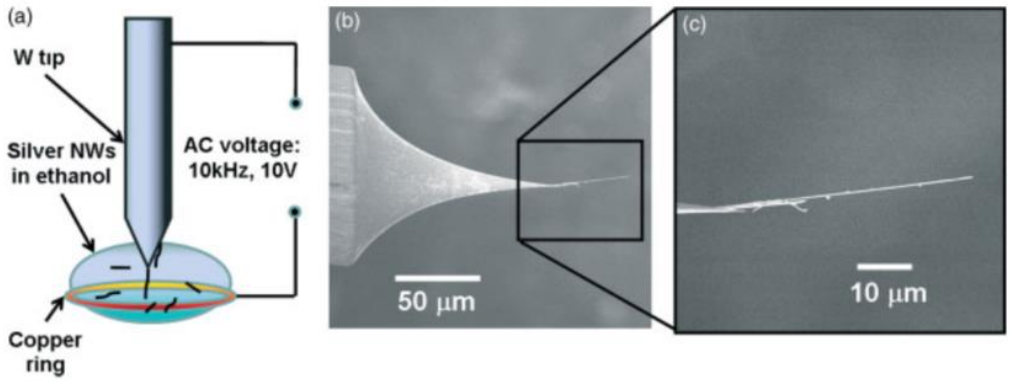

Figure 1.1 Fabrication process of the AC-DEP **a,** Schematic illustration of the AC-DEP set SEM images of W tip with attached AgNW. **c,** Zoomed-in SEM image with more information.

The AC-DEP method was welled applied in the last decade. Based on the same concept H. Uji-i group published many works [25-27]with altered conditions, e.g., different AC voltage and frequency, different materials of the ring electrode or different AgNW solution concentration. It worth noting that one of their studies[27], it was demonstrated that semiconductor AFM cantilevers also could serve as the electrode (higher voltage, 2-12V,

required), which broke the restriction of the metal or metal-coated tip proposed in Z. Shen's work[24].

Besides the AC-DEP method, H. Uji-i group reported another method for the AgNW attachment[28], taking advantage of the capillary force of instant glue drop to pick and fix a AgNW on a W tip. Super glue (Loctite SUPER GULE-3) which reacts with water when it is polymerized, was applied on the tip of an etched sharp tip tungsten probe and using a 3-D manipulator to control the tip to pick up AgNW spin-coated on a hydrophobized glass cover slide. The capillary force provided by the super glue would help to pick the target AgNW up, and as a result, the AgNW can be fixed by the super glue on the W tip. With the help of optical microscope, specific AgNW can be picked up and placed on SPM probes with controlled protruding length. **Figure 2** shows the procedure and results of this method.

As an alternative, J. Michler group proposed another method to attach the AgNW on AFM cantilever in 2011[29], the combined with an SEM-nano-manipulation attachment procedure. It was inspired by the work of attaching single-walled carbon nanotube (SWCNT) on AFM cantilever tip for high spatial resolution scanning probe microscopy (SPM) that was accomplished by H. Dai in R. Smalley group in 1996[30]. Two x,y,z-piezo stages (one was MM2A-EM, Kleindiek Nanotechnik and the other one was combination of P-620.2VL for x,y-directions and P-620.ZVL for z-direction movement) was used to control free-standing AgNWs mesh held by a razor blade and the AFM cantilever, both of two piezo stages have 50μm range and sub-nanometer resolution. The compact design of operation setup was put into SEM chamber, therefore, under the observation by SEM, the AFM cantilever can be

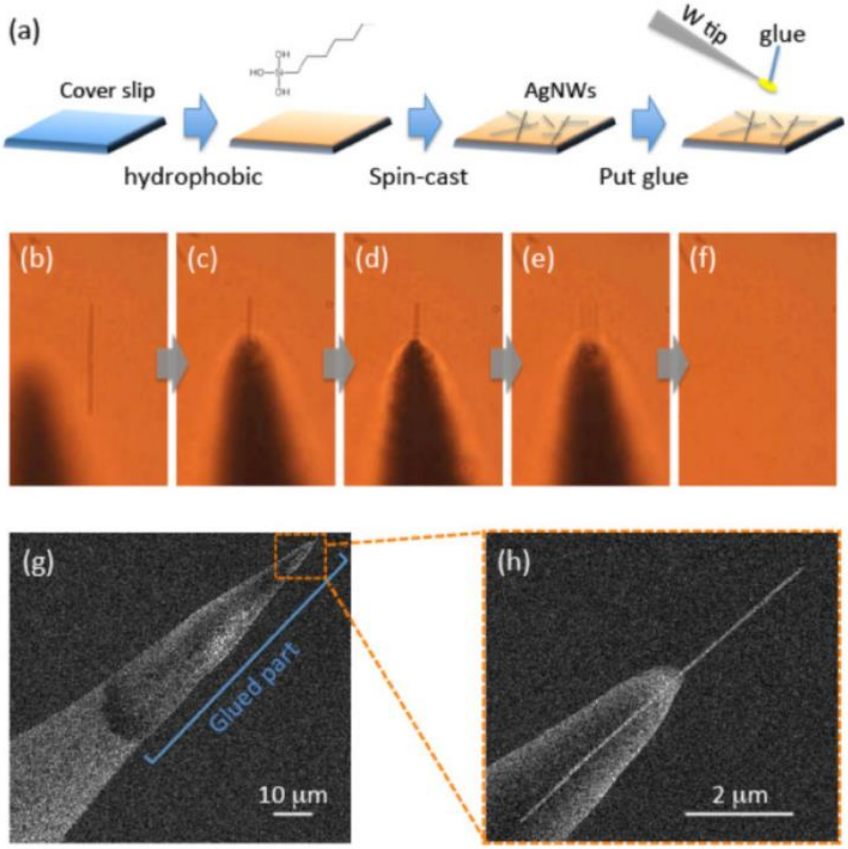

Figure 1.2 Glue-assited fabrication process **a,** Schematic of the process for attaching AgNW on Tungsten tip. **b-f,** proof of the optical microscopy image of the attachment process. **g, h,** the SEM image of tungsten probe before and after attached the AgNW.

roughly aligned with a target AgNW, coarsely operated by a robot arm. With the help of two sub-nanometer resolution 3-D piezo stages, the apex of the AFM cantilever can be aligned at the top of a selected free-standing AgNWs, followed by pushing and gluing by focused electron beam induced deposition of an amorphous, carbonaceous blob. The procedure and results are shown in **Figure 3**. The focused ion beam (FIB, Lyra Tescan) has been used for modifying the apex and the protruding length of the attached AgNW. High-resolution and high-end performance SPM and TERS require apex with a small

radius for spatial accuracy and large enhancement factor, which will be discussed in the later part of this section.

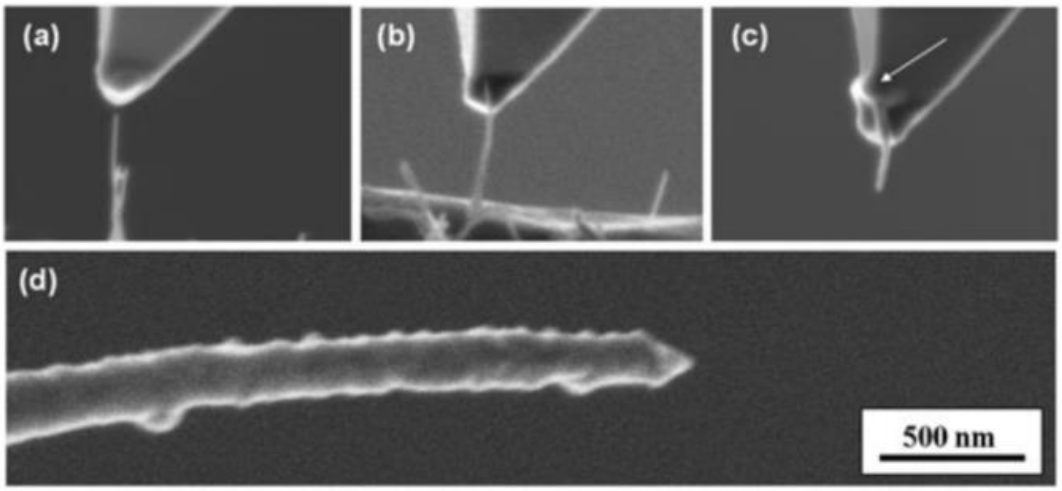

Figure 1.3 Direct attach fabrication method **a, b** and **c,** the process of the attachment (approach, welding and retraction, respectively) **d,** the high-resolution image of the tip end.

SnO_2 nanowire has been attached on the side of tapered optical fiber using a 3-D micromanipulator under the optical microscopy, and a single-cell endoscopy has been demonstrated by R. Yan from P. Yang group in 2012[31]. **Figure 4 a-c** shows the process of this method. Inspired by this work, high accuracy 3-D micromanipulator has been used to pick up a AgNW from PDMS substrate and put on one side of AFM cantilever, followed by applying instant glue (Epoxy) to enhance the adhesive force between AgNW and the sidewall of the AFM cantilever. Conducted under optical microscopy with 50x, 0.7 NA objective lens, one can choose a AgNW from thousands of candidates on the PDMS substrate, and the protruding length can be adjusted before glued as well. This work has been finished in M. Liu group in 2016[21, 32], and **Figure 4 d** show the ability for controlling

of AgNW beyond the AFM cantilever tip protruding length. Another work using the same method to apply AgNW to tungsten probe for AgNW STM-TERS has been reported in 2019[33].

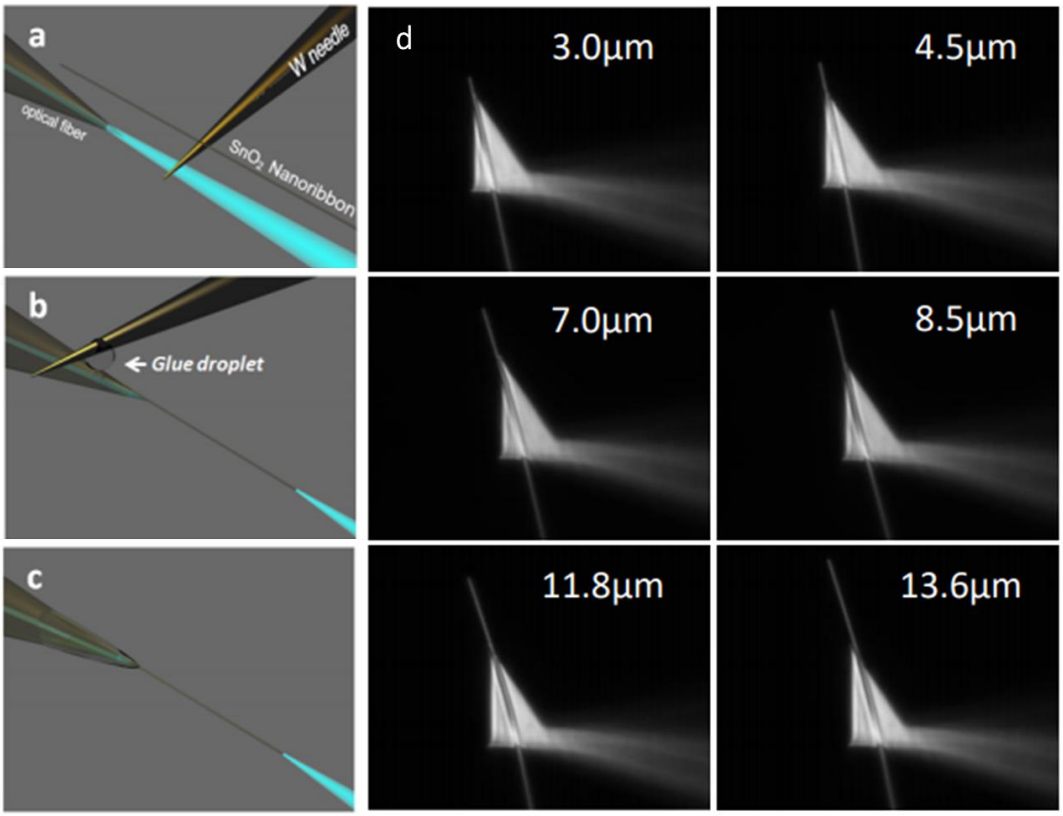

Figure 1.4 Micromanipulator method **a, b** and **c,** the process of the attachment and applying glue process. **d,** the proof of the ability for controlling of the AgNW protruding length.

1.2.2 The tip-substrate distance control: Scanning probe microscopy (SPM)

The key for both Surface-Enhanced Raman (SER) and Tip-Enhanced Raman (TER) is generating a gap mode to enhance the electromagnetic field of both incident light and scattered Raman signal. The quality of the gap influences the performance of TER,

including enhancement factor (EF) and spatial resolution. The enhancement factor can be express by the definition equation:

$$\mathrm{EF}=\frac{I_{near\ field}}{I_{far\ field}}=\frac{I_{tip-in}-I_{tip-out}}{I_{tip-out}}=\frac{I_{tip-in}}{I_{tip-out}}-1 \qquad \textbf{eq. 1.1}$$

where the I_{tip-in} is the Raman signal intensity when the TERS probe is brought in contact with the substrate, and as parallel, the $I_{tip-out}$ is the Raman signal intensity when the TERS probe is retracted at the same position. Subtracting Raman signal intensity of tip-out from that of tip-in is intended to get the pure near-field Raman signal enhanced by the gap mode. The EF becomes a criterion to determine the quality of a TERS probe; the larger EF brings the higher sensitivity of the probe. Scanning probe microscopes (SPMs), e.g. atomic force microscopy (AFM) and scanning tunneling microscopy (STM), are well used to generate and maintain the small gap between the apex of probe and metal substrate. In this section, we will review AgNWs based SPM and their performances.

1.2.2.1 AgNWs based AFM

Attaching single-walled carbon nanotubes on conventional AFM cantilever has been demonstrated by H. Dai et al. in 1996[30]. However, the complicated fabrication method restricted the application for CNTs-AFM, although it has experienced several revolutions. Direct manipulation of CNTs with observation with SEM, chemical vapor deposition growth on the tip of the cantilever and picking up a CNT or a CNT bundle by scanning an AFM cantilever over a SiO_2 substrate with grown CNTs have been used for CNTs-AFM probe fabrication. Despite their low reproducibility, high-cost and time-consuming, the

spatial resolution of a CNTs-AFM probe is limited by CNT diameter. Small diameter CNT, e.g. low chiral index single-walled CNT, can provide good spatial resolution, down to several nano-meter. The protruding length of the CNT beyond the cantilever apex should be small due to its low stiffness to avoid lateral force breaking the AFM feedback while small protruding length of the CNT-AFM probe sacrificed another advantage, the high-aspect-ratio (HAR) AFM imaging, i.e. deep-trench sample topography imaging. In parallel with CNTs, silver nanowires with a high aspect ratio (larger than 100:1) can be mounted on AFM cantilever for HAR AFM image, and protruding length can be larger than 5μm due to its large stiffness (160GPa of Young's modulus). Moreover, Liu group has demonstrated the ultra-sharp tip AgNWs leading to high spatial resolution AFM imaging as well. Individual nanowires are readily distinguishable under optical microscopes can be handled by a micro-manipulator, enabling low-cost, fast, high-reproducibility fabrication protocols.

M. Liu group and Dr. H. Uji-i group have demonstrated the high-aspect-ratio and high resolution (HAR-HR) AgNW attached AFM in 2016 and 2018, respectively[27, 32]. Different methods for probe fabrication (direct manipulate and the AC-DEP) lead to similar results; deep trench sample has been used to benchmark the HAR performance and several nanometers spatial resolution has been achieved. The comparison between scanning over the same deep trench with AgNW-AFM probe (**Figure 5 a** and **d**) and conventional AFM cantilever (**Figure 5 b** and **e**) provide solid evidence to demonstrate the HAR performance of AgNW-AFM. Thanks to the ultra-sharp tip AgNW, a 6nm spatial resolution has been achieved in the single-walled CNTs scanning (**Figure 5 f** and **h**, the red cross line). Also,

after 15 times dual scanning, the performance of this ultra-sharp AgNW-AFM probe shows no obvious decay, proving the high wear resistance of the probe.

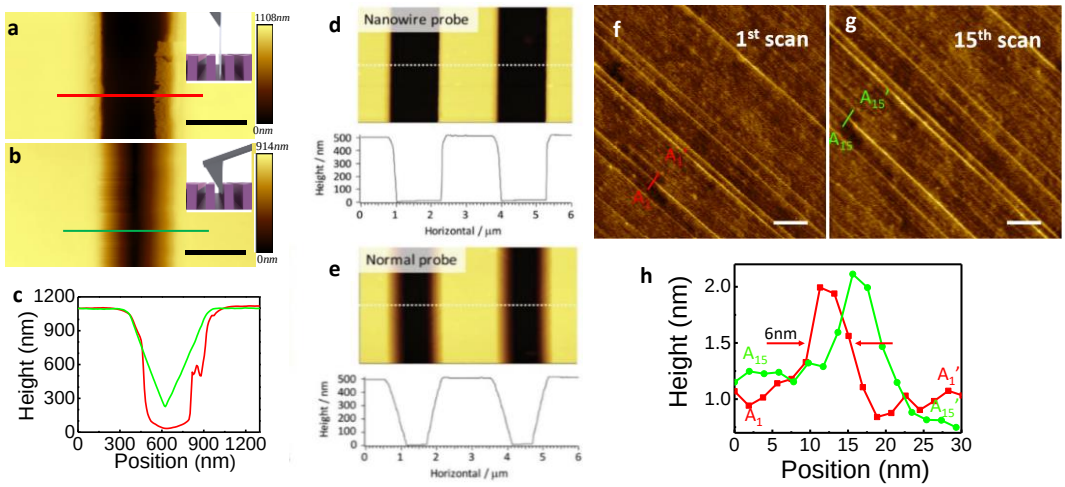

Figure 1.5 High-Aspect-Ratio (HAR) benchmark for the AgNW-AFM probe using a deep trench sample. **f-h,** High-Resolution (HR) and wear resistance benchmark for the AgNW-AFM probe using a single-walled CNTs sample.

1.2.2.2 AgNWs based STM

Scanning Tunneling Microscopy (STM) can provide Angstrom scale spatial resolution and has been well applied in the field of nano-science since its first demonstration in 1981[34]. There are several key aspects to achieve Angstrom resolution, including low thermal vibration of the probe apex, low conductive resistance for the current loop, and small radius of the probe tip. Polyol-synthesized AgNWs have high crystallinity, low defects, and native atomically flat surfaces and makes the AgNW attached STM probe a good candidate for STM imaging. Polyvinylpyrrolidone (PVP) molecules play a critical role during the AgNWs synthesis process and can be formed a several nanometers layer wrapped on both of the sidewall and tip of the AgNWs. The PVP layer not only largely increase the

resistance between AgNW and tungsten or Pt-Ir probes (conventional STM probe), but also generate a big barrier at the apex of AgNW to hinder the tunneling current.

The first issue, thermal vibration of the probe apex, reduces the STM spatial resolution directly that large vibration cannot provide an accurate spatial resolution which smaller than the vibration amplitude. Thermal equipartition theorem has been used to calculate the thermal fluctuation of the AgNW tip apex in M. Liu group recent work[33]. The equipartition theorem gives $\frac{1}{2}\mathrm{k}_B T = \frac{1}{2} K \left\langle x^2 \right\rangle$, where k_B is the Boltzmann constant, T is the absolute temperature, and K is the spring constant of protrude AgNW and is given by $K = \frac{3EI}{L^3}$, E is Young's modulus of AgNW (~90GPa[35]), I is the area moment of inertia for a cylindrical nanowire and L is the protruding length of the AgNW. The thermally induced root-mean-square oscillation of the AgNW tip can be derived as:

$$\left\langle r.m.s._{thermal} \right\rangle_{25°C} = 5.6\times10^{-3} \frac{L^{3/2}}{\mathrm{d}^2} \mathrm{A} \qquad \textbf{eq. 1.2}$$

this equation works at a temperature of $25°C$ and both the L (protruding length of the attached AgNW), and the d (diameter of the AgNW) are in the unit of μm. According to this equation, the sub-angstrom resolution requires the L to be shorter than 3.7μm for a 200nm diameter AgNW and 1.5μm for a 100nm diameter AgNW. The fabrication method of using micromanipulator for directly attachment and adjustment would be the best way to reduce the protruding length during the fabrication process for a low thermal vibration AgNW-STM probe.

The PVP layer over AgNWs surface created during the synthesis process, restricts the STM performance as well. The purification process is introduced by M. Liu group work, in which they applied ethanol wash and centrifugation to reduce the thickness of the attached PVP layer and then $NaBH_4$ treatment to remove residual PVP until the PVP shell cannot hinder the current that through both the junction between commercial STM probe and AgNW sidewalls as well as AgNW apex and substrate. It worth to note that AgNWs in solution (ethanol) would be very easy to get oxidized due to the oxygen that dissolved in the solution. N_2 bubble process is introduced to purge the dissolved oxygen and protect AgNWs from oxidation. **Figure 6 a** and **b** shows the TEM image of the PVP shell that wrapped around the AgNW and the reduced thickness of the PVP shell after purification. **Figure 6 e** shows the comparison of STM imaging for an as-deposited gold surface between after washed six times with ethanol and $NaBH_4$ cleaning, which provides direct evidence that the STM performance degraded by the PVP shell. **Figure 6 f** is the tunneling current variation as a function of the probe forwards to the substrate distance of AgNW with and without PVP probe and commercial Pt/Ir probe. The AgNW without PVP covered shows as good performance as the commercial Pt/Ir probe while the performance comparison between with and without PVP provide solid evidence of the negative influence of the PVP shell.

The multichannel effect, aroused by multiple points at the apex inducing tunneling current through the apex of an STM probe to the substrate, leads to blurred STM imaging or ghost image. To avoid the multichannel effect that reduces the performance of an STM, the apex

of STM probe fabricated needs to be sharp and smooth. DC or AC voltage assisted electrochemical etching method is well used for commercial STM Pt/Ir or tungsten sharp tip probe fabrication[36]. However, the low reproducibility, time-consuming and complicated process restricts the application for a high-quality STM imaging. Mechanical sharpen using two pliers to fabricate the sharp tip of the Pt/Ir probe is also introduced for STM probe fabrication, but the apex quality is hard to control and avoiding the multichannel effect is the big challenge[37].

The ultra-sharp tip AgNWs, introduced by M. Liu group and mentioned before can help to solve the problem. Ultra-sharp AgNW STM probe shows a good performance in both STM and STM-TERS imaging with several nanometers diameter apex and smooth profile of the tip. **Figure 6 g** and **h** show the comparison of the STM imaging for ultra-smooth gold substrate supported single-walled carbon nanotubes (SWCNTs) between regular tip AgNW and ultra-sharp tip AgNW based STM probes, and **Figure 6 c** and **d** show the corresponding AgNW SEM image, respectively. Detailed information is extracted by the ultra-sharp tip AgNW based STM probe, several nanometers lateral resolution and angstrom level horizontal resolution have been achieved. The STM-TERS has been demonstrated, and the benchmark will be reviewed in the next section.

Similar design and result were reported by H. Uji-I group in 2014[25]. They used the AC-DEP method to attach an AgNW on commercial tungsten STM probe and got angstrom spatial resolution STM imaging.

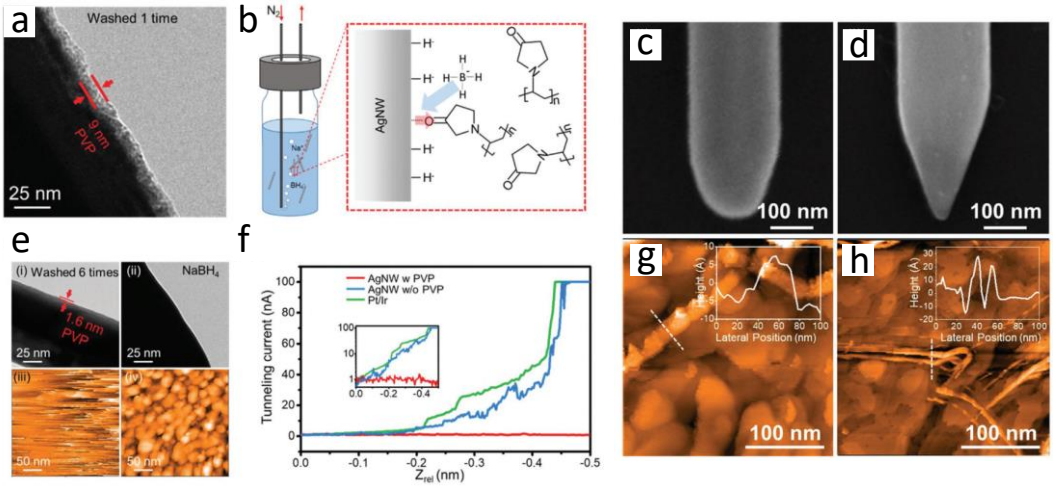

Figure 1.6 Ultra-sharp tip AgNW based STM imaging **a** and **b,** the TEM image of the PVP shell that wrapped around the AgNW and the reduced thickness of the PVP shell after purification. **c and d,** the SEM image of the round shape and ultra-sharp tip AgNW. **e,** the comparison of STM imaging for an as-deposited gold surface between after washed six times with ethanol and $NaBH_4$ cleaning. **f**, the tunneling current variation as a function of the probe forwards to the substrate distance of AgNW with and without PVP probe and commercial Pt/Ir probe. **g** and **h**, the comparison of the STM imaging for ultra-smooth gold substrate supported single-walled carbon nanotubes (SWCNTs) between regular tip AgNW and ultra-sharp tip AgNW based STM probes.

1.2.3 TERS tip radius and TERS enhancement factor

The enhancement factor (EF), which mentioned before, is one of the most important parameter to determine the quality of a TERS setup. Largely enhanced by the metal tip, the near-field Raman signal should be stronger than the far-field background signal and stand out to achieve sub-wavelength resolution. Excited by the apex of TERS probe, the tightly focused incident laser beam would be convert into confined near-field surface plasmon and generate nano-scale near-field enhanced Raman signal. However, the radius of the probe apexes are always sub-wavelength, especially several nanometers for finer near-field distribution and hence only a small portion of incident light could be influenced by the small tip and be convert into near-field. The rest far-field energy would generate large

background Raman signal with low resolution that governed by Abbe's law, leading to smeared Raman mapping image. Therefore, the coupling efficient (η) defined here, the coupled into near-field energy over incident energy, can help us to revise the enhancement factor (EF). The EF, we made the definition before is:

$$\mathrm{EF}=\frac{I_{near\ field}}{I_{far\ field}}=\frac{I_{tip-in}-I_{tip-out}}{I_{tip-out}}=\frac{I_{tip-in}}{I_{tip-out}}-1 \qquad \textbf{eq.1.1}$$

Apparently, this equation underestimated the EF due to the assumption of all of the incident energy would be enhanced by TERS tip. Thus, the revised EF should be:

$$\mathrm{EF}_{revised}=\frac{I_{near\ field}}{I_{Coupled\ far\ field}}=\frac{I_{near\ field}}{I_{far\ field}\eta}=\frac{I_{tip-in}-I_{tip-out}}{I_{tip-out}}\frac{1}{\eta} \qquad \textbf{eq.1.3}$$

Furthermore, the coupling efficiency can be simplified as

$$\eta=\frac{A_{TERS}}{A_{background}} \qquad \textbf{eq.1.4}$$

where $A_{background}$ is the area of the excitation, the laser spot, and A_{TERS} is the effective area of the TERS enhancement region. Small diameter apex TERS probes are always chosen for better spatial resolution of both TERS imaging and SPM imaging, leading to smaller A_{TERS} and smaller η as a result. On the other hand, the sharper TERS tip would generate much higher enhancement factor due to higher electrons density accumulated at the smaller diameter apex and induce larger enhanced electromagnetic field. As a result, multiplying EF_{tip} (eq.2) by η (eq.3) can get totally TERS probe enhancement factor which is EF

(**eq.1.3**), and we can define it as the TERS contrast, C_{TERS}, which is the key parameter to determine the quality of a probe. We have

$$C_{TERS} = \frac{I_{TERS} - I_{background}}{I_{background}} = \frac{I_{tip-in}}{I_{tip-out}} - 1 \qquad \textbf{eq.1.5}$$

$$C_{TERS} = EF_{revised} \cdot \eta \qquad \textbf{eq.1.6}$$

In order to obtain large TERS contrast, one can increase $EF_{revised}$ and η through engineering TERS probe apex structure or smart design. In this section, we will review some examples of the AgNWs based TERS attempting to achieve high TERS contrast and high resolution.

Most of the AgNWs can be etched in the solution and remain a round shape of random profiles of apex. Many works of AgNW based TERS, either STM based or AFM based, have been attempted and lead to around several fold to tens of TERS contrast (C_{TERS})[24, 25].

The natural crystalized apex of a AgNW, the pentagonal pyramid profile, have sharp tip (several nanometer diameter of apex) and allowed high density electrons accumulate at the sharp apex to generate large electromagnetic filed, especially a gap mode with metal substrate is established. Around 500 of TERS contrast has been reported by H. Uji-i group in 2018, compared with conventional TERS used an etched gold tip that 50 of TERS contrast was achieved[27].

Tip structure engineering enables the enlarged coupling efficiency (η). A silver globule that produced by a so-called joule-heating serves as the TERS probe apex was reported by

Dr. H. Uji-i group in 2018. They used a sharp tungsten tip with applied 1-2v voltage, that was controlled by a 3D manipulator, to touch the protrude AgNW of a prepared AgNW-tungsten STM-TERS probe that connected ground. Current loop could be set-up and large joule heat would be generated at the touching point, due to the poor electrical connection at the point and the large resistance as the result. The AgNW heated by the joule heat and would be melt, and a silver globule would be formed by the continuous heat and the capillary force of itself after around 5 mins (**Figure 7 a-d**, the fabrication process and results). Compared with the no-cut AgNW-STM TERS probe, the silver globule apex enlarged the coupling efficiency (η) by increase effective area of TERS enhancement region (A_{TERS}) and result in twice larger TERS contrast, as shown in **Figure 7 e**.

Ultra-sharp silver nanowire has been reported by Dr. M. Liu group in 2016 mentioned preciously[32]. Even though the $EF_{revised}$ would be largely enhanced due to the sharp apex, the small A_{TERS} may leads to low coupling efficiency (η) and the TERS contrast remains uncertain and further researches need to be performed.

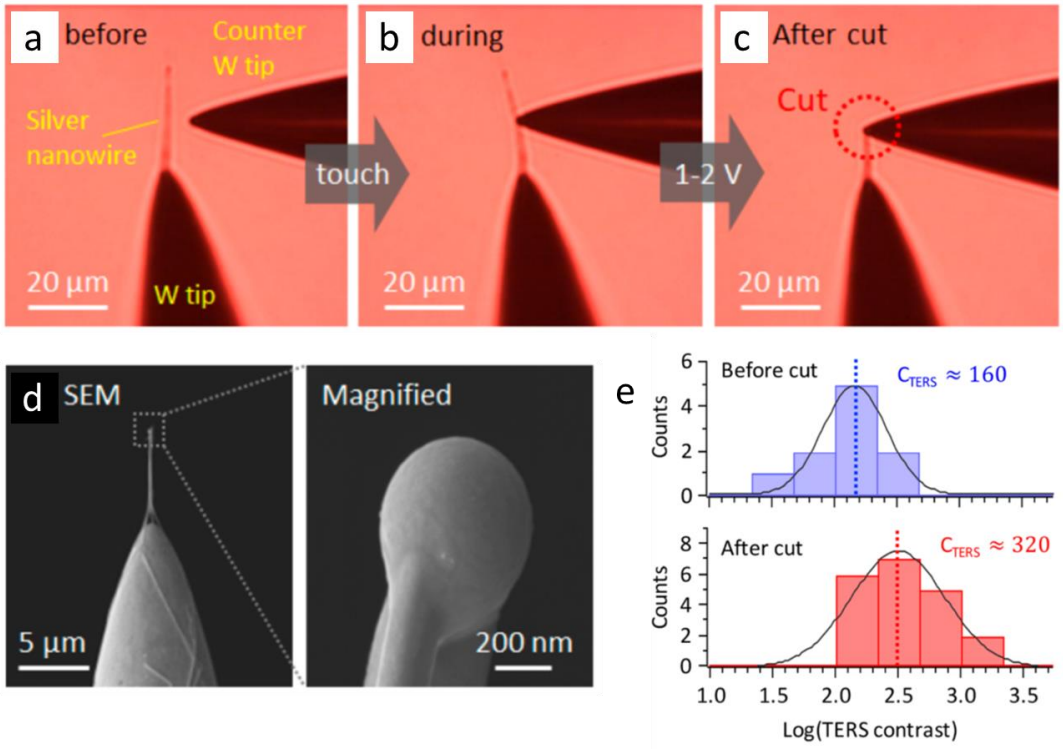

Figure 1.7 The heat induced sphere tip TERS probe **a, b** and **c,** the fabrication process of the silver globule. **d,** the SEM image of the engineered AgNW-STM TERS probe and the silver globule. **e**, TERS contrast comparison using cut tip and no-cut tip.

1.2.4 Advanced AgNWs based TERS techniques

In the last section, we discussed that the coupling efficiency (η) and tip enhancement factor ($EF_{revised}$) determined the TERS contrast (C_{TERS}) together, and higher η and higher $EF_{revised}$ would give better TERS result. The low η results from large background Raman signal, and separating incident point and scattering point to remove the influence of the large background signal sounds reasonable. Recently, grating-assisted plasmonic-nanofocusing probes have demonstrated and serve as a candidate for remote-excited TERS solution to eliminate the background signal. Designed grating milled by focused ion beam

(FIB) on sidewall of a tapered metal probe convert the incident laser into surface plasmon polaritons (SPPs) mode that propagate on the surface towards to the apex of the probe and exited nano-confined light[18]. The grating is designed for matching the incident momentum where the grating period a_0 determined by the in-plane momentum conservation condition $k_{spp} = k_{in} + nG$, k_{spp} and k_{in} are in-plane momentum of SPP mode and incident light, respectively, and n is an integer and $G = 2\pi/a_0$. Depends on the different designs, 0.1-9% coupling efficiency, the enrgy ratio between the excited light at apex and the incident light, has been reported[18-20]. However, the low reproducibility and complicate process of the grating-assisted probe fabrication restrict the application of the technique. Silver nano-cube (AgNC) and AgNW bundle has been demonstrated as a broadband spectra (visible) antenna to excite SPP mode and achieve the nano-focusing at the apex of AgNW. Thanks to the dimension controllable and large reproducibility for both AgNC and AgNW, the AgNC-AgNW remote-exited TERS probes provide another solution to eliminate the background signal for high TERS contrast (C_{TERS}).

AgNW-AgNC bundle serve as an endoscopy for a HeLa cell inside Raman information extraction has been first demonstrated by H. Uji-i group in 2014, a tens nanometers dimension AgNC attached on the side of a 50-150 nm diameter AgNW and works as a antenna to match the incident light momentum and couple them into SPP mode. Excited nanoscale light at the apex of AgNW could be enhanced by the sharp profile of the AgNW apex and generate relative large Raman signal that received by an invert microscope (TiU, Nikon) and resolved by a spectrometer (iHR 320, Horiba). It worth nothing that they used

the same objective lens to tightly focus the incident laser and receive the Raman signal, because the remote exited point and Raman scattering point are very close with each other (~2μm) and they can be covered in the field of view of the objective lens. As a follow up work, they combined the remote-excited probe (the AgNW-AgNC bundle) with a tungsten based shear-force AFM probe, which enabling the apex of probe work at the surface of metal substrate and both of the nanoscale light and scattered Raman signal can be enhanced by the gap between the probe apex and metal substrate. Comparing with the conventional direct-exited Raman, the remote-excited Raman C_{TERS} (TERS contrast) achieved roughly 3 to 4 times larger value. However, the coupling efficiency of the AgNC remote coupler is not high enough and results in low remote-excited TERS signal and TERS contrast, which result from the lake of the dimension control for both AgNWs and AgNCs, of the quantitative design for high coupling efficiency, and of sharp apex for high enhancement factor ($EF_{revised}$).

M. Liu group reported an optimized AgNW-AgNC bundle based remote-exited TERS and 3.0% coupling efficiency and exceed 100 fold of TERS contrast have been achieved[21]. Finite element analysis numerical simulations (COMSOL Multiphysics 5.1) were carried out to optimize the parameters (AgNW and AgNC dimension and polarization) for high coupling efficiency. The diameter of AgNW was 200nm and the AgNC size was swept in the range between 20 to 300nm, with step of 10nm. The wavelength incident laser ranging from 450nm to 800nm with step of 5nm. The distance between the AgNW-AgNC junction and apex of AgNW was set as 2μm. They found that the best condition is size of 185nm AgNC attached on side of 200nm diameter of AgNW under S- polarized (perpendicular to

the contact surface between the AgNW and the AgNC) 510nm wavelength laser. As the nearest wavelength conventional laser source, a 532nm wavelength green laser has been used and near 4% coupling efficiency can be achieved. Practically, under a 50x dark-field optical microscope, they used the 3D micro-manipulator to control a sharp tip tungsten probe to pick a selected AgNW-AgNC bundle that made of the mixture-incubation method and attached it on sidewall of a conventional AFM cantilever, which fabrication process has been illustrated in previous section. The so-called "mixture-incubation" method is custom friendly and have high yield, the AgNW ethanol solution (~10^8/mL, diameter of 200 ± 20nm) and AgNC ethanol solution (~10^{11}/mL, size of 180 ± 10nm) were mixed and then incubated for 2 days at room temperature. 3D micro-manipulator controlled sharp tip tungsten probe can move or remove AgNCs to adjust the bundle to preferred condition for both high coupling efficiency and efficient AFM feedback. **Figure 8 a-d** show the SEM image of this AgNW-AgNC bundle based remote-excited TERS probe and the dark-field optical microscopy image of the coupling efficiency. The AgNW-AgNC junction serve as a coupler is prefer the S-polarization incident laser and the uncoupled S-polarization incident laser illuminate at the surface of the substrate is not only out of focus, leading to low energy density to alleviate the extra damage for the sample, but also not the preferred polarization to excite background Raman signal. **Figure 8 e** and **f** are the Raman signal comparison of the remote-excited TERS and conventional direct-excited TERS for the 4-ATP self-assemble monolayer (SAM) under S- and P- polarization incident laser, respectively. The TERS contrast of RE-TERS ($C_{RE\text{-}TERS}$) can exceed ~ 100, ~47 fold better than of DE-TERS ($C_{DE\text{-}TERS}$) under the S- polarization.

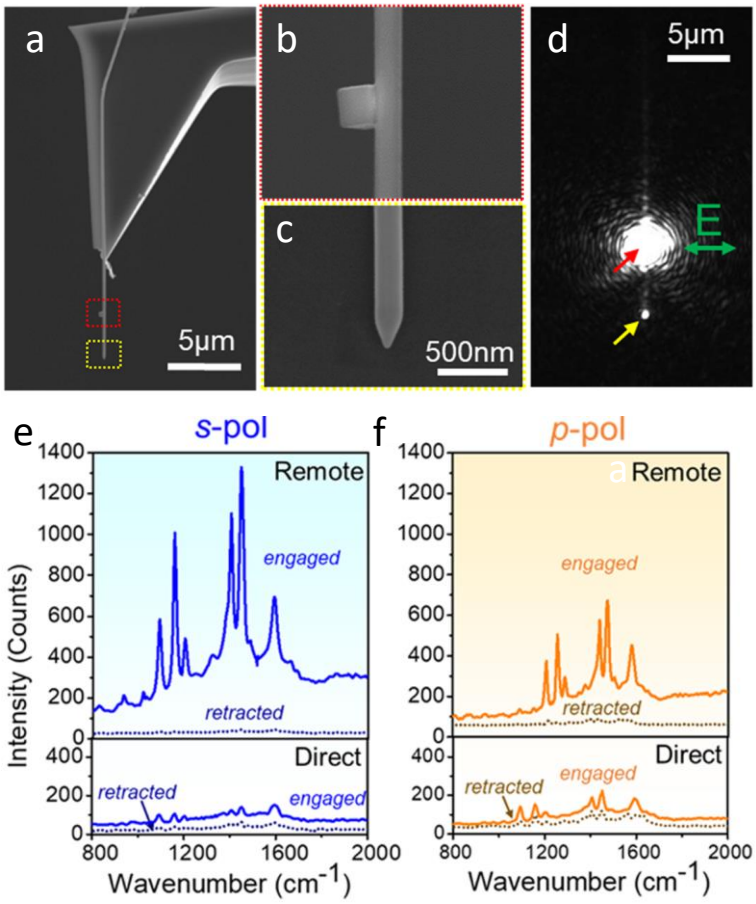

Figure 1.8 the AgNW-AgNC bundle based RE-TERS **a, b** and **c,** the SEM image of the RE-TERS probe, zoom-in SEM image of the AgNW-AgNC junction and the sharp tip apex **d,** the dark-field optical microscopy image for coupling efficiency **e** and **f**, the comparison of RE-TERS and DE-TERS Raman signal under S- and P- polarization incident laser.

Either the conventional directly exited TERS configurations or the remote excited TERS concepts are belonging to the family of apertureless NSOM. We have reviewed that the aperture NSOM restricted by itself struggling from the trade-off that either poor spatial resolution (tip radius) or low transmittance. However, the aperture NSOM hold many advantages, including the potential of lens-free (probe signal-in and signal-out) configuration, the easy-handle adjustment for laser path (especially for incident light) and

low background. Beside the blooming progress of the apertureless NSOM and hard moving of the aperture NSOM, a high-external-efficiency nanofocusing NSOM has been reported very recently. Combining aperture and apertureless NSOM advantages, this novel two-step sequential nanofocusing technique achieved high-efficiency (~50%), broadband, and probe-in and probe-out for near-field excitation and spectrum collection. Among many nanofocusing NSOM concepts, the SPP modes are coupled in and compressed into high K (momentum) modes for super spatial resolution. Many demonstrated novel NSOM concepts, such as tip-integrated bow-tie antennas or grating-assisted adiabatic probes, are designed for exciting SPP modes to smooth the large momentum mismatch between the incident far-field light ($k\sim10^5$ cm^{-1}) and the highly confined localized-surface-plasmon mode (LSP, $k>10^7$ cm^{-1}). However, the low SPPs coupling efficiency of those designs limited the application of NSOM. The prism coupling method, the Otto configuration, is the most efficient way to excite SPP modes, which using the resonant mode coupling when the phase-mating condition happened. The SPP modes propagate alone the AgNW with low energy loss smooth surface towards to the ultra-sharp tip and are compressed into high K TM_0 mode, i.e. the quasi-adiabatic nanofocusing process, with as high as 70% efficiency. Combined with a commercial STM (NatioSTM BY Nanosurf AG), the two-step nanofocusing probe can scan over a hundreds nanometers area with sub-nanometer spatial resolution. Excited Raman signal at the apex-substrate gap would be collected by the two-step nanofocusing probe and result in a high resolution probe-in and probe-out lens free TERS microscope. As a proof, single wall carbon nanotube (SWCNTs) on smooth gold surface has been characterized and 1nm spatial resolution achieved.

1.3 Applications

Unlike the confocal Raman spectrum are excited by incident laser with in-plane polarization, tip-enhanced Raman (TER) spectrum are arise from enhanced E-field that perpendicular to the sample surface in the gap, no matter what polarization of the free-space incident laser. Raman spectra revile the vibration modes of the objective sample, and some materials show strong polarization-dependent properties. The single-walled carbon nanotube, for example, the radial breathing mode (RBM) reflects carbon atoms vibration along the circumferential direction and is an indicator to determine the diameter of a CNT, the incident laser with polarization that along the tube axis direction cannot excite this mode efficiently. Another example is the G-band is arising from the stretching of the C-C bond and shows strong polarization dependent, i.e. it is easier to be excited by the polarization that along the tube axis direction. In the many SWCNTs system, the tube to tube interaction should be took into consideration and may cause symmetry breaking effect, resulting in the G-band split into six modes: two A (A_{1g}), two doubly degenerate E_1 (E_{1g}), and two doubly degenerate E_2 (E_{2g}) modes. The totally symmetric A modes can be observed by the exited laser with polarization that parallel to the tube axis direction, the E_1 modes can be observed by the cross polarized Raman spectra (parallel direction polarization in and perpendicular direction polarization detected), and the E_2 mode can only be detected by the perpendicular direction polarization laser. For those curved CNT or CNT bundle, TERS amplify the polarization that perpendicular to the sample surface, which can help studying the RBM, E_2 modes. We will review couple of applications of the AgNWs based TERS including 1D, 2D and many other materials in this section.

1.3.1 1D materials

One dimensional (1D) materials includes carbon nanotubes, nanowires, carbon nano-ribbons and many more. Among those 1D materials, their other two dimensions have limited size (several nanometers to tens nanometers) and cannot scattered Raman signal efficiently. The single walled carbon nanotubes (SWCNTs) diameter ranging from sub-nanometers to several nanometers depends on its chiral index n and m, governed by the equation: $\mathrm{d} = \frac{0.246}{\pi}\sqrt{(n^2 + nm + m^2)}$. The conventional Raman spectroscopy has been widely carried out to invest the vibration modes of the CNTs, the poor spatial resolution, however, restricts its application and cannot solve complicated cases, like the CNT bundle. The TERS provide an enhanced and confined electromagnetic field to efficiently scatter Raman signal with high spatial resolution down to sub ten nanometers. Importantly, CNTs have also become a "benchmark sample" for novel TERS tools due to it reduced dimensions in two directions and would serve as a "probe" to map the light source reversely. The quality of the light source is determined by several aspect, including the source vibration amplitude, its size and its exciting modes.

Firstly, the vibration at TERS probe apex may arouse from ambient thermal vibration or laser heat effect, limiting the TERS spatial accuracy. Commonly, the AgNWs TERS probes are fabricated by attaching a AgNW on a commercial SPM probe to get the help from the ready SPM feedback system. The protruding length of the AgNW work as a vibrating stick driven by the thermal energy. We have discussed, in the previous section, the thermal vibration and got an equation:

$$\left\langle r.m.s._{thermal} \right\rangle_{25°C} = 5.6\times10^{-3}\frac{L^{3/2}}{d^2} \qquad \textbf{eq. 1.2}$$

where L is the protruding length and the d is the diameter of the AgNW and both of their unit are μm. It shows the longer protruding length and the thinner diameter of the AgNW leads to higher amplitude of the apex vibration. However, limited by the probes fabrication methods or the special demands, like enough space placing AgNC for the RE-TERS or the long protruding length for high-aspect-ratio (HAR) AFM, the protruding length cannot keep short. Here we will highlight some works that using the SWCNTs as the benchmark subject.

Regular crystalline AgNW apex has been used to perform the directly exited TERS (DE-TERS) by H. Uji-i group in 2018. AgNW combined with AFM cantilever that controlled under both contact mode and tapping mode and achieved TERS mapping images with as high as 9.9 nm spatial resolution (**Figure 9 a-c**). Although, the apex is keep tapping during the scanning under tapping mode AFM and only little portion of time the gap mode works for large enhancement factor, enhanced Raman signal still have been achieved due to the large TERS contrast (C_{TERS}) (the 500 of C_{TERS} has been demonstrated using the contact mode). Considering the distance between apex and substrate is a sine function of time, the amplitude was 20nm and result in 14.4% of time the distance maintained within 2nm. The Raman signal would be exponentially decrease as the increasing of the apex-substrate distance, leading to acceptable TERS signal and contrast. Despite some works that record the TERS signal only when the apex-substrate distance smaller than a pre-set threshold[38, 39], there is rarely TERS mapping image achieved under tapping mode.

Remote-excited TERS (RE-TERS) was tested using the SWCNTs sample as well. In the paper of AgNW-AgNC bundle based RE-TERS that reported by Liu group, 9.7nm spatial resolution has been demonstrated (**Figure 9 d-j**). Among most of the AFM based TERS, including AgNW-TERS or other techniques, around 10nm spatial resolution seems to be a

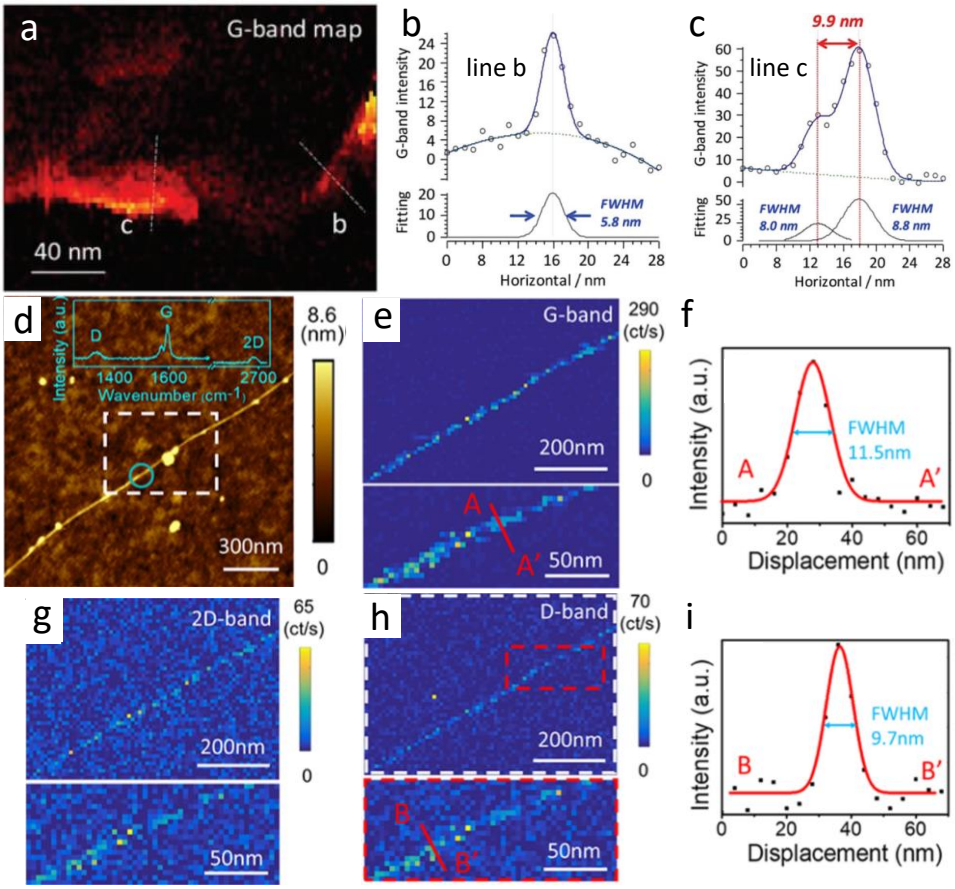

Figure 1.9 SWCNT sample benchmark using the RE-TERS probe **a,** TERS map of the G-band of a CNT on gold substrate with 2nm for one pixel. **b** and **c,** cross line labeled in **a** shows 9.9 nm spatial resolution **d,** AFM morphology imaging mapping of single-walled CNTs, sprayed on a smooth Au substrate. **e,** G-band, **g,** 2D-band, and **h,** D-band intensity images. Spatial steps are 10 nm for top images and 4 nm for the zoom-in at bottom, **f** and **i** are line cross-section of the marked regions in **e** and **h,** 9.7 nm spatial resolution is shown.

performance celling. The large vibrations, we mentioned above, that are originated from the thermal, the air floor or even the principle of the AFM—vibrating for feedback—may

limit the resolution. STM, a dynamic feedback SPM, can provide with a stable nano-light source and result in several nanometers or even sub-nanometers spatial resolution[6]. Another paper from M. Liu group reported a work that has been achieved ~1nm spatial resolution using the AgNW based nanofocusing probe STM based TERS.

1.3.2 2D materials

Graphene, transition metal dichalcogenide (TMD, such as MoS_2, WSe_2, et al.), and many more two-dimensional (2D) nano-materials (like hBN or black phosphorus) have triggered a wide range of interests due to their exciting performances and unique physical properties since Novoselov, Geim and co-workers successfully exfoliated graphene from graphite using the "Scotch tape" method in 2004. TERS and TERS mapping has been widely used to study the 2D nano-materials in the past 15 years. Gap mode plays an important role in TERS mapping to take advantage of the Purcell effect for stronger Raman signal, 2D materials, including CVD growth and exfoliated ones, have been transferred onto metal substrates to perform the TERS experiments. However, the roughness of the metal surface arise strong surface enhanced Raman (SER) and contributes large background signal that degrade the TERS contrast. Large TERS contrast technique are required as a result.

The AgNW-AgNC bundle based remoted-excited TERS, reported by M. Liu group, mapped a tensile stained transferred CVD monolayer MoS_2 flack with smooth gold supported. There are two major Raman modes of MoS_2, the E_{2g}^1 and the A_{1g}, the former one reflect the atoms in-plane vibration while the latter one shows the out-of-plane

vibration. Compared with the A_{1g} mode, the E^1_{2g} mode is influenced by the stress more and Raman peak would red-shift. The frequency differences between two peaks $\Delta\tilde{\nu}$ ($\Delta\tilde{\nu} = \tilde{\nu}_{A_{1g}} - \tilde{\nu}_{E^1_{2g}}$) of MoS_2 is the indicator to determine both the number of layer and the inside strain, which varies from 18.2 to 20.0 cm^{-1} and all of them fall within the monolayer region. **Figure 10 g** the mapping of the $\Delta\tilde{\nu}$, there is a strong spatial dependence and ~1.8 cm^{-1}

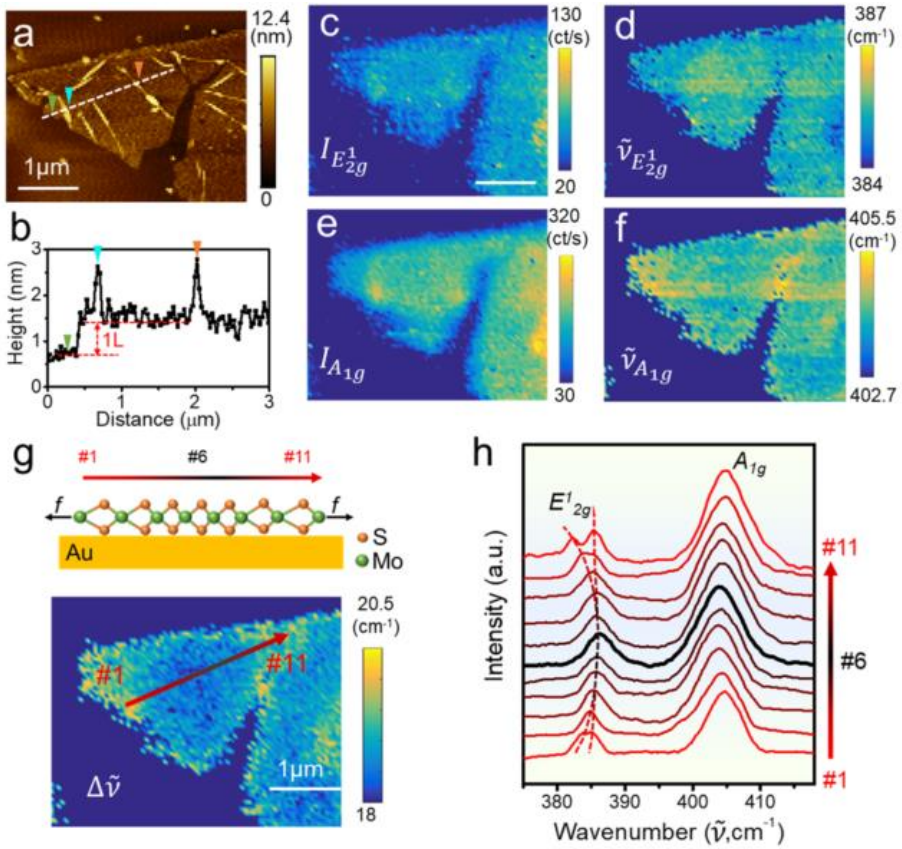

Figure 1.10 MoS_2 flack sample TERS imaging using the RE-TERS probe. **a,** AFM image of a tensile strain CVD MoS_2 flack on gold substrate. **b,** the profile of the cross line shown in **a**, **c** and **e,** intensity mapping of E^1_{2g} and A_{1g} peak. **d** and **f**, peak wavenumber mapping of E^1_{2g} and A_{1g} peak. **g,** mapping of the frequency differences between two peaks Δν̃. **h,** Raman spectrum show the peak drift that corresponding to each point labeled in **g**.

larger at the edges and near the cracks of the flack than at the center region. **Figure 10 c** and **e** shows the intensity mapping of both the A_{1g} mode and the E^1_{2g} respectively, and

there are many details, the grains and the boundary at the crack region, are distinguishable in the TERS mapping, which shows good performance of this RE-TERS.

1.4 Summary and perspective

TERS combined both the Raman spectroscopy, which provide atoms vibration modes of materials, and the scanning probe microscopies (SPMs), which have the ability to revile the topography of substrate surface with nano- of sub-nano-spatial resolution. However, both of two different TERS concepts, the aperture probe based TERS and the apertureless probe (scattering) based TERS are suffering from problems. The hard balance between shrinking diameter of probe apex and exponential decay light transmission rate as the diameter decrease for the aperture probe based TERS. The apertureless probe based TERS is limited by its low TERS contrast result from large background signal and low reproducibility of probe fabrication. Although the grating assisted adiabatic nanofocusing probe has been achieved for the remote-excited TERS to solve the problem of the large background signal, the complicated fabrication and time-consuming of this probe restrict its application. The AgNW based TERS probe make the fabrication process much easier and have been demonstrated good performance of both TERS and SPM.

In the chapter 1.2, we mentioned the some aspects that related to the AgNW based TERS technique.

1) The fabrication methods for AgNW based TERS probe, including AFM and STM based TERS probes. The AC-DEP method, the epoxy glue assisted method, the directly attached

method, and the directly manipulated by a micro-manipulator method have been introduced in the chapter 1.2.1.

2) The tip-substrate distance control methods, i.e. the AgNW based SPM, that include AFM and STM has been reviewed in chapter 1.2.2. Thanks to the large mechanical stiffness, the high aspect ratio, and the crystalized sharp tip of the chemical synthesis AgNWs, the AgNW based SPMs can provide ones with high spatial resolution and high aspect ratio for sample topography.

3) The different apexes of the AgNW based TERS probes have been reviewed in chapter 1.2.3. AgNWs apexes including crystalized sharp, etched ultra-sharp, round and heat induced nano-droplet profiles. Among those apexes, TERS probe enhancement factor and coupling efficiency influence the TERS contrast spontaneously, small diameter give enhancement factor and finer near-field energy distribution but with low coupling efficiency. Thus, the trade-off between high enhancement factor and high coupling efficiency is important for directly-excited TERS techniques.

4) The remote-excited TERS solved the indecisive trade-off by using a nano-antenna (the AgNW-AgNC bundle) to convert the incident laser into SPPs mode and propagate along AgNW toward the apex of AgNW sharp tip, nanoscale laser would re-scattered at the apex and generate enhance Raman signal. Comparing to the grating-assisted RE-TERS probe, the AgNW-AgNC bundle based RE-TERS probe have high reproducibility, high coupling efficiency and simple fabrication process and become a promising candidate for high spatial resolution and high TERS contrast nano-Raman imaging technique.

5) The two-step prism coupling and quasi-adiabatic nanofocusing AgNW based high external efficiency probe-in and probe-out TERS technique has been achieved 50% totally coupling efficiency and ~1nm spatial resolution.

The selected applications of AgNW based TERS imaging, including 1D and 2D materials, reviewed in the chapter 1.3. As the best test sample for benchmarking a TERS probe, SWCNTs have one reduced dimension on the sample surface that serve as a reversed probe to map the nano light source at a TERS probe apex. Several nanometer spatial resolution has been achieved in many AgNW based TERS experiments. Tensile strained monolayer MoS_2 flake on smooth gold substrate has been studied using a AgNW-AgNC bundle based remote-excited TERS probe and strain mapping has been shown and high TERS contrast was proved.

Although they just have 9 years history, we can conclude that the AgNW based TERS techniques have promising future because of their low-cost, high reproducibility and easy fabrication process.

1.5 Reference:

1. Schmid, T.; Opilik, L.; Blum, C.; Zenobi, R. *Angewandte Chemie International Edition* **2013,** 52, (23), 5940-5954.

2. Xia, L.; Chen, M.; Zhao, X.; Zhang, Z.; Xia, J.; Xu, H.; Sun, M. *Journal of Raman Spectroscopy* **2014,** 45, (7), 533-540.

3. Zrimsek, A. B.; Chiang, N.; Mattei, M.; Zaleski, S.; McAnally, M. O.; Chapman, C. T.; Henry, A.-I.; Schatz, G. C.; Van Duyne, R. P. *Chemical reviews* **2016,** 117, (11), 7583-7613.

4. Verma, P. *Chemical reviews* **2017,** 117, (9), 6447-6466.

5. Shi, X.; Coca-López, N. s.; Janik, J.; Hartschuh, A. *Chemical reviews* **2017,** 117, (7), 4945-4960.

6. Lee, J.; Crampton, K. T.; Tallarida, N.; Apkarian, V. A. *Nature* **2019,** 568, (7750), 78.

7. Zalevsky, Z. *Nature Photonics* **2013,** 7, (8), 593.

8. Wessel, J. *JOSA B* **1985,** 2, (9), 1538-1541.

9. Stöckle, R. M.; Suh, Y. D.; Deckert, V.; Zenobi, R. *Chemical Physics Letters* **2000,** 318, (1-3), 131-136.

10. Hayazawa, N.; Inouye, Y.; Sekkat, Z.; Kawata, S. *Optics Communications* **2000,** 183, (1-4), 333-336.

11. Anderson, M. S. *Applied Physics Letters* **2000,** 76, (21), 3130-3132.

12. Zhang, W.; Fang, Z.; Zhu, X. *Chemical reviews* **2016,** 117, (7), 5095-5109.

13. Veerman, J.; Otter, A.; Kuipers, L.; Van Hulst, N. *Applied Physics Letters* **1998,** 72, (24), 3115-3117.

14. Fei, Z.; Rodin, A.; Andreev, G.; Bao, W.; McLeod, A.; Wagner, M.; Zhang, L.; Zhao, Z.; Thiemens, M.; Dominguez, G. *Nature* **2012,** 487, (7405), 82.

15. Park, C.; Park, J.-H.; Rodriguez, C.; Yu, H.; Kim, M.; Jin, K.; Han, S.; Shin, J.; Ko, S. H.; Nam, K. T. *Physical review letters* **2014,** 113, (11), 113901.

16. Jordan, C. E.; Stranick, S. J.; Cavanagh, R. R.; Richter, L. J.; Chase, D. B. *Surface science* **1999,** 433, 48-52.

17. Zhang, R.; Zhang, Y.; Dong, Z.; Jiang, S.; Zhang, C.; Chen, L.; Zhang, L.; Liao, Y.; Aizpurua, J.; Luo, Y. e. *Nature* **2013,** 498, (7452), 82.

18. Ropers, C.; Neacsu, C.; Elsaesser, T.; Albrecht, M.; Raschke, M.; Lienau, C. *Nano letters* **2007,** 7, (9), 2784-2788.

19. De Angelis, F.; Das, G.; Candeloro, P.; Patrini, M.; Galli, M.; Bek, A.; Lazzarino, M.; Maksymov, I.; Liberale, C.; Andreani, L. C. *Nature Nanotechnology* **2010,** 5, (1), 67.

20. Berweger, S.; Atkin, J. M.; Olmon, R. L.; Raschke, M. B. *The Journal of Physical Chemistry Letters* **2010,** 1, (24), 3427-3432.

21. Ma, X.; Zhu, Y.; Yu, N.; Kim, S.; Liu, Q.; Apontti, L.; Xu, D.; Yan, R.; Liu, M. *Nano Letters* **2018,** 19, (1), 100-107.

22. Esmann, M.; Becker, S. F.; Witt, J.; Zhan, J.; Chimeh, A.; Korte, A.; Zhong, J.; Vogelgesang, R.; Wittstock, G.; Lienau, C. *Nature nanotechnology* **2019**, 1.

23. Agapov, R. L.; Sokolov, A. P.; Foster, M. D. *Journal of Raman Spectroscopy* **2013,** 44, (5), 710-716.

24. You, Y.; Purnawirman, N.; Hu, H.; Kasim, J.; Yang, H.; Du, C.; Yu, T.; Shen, Z. *Journal of Raman Spectroscopy* **2010,** 41, (10), 1156-1162.

25. Fujita, Y.; Chiba, R.; Lu, G.; Horimoto, N. N.; Kajimoto, S.; Fukumura, H.; Uji-i, H. *Chemical Communications* **2014,** 50, (69), 9839-9841.

26. Lu, G.; De Keersmaecker, H.; Su, L.; Kenens, B.; Rocha, S.; Fron, E.; Chen, C.; Van Dorpe, P.; Mizuno, H.; Hofkens, J. *Advanced Materials* **2014,** 26, (30), 5124-5128.

27. Walke, P.; Fujita, Y.; Peeters, W.; Toyouchi, S.; Frederickx, W.; De Feyter, S.; Uji-i, H. *Nanoscale* **2018,** 10, (16), 7556-7565.

28. Fujita, Y.; Walke, P.; De Feyter, S.; Uji-i, H. *Japanese Journal of Applied Physics* **2016,** 55, (8S1), 08NB03.

29. Brodard, P.; Bechelany, M.; Philippe, L.; Michler, J. *Journal of Raman Spectroscopy* **2012,** 43, (6), 745-749.

30. Dai, H.; Hafner, J. H.; Rinzler, A. G.; Colbert, D. T.; Smalley, R. E. *Nature* **1996,** 384, (6605), 147.

31. Yan, R.; Park, J.-H.; Choi, Y.; Heo, C.-J.; Yang, S.-M.; Lee, L. P.; Yang, P. *Nature nanotechnology* **2012,** 7, (3), 191.

32. Ma, X.; Zhu, Y.; Kim, S.; Liu, Q.; Byrley, P.; Wei, Y.; Zhang, J.; Jiang, K.; Fan, S.; Yan, R. *Nano letters* **2016,** 16, (11), 6896-6902.

33. Liu, Q.; Kim, S.; Ma, X.; Yu, N.; Zhu, Y.; Deng, S.; Yan, R.; Zhao, H.; Liu, M. *Nanoscale* **2019,** 11, (16), 7790-7797.

34. Binnig, G.; Rohrer, H.; Gerber, C.; Weibel, E. *Applied Physics Letters* **1982,** 40, (2), 178-180.

35. Vlassov, S.; Polyakov, B.; Dorogin, L. M.; Antsov, M.; Mets, M.; Umalas, M.; Saar, R.; Lõhmus, R.; Kink, I. *Materials Chemistry and Physics* **2014,** 143, (3), 1026-1031.

36. Umeda, N.; Ishikawa, Y.; Anzai, T. *JOURNAL-JAPAN SOCIETY FOR PRECISION*

ENGINEERING **1996,** 62, 1484-1488.

37. Zha, F.-X.; Czerw, R.; Carroll, D.; Kohler-Redlich, P.; Wei, B.-Q.; Loiseau, A.; Roth, S. *Physical Review B* **2000,** 61, (7), 4884.

38. Yu, J.; Saito, Y.; Ichimura, T.; Kawata, S.; Verma, P. *Applied Physics Letters* **2013,** 102, (12), 123110.

39. Yano, T.-a.; Ichimura, T.; Taguchi, A.; Hayazawa, N.; Verma, P.; Inouye, Y.; Kawata, S. *Applied Physics Letters* **2007,** 91, (12), 121101.

Chapter 2 Sharp-tip silver nanowires mounted on cantilevers for high-aspect-ratio high-resolution imaging

Despite many efforts to fabricate high-aspect-ratio atomic force microscopy (HAR-AFM) probes for high-fidelity, high-resolution topographical imaging of three-dimensional (3D) nano-structured surfaces, current HAR probes still suffer from unsatisfactory performance, low wear-resistivity, and extravagant prices. The primary objective of this work is to demonstrate a novel design of a high-resolution (HR) HAR AFM probe, which is fabricated through a reliable, cost-efficient bench-top process to precisely implant a single ultra-sharp metallic nanowire on a standard AFM cantilever probe. The force-displacement curve indicated that the HAR-HR probe is robust against buckling and bending up to 150 nN. The probes were tested on polymer trenches, showing a much better image fidelity when compared with standard silicon tips. The lateral resolution, when scanning a rough metal thin film and single-walled carbon nanotubes (SW-CNTs), was found to be better than 8 nm. Finally, stable imaging quality in tapping mode was demonstrated for at least 15 continuous scans indicating high resistance to wear. These results demonstrate a reliable bench-top fabrication technique towards metallic HAR-HR AFM probes with performance parallel or exceeding that of commercial HAR probes, yet at a fraction of their cost.

2.1 Introduction

As the progress of the technique of traditional nano-photonics and nano-electronic devices, the scanning probe microscopy (SPM), especially the atomic force microscopy (AFM)[1],

for nondestructive and rapid topographical characterization of nanostructured 3D surfaces has been demanded more. However, recently, there are emerging some novel 3D nano-devices, such as photonic crystals with subwavelength hole arrays[2] and fin-based multi-gates transistor architectures (like FinFETs, round channel FETs)[3], usually have both high aspect ratios and lateral features need to be detailed. Due to the needs of those high-aspect-ratio high-resolution (HAR-HR) topographical imaging of those 3D nano-structures, AFM probes should have not only a high aspect ratio (>10:1) for deep trench access, but also a small apex radius for high spatial resolution. Although high aspect ratio scanning probes (better than 5:1) are commercially available, the fabrication of such probes usually requires advanced nano-manufacturing techniques, for example, or focused electron beam (FEB) induced deposition focused ion beam (FIB) deposition[4]. Thus, the succeed ratio is low and high cost. Meanwhile, the tips may be delicate and vulnerable to breakage while the probe do the approach process because of the limited choices of deposition materials and high density of crystal defects introduced during FIB/FEB deposition processes. In addition, the low war resistance of the probes may introduce some instability during the AFM image scanning.[5]. Alternatively, carbon nanotubes (CNTs) attached to AFM cantilever has been demonstrated for HAR-HR imaging[6-8]. However, this technique requires complicated fabrication process and time-consuming, which resulting in low throughput and higher price. Therefore, a low-cost, time-saving, high reproducibility and through bench-top fabrication technique for HAR-HR AFM probes is in urgent demand for “high fidelity” imaging of 3D nanostructures.

Besides CNT AFM probe, another variety of HAR nanostructures that are uniquely suitable for HAR-HR AFM tips are elemental or compound nanowires. Many different nanowires with aspect ratios larger than 100:1 can be synthesized by bottom-up methods with high uniformity, low-cost and in large scale. In addition, it is much easier to mechanical manipulate those nanowires comparing to CNTs. Because the individual nanowires can be observed by conventional optical microscopes directly and a 3D micro manipulator can be introduced to control a etched sharp tip tungsten probe to manipulate those nanowires.[9] This process can avoid the fabrication requirements for slow and expensive cleanroom processes required by CNTs-based probes. The assembly of nanowires on conventional AFM cantilevers has been previously tested as HAR-AFM probes[10, 11]. However, due to the large nanowire tip radius, the low spatial resolution for those nanowire attached on AFM cantilever probes has been becomes their major drawback. For instance, due to the attachment of metallic catalyst nanoparticles, semiconductor nanowires synthesized by chemical vapor deposition (CVD) methods usually have one end with rounded tip profiles with large tip radius[12]. Although better than the naturally flat tips of semiconductor nanowires, these catalyst particles are usually have size between tens to hundreds of nanometers leading to the poor imaging spatial resolution. Recently, a self-assembly method to grow Ag_2Ga alloy nanowires directly on AFM cantilevers has been developed[13]. This method still makes nanowires radius be rounded (tip radius 25-100 nm) or even flat ends, which still limited AFM spatial resolution.

In this chapter, we introduced an economical fabrication method for AFM probes that make the AFM image with both high-aspect-ratio (HAR) and high resolution (HR), by attaching

sharp-tip silver nanowires (AgNW) (tip radius down to 5 nm) on the standard commercial AFM cantilevers, which are synthesized through a low-cost, wet chemical process, scalable method as shown in **Figure 2.1 a**. **Figure 2.1 b** shows the scanning electron microscopy (SEM) image of the probe. The typical protruding length of the AgNW from the cantilever tip is around 3-5 μm to maintain a high aspect ratio in the range of 40:1-70:1 and preventing bending/buckling during the approach process effectively. The sharp-tip AgNW (in the inset of **Figure 1b**) shows the diameter is around 70 nm and tip radius is around 8 nm.

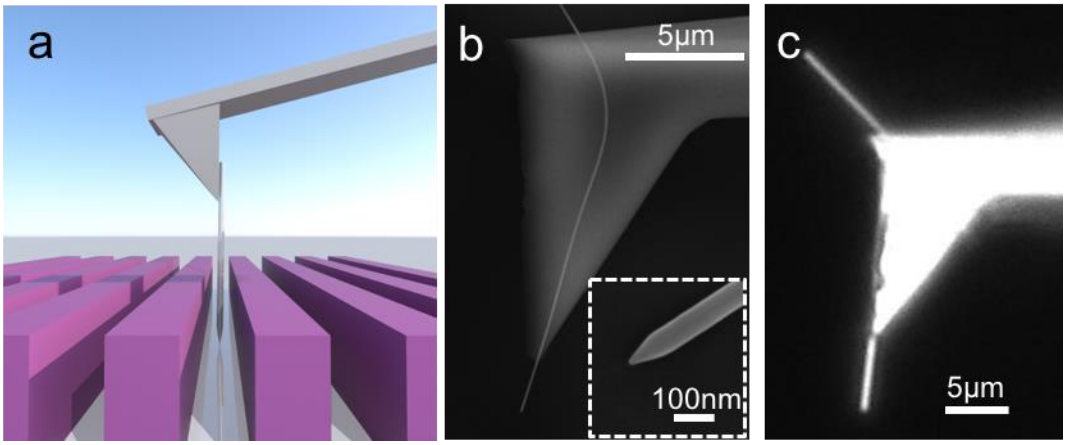

Figure 2.1 Schematic of sharp tip AgNW based AFM **a**, Schematic illustration of the AgNW probe for deep-trench topographical imaging. b, SEM image of an AgNW probe. Inset: Close-up SEM image of the sharp AgNW tip. The tip radius of the AgNW was 5 nm. c, Dark-field optical image of the probe.

2.2 Probe fabrication

The AgNW HAR-HR AFM probe was fabrication process is adhering an AgNW onto the side wall of a conventional silicon AFM cantilever (Olympus, Model# AC160TS-R3) which shape is the pyramidical tip, through a bench-top manipulation procedure that has been introduced the previously developed[9]. First, the AgNWs were dispersed onto a fresh

polydimethylsiloxane (PDMS) substrate, then using the dark-field of an upright optical microscope imaging system (Nikon Eclipse 80i, integrated with an Andor® Zyla sCMOS Camera) to examine the quality of the AgNWs (the examination method will be introduced in the next set of this chapter). The next step, a tungsten probe controlled by a motorized 4-axis micromanipulator (MP-285, Sutter Instrument®, 40 nm resolution) was used to pick up the target AgNW, followed by placing it in the desired position on the pyramidical tip, and finely adjust the protruding length by gently pushing along the nanowire. **Figure 2.2** shows that the protruding length could be fine controlled. After the nanowire had been mounted, due to the attractive Van der Waals' force between the AgNW and the side of the AFM cantilever is not enough, we used another tungsten probe to apply a small amount of epoxy glue on the AgNW-cantilever junction to improve the adhesion and prevent the detachment of AgNW during the tapping-mode measurement. **Figure 2.1 c** shows a dark-field optical microscope image of an AgNW probe that is ready for AFM mapping.

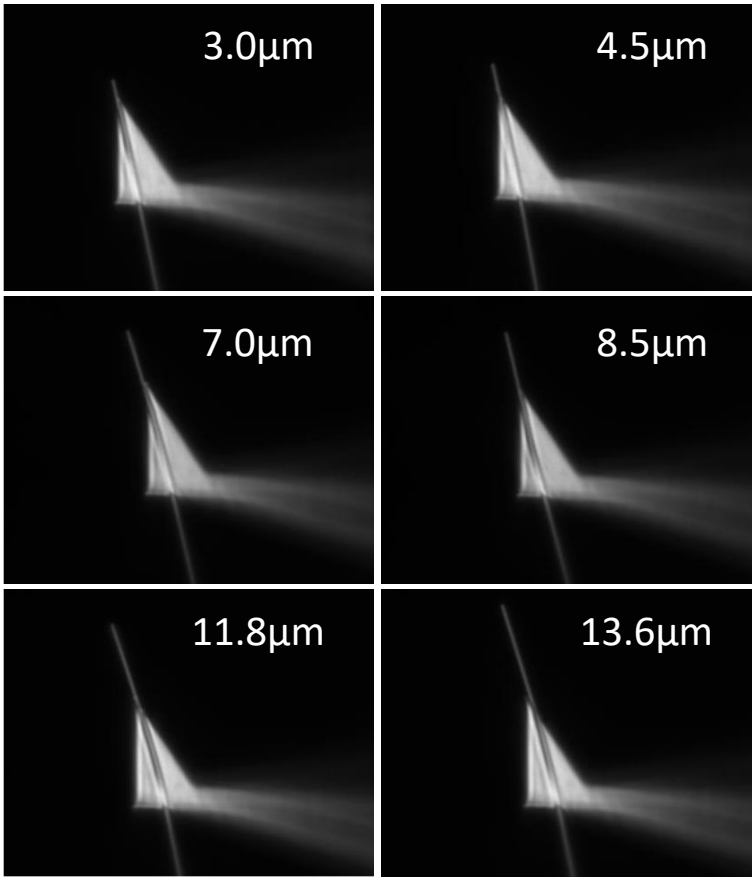

Figure 2.2 The AgNW protruding length on the cantilever was able to be controlled.

2.3 Synthesis of sharp-tip AgNWs

The AgNWs were synthesized with a modified polyol reduction method, which is known to produce high quality, uniform AgNWs and is large throughput to meet the requirement of the industrial manufacturing needs. Due to their high crystallinity, low defect level and atomically flat surfaces, such AgNWs have outstanding mechanical, electrical, and optical properties. It has been demonstrated a wealth of applications, such as flexible/stretchable electronics[14, 15], plasmonic applications which including surface enhanced Raman

spectroscopy (SERS)[16] and subwavelength optoelectronics[17]. Unlike the bulk silver, crystalline AgNWs have improved mechanical properties, a 160 Gpa of Young's modulus has been measured by the strain-stress measurements[18, 19], which is 3 times larger than bulk silver and exceeds that of silicon nanowires. Although their vulnerability to oxidation as an obvious shortcoming of AgNWs, surface protective coatings, such as a thin layer of Al_2O_3 via atomic layer deposition (ALD) or a conformal Au coating through solution phase deposition can be alleviated.

Unlike some semiconductor nanowires (such as Si nanowires), the AgNWs has the unique features are their naturally pointed tips and the tunability of their tip morphologies. Chemically synthesized AgNWs are five-fold twinned with vertical twin boundaries (TBs) meeting at the central axis of the nanowire. The five-fold vertical twinning guides the formation of their pentagonal pyramidal ends, as illustrated in **Figure 2.3** (SEM pictures in **Figure 2.4**). These pointed ends are capped with five (111) facets oriented radially about the central axis of the nanowire. Each of these (111) facets has two sides in contact with its neighbors with a dihedral angle of ~70.5°[20]. The five (111) facets join at the tip with a taper angle of ~120° (**Figure 2.4**). Depending on the synthesis condition, the tip shape may not be rigidly polyhedron, but can be rounded due to oxidative dissolution[20, 21] to form an elliptical tip (**Figure 2.4**) with a tip radius of roughly half of the nanowire diameter (**Figure 2.3 b**, i-iii). As an example, a nanowire with a 100 nm diameter, would have a tip radius (R) of ~50 nm.

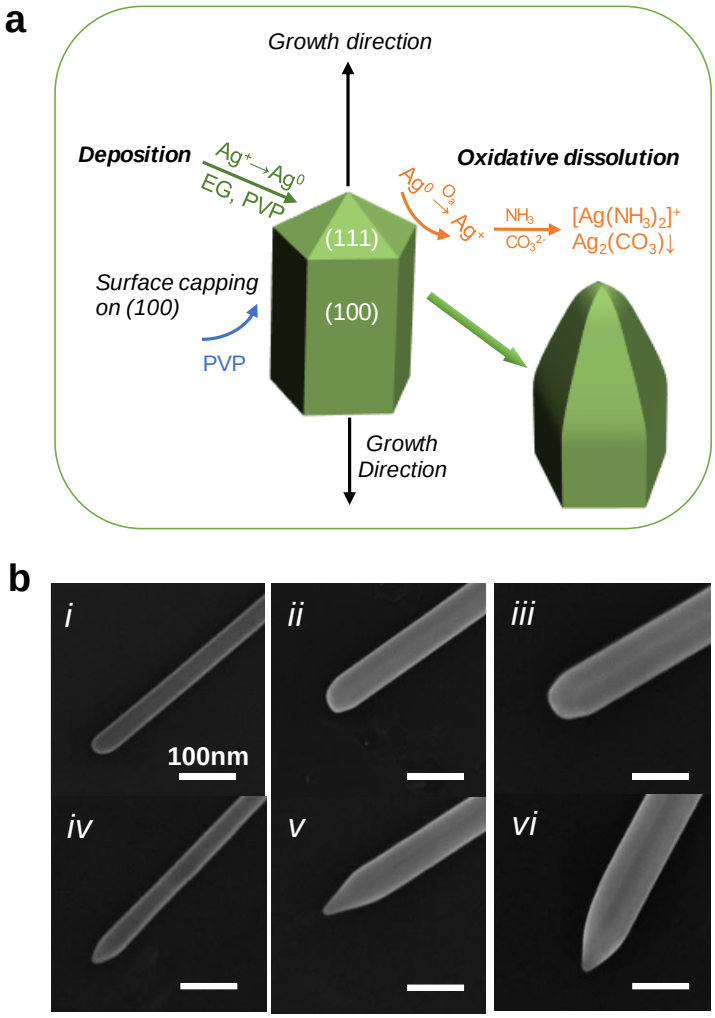

Figure 2.3 The fabrication of ultra-sharp tip AgNW **a,** Schematic illustration of the dynamic deposition and dissolution processes of Ag atoms at the sharpened tips of AgNWs. O_a: adsorbed O atoms. **b,** SEM images of regular AgNWs (top row) and AgNWs with sharpened tips (bottom row) with different diameters. From left to right, the AgNW diameters are 40nm (i, iv), 70nm (ii, v) and 90 nm (iii,vi), respectively.

While the pyramidal or rounded tips give these chemically synthesized AgNWs a natural advantage for high-resolution AFM imaging over semiconductor NWs with flat tips, to achieve the sub-10 nm AFM lateral resolution, the AgNW tips must be further sharpened to reduce tip radii. This can be accomplished by deliberately amplifying the oxidative

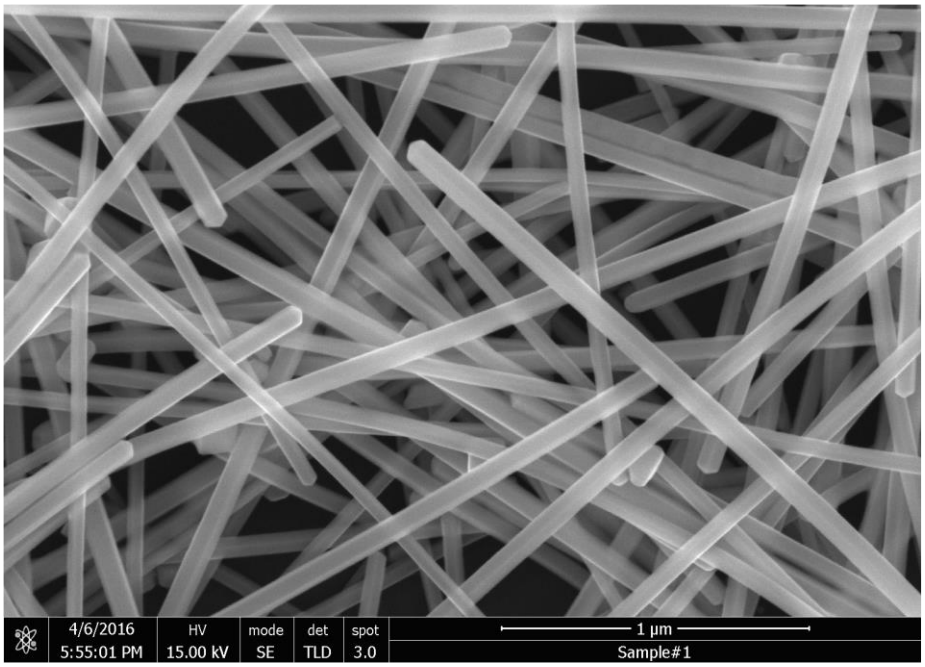

Figure 2.4 SEM image of regular AgNWs that show pentagonal pyramidal or rounded (yellow circles) tips.

dissolution at the TBs between the (111) facets at the AgNW tip[21, 22]. As illustrated in **Figure 2.3 a**, the one-dimensional growth of AgNWs is driven by two factors: (1) the formation of seeds with multiple TBs, where significant lattice distortion, surface relaxation and defects occur[20, 23, 24] to provide high-energy sites for atomic addition to feed the fast axial growth along the TBs[20, 25]; (2) the inhibition of lateral growth on the (100) side walls by capping agent poly(vinyl pyrrolidone), or PVP, which binds more strongly to the (100) side surfaces, rather than with the (111) ends[26]. At the same time, the presence of air in the reaction solution could also lead to preferential oxidative dissolution or "etching" (**Figure 2.3 a**, curved orange arrow) at the highly reactive TBs near the AgNW tip. This is caused by the adsorption and dissociation of molecular oxygen on the Ag surface[27-29] to form surface adsorbed oxygen atoms (O_a), which oxidize Ag^0 atoms at the nanowire

surfaces and release Ag^0 back to the growth solution as Ag^+. Such oxidative etching happens preferentially at the tips due to the weak PVP binding on (111) facets, and also at TBs due to their high reactivity. As a result, the original sharp edges formed by TBs between the (111) facets at the AgNW tips become rounded. By introducing coordination regents, such as NH_3 and CO_3^{2-} used in the current study, to reduce the Ag^+ concentration and drive the $Ag^0 \rightarrow Ag^+$ oxidative dissolution reaction forward, the etching effect on the tip TBs can be further amplified to form ultra-sharp nanowire tips (**Figure 2.3 a**). **Figure 2.3 b** shows the effect of amplified oxidative etching on AgNW tip morphologies. The top panels (**Figure 2.3 b**, i-iii) are AgNWs of different diameters (40, 70 and 90 nm, respectively) synthesized with conventional polyol synthesis in air. The nanowire tips are rounded due to natural oxidative etching from dissolved oxygen in the growth solution. The bottom panels (**Figure 2.3 b**, iv-vi) are ultra-sharp-tip AgNWs synthesized through the addition of $(NH_4)_2CO_3$ to the growth solution, while other growth parameters were kept the same. NH_4^+ dissociates to release NH_3, which then coordinates with Ag^+ to form the silver-amino complex ion $Ag(NH_3)_2^+$, while CO_3^{2-} combines with Ag^+ to form Ag_2CO_3(s) due to its low solubility, both effectively reducing the Ag^+ concentration in the growth solution to accelerate the oxidative etching. The sharpening effect seen in **Figure 2.3 b** (iv-vi) was consistent for AgNWs of different diameters. **Figure 2.5** shows a series of SEM images of the ultra-sharp tip AgNW sample purified through centrifugation. The purified AgNW sample was used in all subsequent AFM imaging and has a uniform diameter of 70±7 nm and an average tip radius of 9±5 nm.

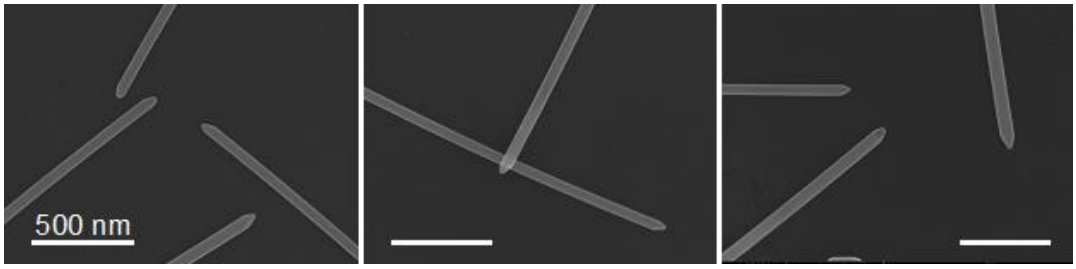

Figure 2.5 SEM images of purified ultra-sharp-tip AgNWs with an average diameter of 70 nm showing narrow diameter distribution and consistent tip morphology.

2.4 Mechanical properties of the AgNW HAR-HR AFM probe

The AgNW HAR-HR AFM probe was fabricated by adhering an AgNW onto the side wall of the pyramidical tip of a conventional silicon AFM cantilever (Olympus, Model# AC160TS-R3) through a bench-top manipulation procedure that is similar to what we have previously developed[9]. First, the AgNWs were dispersed onto a fresh polydimethylsiloxane (PDMS) substrate, and examined with an upright optical microscope imaging system (Nikon Eclipse 80i, integrated with an Andor® Zyla sCMOS Camera) to locate the AgNWs with proper lengths. Then a tungsten probe mounted on a motorized 4-axis micromanipulator (MP-285, Sutter Instrument®, 40 nm resolution) was used to pick up the target AgNW, place it in the desired position on the pyramidical tip, and finely adjust the protruding length by gently pushing along the nanowire. The protruding length can be controlled with a 0.5 μm accuracy, to adjust the aspect ratio of the probe to meet the measurement requirements. After the nanowire had been mounted, we used another tungsten probe to apply a small amount of epoxy glue on the AgNW-cantilever junction to improve the adhesion and prevent the detachment of AgNW during the tapping-mode

measurement. **Figure 2.1 c** shows a dark-field optical microscope image of an AgNW probe that is ready for measurement.

The attachment of the AgNW has little influence on the dynamic response property of the AFM cantilever. As shown in Fig. 3a, the resonance frequency f only showed a marginal decrease of 0.03% (0.1 kHz) after the AgNW attachment. This result indicates that the total added mass from the AgNW and the epoxy glue ($\Delta m = m_{Ag} + m_{glue}$) is negligible compared to the effective mass (m_{eff}) of the silicon cantilever. The mass of a typical AgNW is on the order of pico-gram, and the amount of epoxy glue applied was carefully minimized to ensure a much smaller Δm than m_{eff}, which can be derived from the resonance frequency (f) and the spring constant (k) of the cantilever via

$$f = \frac{1}{2\pi}\sqrt{\frac{k}{m_{eff}}} \qquad \textbf{eq. 2.1}$$

For the cantilever used here (k ~ 26 N/m), m_{eff} is found to be around $6 \times 10^{-9} g$. Using the first order approximation, Δm can be derived from the change of the resonance frequency Δf, as $\Delta m = -\frac{2\Delta f}{f} m_{eff}$. For the probe measured in **Figure 3a**, Δm is ~$3 \times 10^{-12} g$, which is about 3 orders smaller than the mass of the cantilever. As a result, the performance of the cantilever can be largely maintained, as evidenced by the mechanical quality factor Q, which was reduced marginally from 307 to 281 after the AgNW adhesion.

The force-displacement curve measurement was conducted on a quartz substrate to characterize the mechanical property of the AgNW HAR-HR probe. **Figure 2.6 b** shows a

typical force-displacement curve during indenting and pulling of an AgNW probe with 3 μm protruding length, measured on a commercial AFM instrument (SmartSPM, AIST-NT, Inc). When the AgNW was approaching the substrate from afar, the force curve showed a flat zero line (**Figure 2.6 b and d**, i), with a tiny cantilever deflection observed near zero displacement. After the AgNW had touched the substrate, the force curve showed a linear increase up to 150 nN, at the slope of the cantilever spring constant (~26 N/m), implying that the AgNW was not bent within this range (**Figure 2.6 b and 2.6 d**, ii). Two detaching steps were found when the substrate was retracted from the tip. The first step (**Figure 2.6 b and 2.6 d**, iii) corresponded to the onset of a forward sliding motion of the AgNW tip on the substrate, as depicted in **Figure 2.6 d**, iv. Since the sliding friction is smaller than the maximum static friction between the AgNW tip and the substrate, a weaker net attractive force was needed during the sliding process, which was reflected by the plateau with a smaller negative force value in **Figure 2.6 b**, iv. The second step (**Figure 2.6 b and 2.6 d**, v) was the detachment of the bent AgNW from the substrate. Assuming that the AgNW was nearly vertical at the detaching point, we can estimate the tilt angle θ from the equation $d = L(1 - \cos\theta)$, where d is the substrate displacement during the sliding process and L is the protruding length. For the probe in **Figure 2.6**, where the AgNW was aligned with the outer edge of the cantilever, θ was found to be ~7˚, which is close to the tip angle ofthe cantilever mount. This result suggests that it is possible to further minimize the tilt angle between the AgNW and the normal vector of the substrate by choosing cantilever mounts with proper geometries.

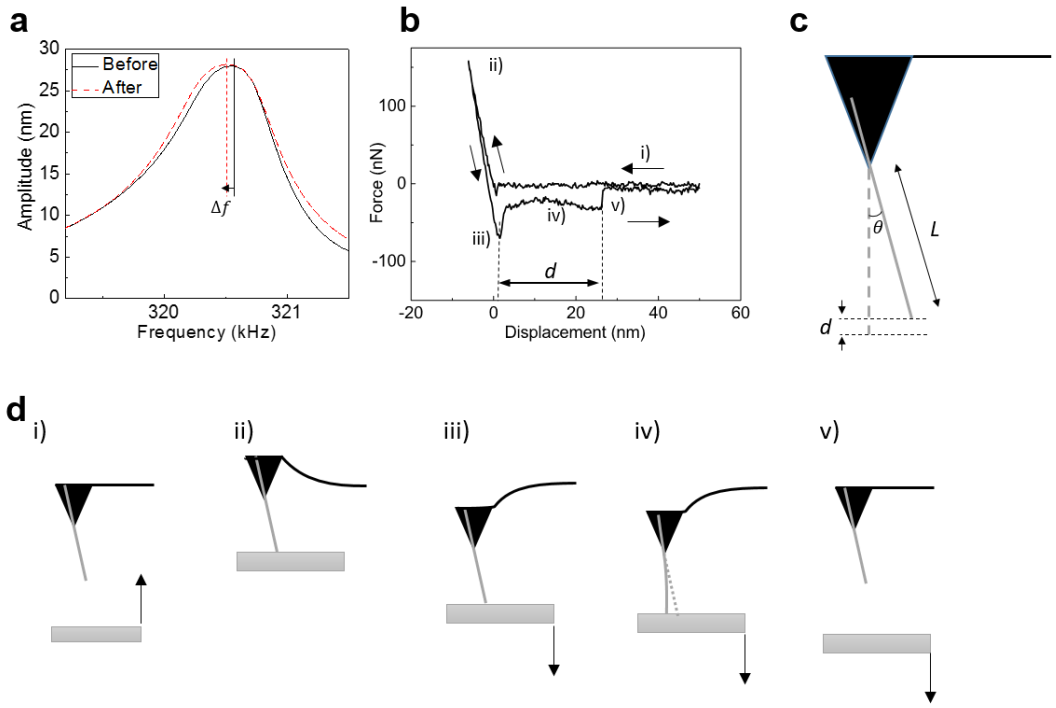

Figure 2.6 Mechanical characterization of an AgNW probe. **a**, Frequency response curves of cantilevers before (solid black curve) and after (dashed red curve) the attachment of AgNW. **b,** Force-distance curves during approach and retraction from a quartz substrate using the AgNW probe. **c** and **d,** Schematic diagrams illustrating the probe and the proposed events during the force-distance test. i) Substrate approaches. ii) Cantilever bends upward. iii) Cantilever bends downward, and the AgNW sticks to the substrate. iv) and v) the AgNW starts to slide on the substrate, and pulls off.

2.5 Performance of the AgNW HAR-HR AFM probe

To evaluate the performance of the AgNW HAR-HR tip, spatial resolution, robust, and deep trench measurement have been carried out.

2.5.1 Au film surface grain boundaries to demonstrate the AFM spatial resolution

To evaluate the spatial resolution of the AgNW HAR-HR tip, we chose a gold thin film with a rough surface as the imaging sample. The Au thin film was prepared by electron-beam thermal deposition of a 20 nm-thick Au film on a silicon dioxide substrate, with a 2

nm chromium (Cr) wetting layer underneath to improve the adhesion. Grains and gaps on the scale of several to tens of nanometers exist on the film surface due to the aggregation of Au atoms during the deposition, as shown in the SEM image (**Figure 2.7 d**). **Figure 2.7 (a-c)** present the tapping mode scanning images obtained with the AgNW HAR-HR probe, corresponding to the height, magnitude and phase images measured from the same area of the sample, respectively. The AFM images show islands and gaps with lateral dimensions that correspond well with the SEM image. The smallest gap size on the AFM image was around 8 nm.

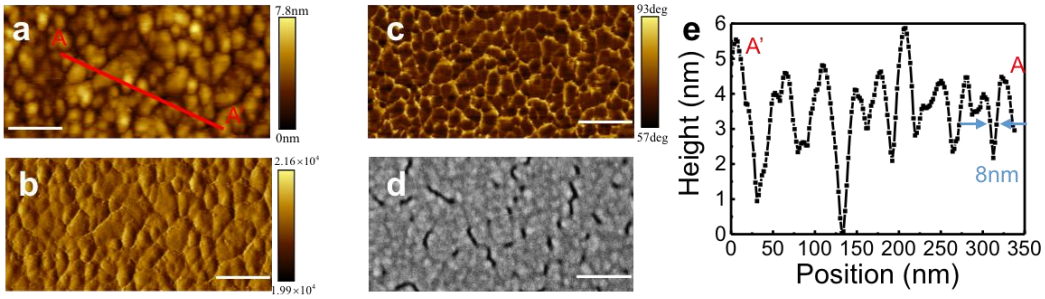

Figure 2.7 Tapping mode AFM topography images of a 20-nm thick gold film prepared by electron beam thermal deposition on a quartz substrate. **a-c,** are height, magnitude and phase imaging, respectively. **d** is a SEM image of a similar region of the same sample. **e** The line cut section analysis of (a). All scale bars are 100 nm. Image resolution, 440 by 220 pixels; Pixel resolution, 2nm; Scan rate, 1Hz; Oscillation amplitude, 20nm; Set-point, 87%, gain: 192.

2.5.2 Single-walled carbon nanotubes (SW-CNTs) AFM imaging to demonstrate the AFM probe robust

Image reproducibility is another important benchmark to evaluate the imaging performance and longevity of AFM probes, especially for metallic AFM tips. Studies have shown that traditional metallic probes with metal coatings such as Pt, Au, and Co usually have relatively low wear resistance due to the low hardness of the sputtered metals[30], although

they are widely needed for tip-enhanced Raman spectroscopy (TERS)[31] and covalent bonding to bio-molecules for biology applications[32]. Tip wear can be reflected in the AFM data, in particular, the AFM image quality[33]. Due to the high crystal quality of the chemically synthesized AgNW, the HAR-HR probe has a high wear-resistance. This can be experimentally evaluated by comparing the quality of a series of images continuously acquired from a CVD-grown single-walled carbon nanotube (CNT) sample over time[34]. As shown in **Figure 2.8**, a high spatial resolution of ~6 nm can be consistently achieved for at least 15 continuous scans, indicating excellent image reproducibility and high resistance of AgNWs to tip wear/damage. **Figure 2.9** shows the complete continuously scan to test the robust of this AgNW HAR-HR probe.

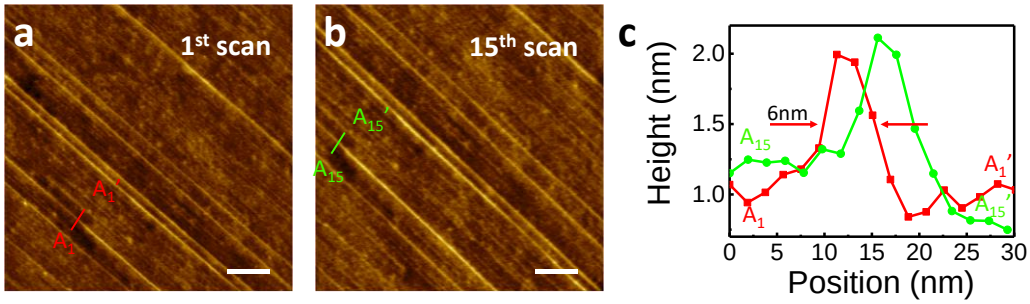

Figure 2.8 Continuous tapping mode imaging of a single-wall carbon nanotube array sample prepared by chemical vapor deposition method on a quartz substrate. **a,** and **b,** are the height images of the 1st and the 15th scanning. All scale bars are 100nm.

Image resolution, 400 by 400 pixels; Pixel resolution, 2nm; Scan rate, 1Hz; Oscillation amplitude, 20nm; Set-point, 87%, gain: 192.

2.5.3 PMMA deep trench mapping to demonstrate the AFM probe high-aspect ratio mapping ability

To demonstrate the capability of the AgNW probe for high fidelity imaging of 3D HAR samples, we fabricated a poly-methyl methacrylate (PMMA) grating through electron

beam lithography. The grating consists of 1100nm–deep, 600nm-wide trenches. **Figure 2.11** presents the AFM images obtained using the AgNW probe and a brand new standard commercial tapping-mode AFM probe for performance comparison. The commercial AFM probe tested here was the same model as the one used to mount the AgNW (Olympus, Model# AC160TS-R3), so that the specifications of the cantilevers in the two cases are identical. This comparison clearly shows that the AgNW probe delivered higher-fidelity trench images with no smearing effect on the edges that existed in the case of the commercial probe. The high aspect ratio of the AgNW probe followed the trench profile precisely (**Figure 2.10 c**), and faithfully revealed the details of the trench bottom. This is particularly obvious in the phase (**Figure 2.10 b**) and magnitude (**Figure 2.11**) images. The commercial probe reached only 800 nm into the trench and showed V-shaped profiles, which were the duplications of the probe cross-section. In order to show the origin real morphology of the PMMA deep trench, the sample was cross cropped and the sectional view SEM image is shown in **Figure 2.12**.

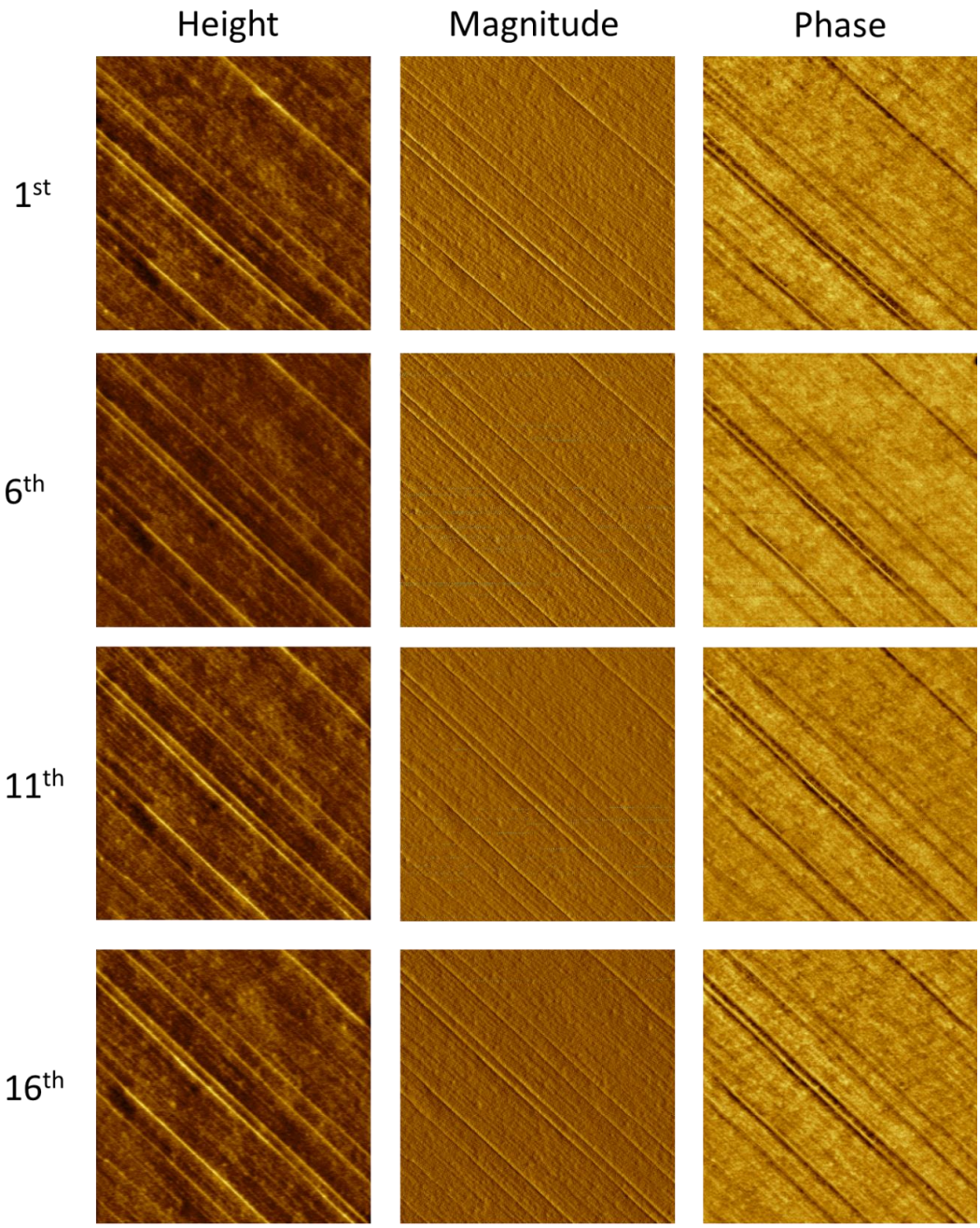

Figure 2.9 Additional images of continuous tapping mode scanning.

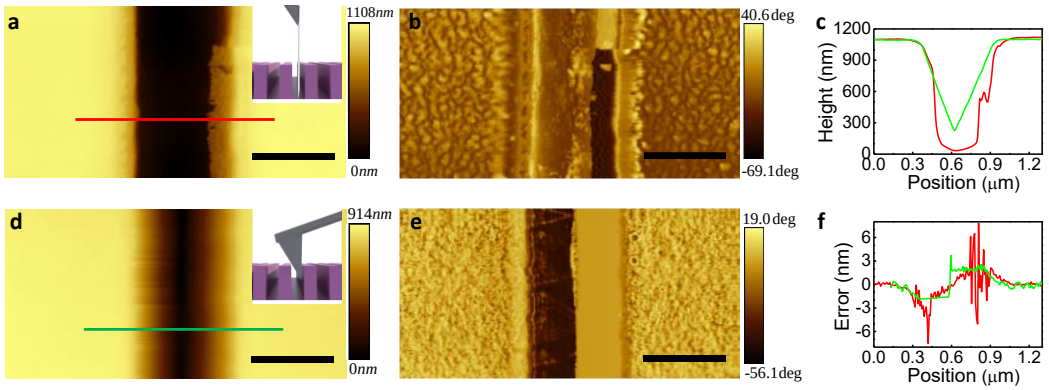

Figure 2.10 Comparison between an AgNW probe and a bare pyramidal silicon probe on a PMMA trench sample (width, 600nm; depth, 1100nm). **a,** and **b,** the height and the phase images acquired with the AgNW probe. **d,** and **e,** are prepared by a conventional AFM probe on the same sample. Scale bar: 500nm. **c,** and **f,** height and error line scans. Image resolution, 256 by 128 pixels; Scanning area, 2μm by 1μm; Scan rate, 1Hz; Oscillation amplitude, 20nm; Set-point, 87%, gain, 194.

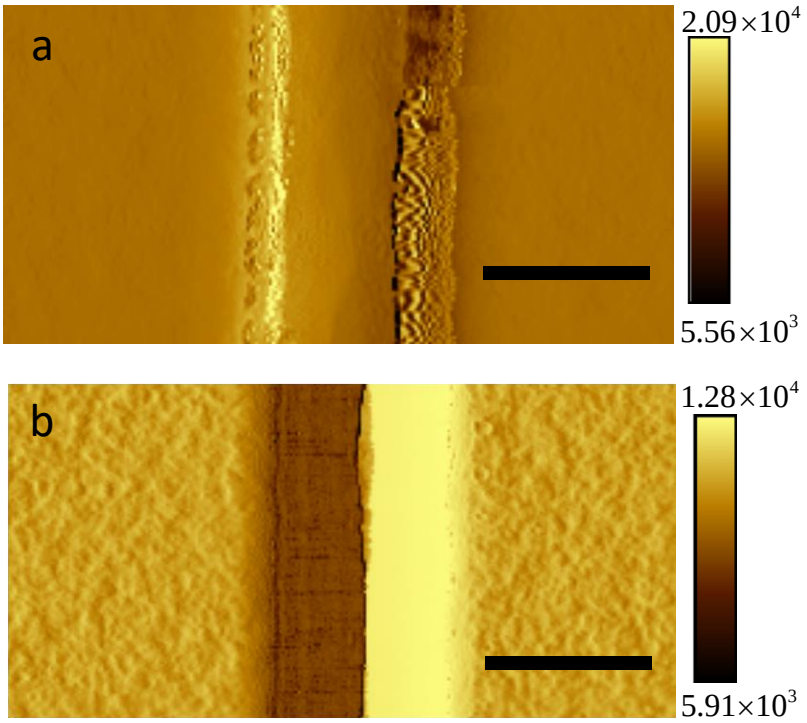

Figure 2.11 Error images for the trench sample corresponding to that in Figure 6. **a,** was obtained by an AgNW probe, and **b,** by a conventional AFM probe. Scale bar, 500nm.

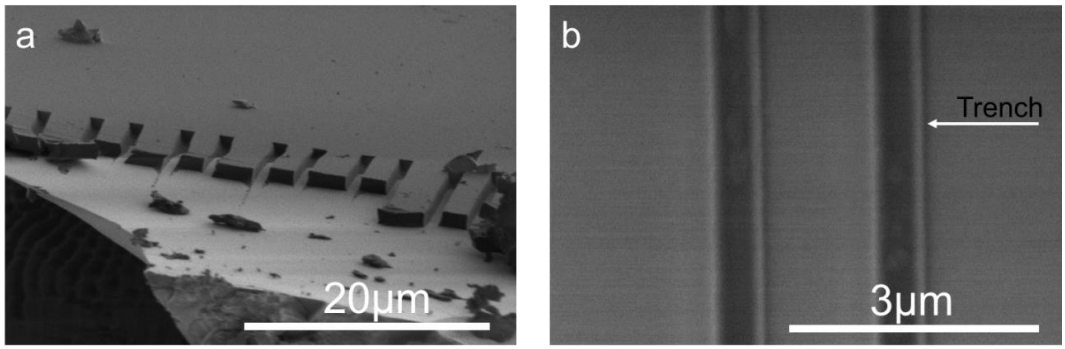

Figure 2.12 The perspective and top-view SEM images of the PMMA deep trench.

2.6 References

1. Haugstad, G., *Atomic force microscopy: understanding basic modes and advanced applications*. John Wiley & Sons: 2012.

2. Priolo, F.; Gregorkiewicz, T.; Galli, M.; Krauss, T. F. *Nat Nanotechnol* **2014,** 9, (1), 19-32.

3. Tang, X. H.; Bayot, V.; Reckinger, N.; Flandre, D.; Raskin, J. P.; Dubois, E.; Nysten, B. *Ieee T Nanotechnol* **2009,** 8, (5), 611-616.

4. Utke, I.; Hoffmann, P.; Melngailis, J. *J Vac Sci Technol B* **2008,** 26, (4), 1197-1276.

5. Lantz, M. A.; Wiesmann, D.; Gotsmann, B. *Nat Nanotechnol* **2009,** 4, (9), 586-591.

6. Dai, H. J.; Hafner, J. H.; Rinzler, A. G.; Colbert, D. T.; Smalley, R. E. *Nature* **1996,** 384, (6605), 147-150.

7. Burt, D. P.; Wilson, N. R.; Weaver, J. M. R.; Dobson, P. S.; Macpherson, J. V. *Nano Lett* **2005,** 5, (4), 639-643.

8. Wilson, N. R.; Macpherson, J. V. *Nat Nanotechnol* **2009,** 4, (8), 483-491.

9. Yan, R. X.; Park, J. H.; Choi, Y.; Heo, C. J.; Yang, S. M.; Lee, L. P.; Yang, P. D. *Nat Nanotechnol* **2012,** 7, (3), 191-196.

10. Christiansen, S. H.; Becker, M.; Fahlbusch, S.; Michler, J.; Sivakov, V.; Andra, G.; Geiger, R. *Nanotechnology* **2007,** 18, (3), 035503.

11. Engstrom, D. S.; Savu, V.; Zhu, X. N.; Bu, I. Y. Y.; Milne, W. I.; Brugger, J.; Boggild, P. *Nano Lett* **2011,** 11, (4), 1568-1574.

12. Dasgupta, N. P.; Sun, J. W.; Liu, C.; Brittman, S.; Andrews, S. C.; Lim, J.; Gao, H. W.; Yan, R. X.; Yang, P. D. *Adv Mater* **2014,** 26, (14), 2137-2184.

13. Ma, X.; Zhu, Y.; Kim, S.; Liu, Q.; Byrley, P.; Wei, Y.; Zhang, J.; Jiang, K.; Fan, S.; Yan, R. *Nano letters* **2016,** 16, (11), 6896-6902.

14. Hu, L. B.; Kim, H. S.; Lee, J. Y.; Peumans, P.; Cui, Y. *Acs Nano* **2010,** 4, (5), 2955-2963.

15. Garnett, E. C.; Cai, W. S.; Cha, J. J.; Mahmood, F.; Connor, S. T.; Christoforo, M. G.; Cui, Y.; McGehee, M. D.; Brongersma, M. L. *Nat Mater* **2012,** 11, (3), 241-249.

16. Lu, G.; De Keersmaecker, H.; Su, L.; Kenens, B.; Rocha, S.; Fron, E.; Chen, C.; Van Dorpe, P.; Mizuno, H.; Hofkens, J.; Hutchison, J. A.; Uji-i, H. *Adv Mater* **2014,** 26, (30), 5124-5128.

17. Fang, Y. R.; Li, Z. P.; Huang, Y. Z.; Zhang, S. P.; Nordlander, P.; Halas, N. J.; Xu, H. X. *Nano Lett* **2010,** 10, (5), 1950-1954.

18. Narayanan, S.; Cheng, G. M.; Zeng, Z.; Zhu, Y.; Zhu, T. *Nano Lett* **2015,** 15, (6), 4037-4044.

19. Zhu, Y.; Qin, Q. Q.; Xu, F.; Fan, F. R.; Ding, Y.; Zhang, T.; Wiley, B. J.; Wang, Z. L. *Phys Rev B* **2012,** 85, (4), 045443.

20. Wiley, B.; Herricks, T.; Sun, Y. G.; Xia, Y. N. *Nano Lett* **2004,** 4, (9), 1733-1739.

21. Korte, K. E.; Skrabalak, S. E.; Xia, Y. N. *J Mater Chem* **2008,** 18, (4), 437-441.

22. Liu, S. H.; Sun, B. M.; Li, J. G.; Chen, J. L. *Crystengcomm* **2014,** 16, (2), 244-251.

23. Hofmeister, H.; Nepijko, S. A.; Ievlev, D. N.; Schulze, W.; Ertl, G. *J Cryst Growth* **2002,** 234, (4), 773-781.

24. Nepijko, S. A.; Ievlev, D. N.; Schulze, W.; Urban, J.; Ertl, G. *Chemphyschem* **2000,** 1, (3), 140.

25. Gai, P. L.; Harmer, M. A. *Nano Lett* **2002,** 2, (7), 771-774.

26. Sun, Y. G.; Mayers, B.; Herricks, T.; Xia, Y. N. *Nano Lett* **2003,** 3, (7), 955-960.

27. Campbell, C. T. *Surf Sci* **1985,** 157, (1), 43-60.

28. deMongeot, F. B.; Cupolillo, A.; Valbusa, U.; Rocca, M. *Chem Phys Lett* **1997,** 270, (3-4), 345-350.

29. Sexton, B. A.; Madix, R. J. *Chem Phys Lett* **1980,** 76, (2), 294-297.

30. Chung, K. H. *Int J Precis Eng Man* **2014,** 15, (10), 2219-2230.

31. Huth, F.; Chuvilin, A.; Schnell, M.; Amenabar, I.; Krutokhvostov, R.; Lopatin, S.; Hillenbrand, R. *Nano Lett* **2013,** 13, (3), 1065-1072.

32. Lee, K. B.; Lim, J. H.; Mirkin, C. A. *J Am Chem Soc* **2003,** 125, (19), 5588-5589.

33. Liu, J. J.; Notbohm, J. K.; Carpick, R. W.; Turner, K. T. *Acs Nano* **2010,** 4, (7), 3763-3772.

34. He, Y. J.; Zhang, J.; Li, D. Q.; Wang, J. T.; Wu, Q.; Wei, Y.; Zhang, L. N.; Wang, J. P.; Liu, P.; Li, Q. Q.; Fan, S. S.; Jiang, K. L. *Nano Lett* **2013,** 13, (11), 5556-5562.

Chapter 3 Toward high-contrast AFM-TERS imaging: nano-antenna-mediated remote-excitation on sharp-tip silver nanowire probes

The tip-enhanced Raman spectroscopy (TERS) imaging technique is designed to provide correlated morphological and chemical information with a nanoscale spatial resolution by utilizing the plasmonic resonance supported by metallic nanostructures at the tip apex of a scanning probe. However, limited by the scattering cross-sections of these nanostructures, only a small fraction of the incident light can be coupled to the plasmonic resonance to generate Raman signals. The uncoupled light then directly excites background spectra with a diffraction-limited resolution, which becomes the background noise that often blurs the TERS image. Here, we demonstrate how this problem can be solved by physically separating the light excitation region from the Raman signal generation region on the scanning probe. The remote-excitation TERS (RE-TERS) probe, which can be fabricated with a facile, robust and reproducible method, utilizes silver nanoparticles as nano-antennas to mediate the coupling of free-space excitation light to propagating surface plasmon polaritons (SPPs) in a sharp-tip silver nanowire to excite Raman signals remotely.

3.1 Introduction

Scanning probe microscopies (SPM), such as scanning tunneling microscopy (STM) and atomic force microscopy (AFM), have become powerful tools for acquiring morphology information of nanostructured surfaces with atomic resolutions, but offer limited insights

into their surface chemistry. On the other hand, far-field optical spectroscopies, such as Raman or Fourier-transform infrared spectroscopy (FTIR), are widely used to investigate chemical bonds and molecular interactions. Their spatial resolutions, however, are orders of magnitude lower, dictated by the diffraction limit of the excitation light. Combining these two technologies has led to the development of tip-enhanced Raman/FTIR spectroscopy (TERS and nano-FTIR) imaging techniques[1-8], which bear the potential for chemical analysis of complex nanoscale surfaces down to the single molecule resolution[9]. In these applications, the tip apex of a metal probe, typically tens of nanometers in curvature, serves as a plasmonic antenna to amplify the intensity of both the incident light (i.e. excitation) and the Raman-scattered light (i.e. signal), and confines them to a nanoscale mode volume to achieve a spatial resolution defined by the curvature of the tip apex. However, since the excitation efficiencies of plasmonic nanostructures are generally small, only a tiny fraction of the incident power can be concentrated at the tip. The uncoupled light can still excite Raman scattering processes on the sample with low spatial resolution, which not only generates background noises that reduces the signal-to-noise ratio but also increases the chance of sample photo-degradation, giving the fact that strong laser is often used to pump the TERS signal. To tackle these problems, grating-assisted plasmonic-nanofocusing probes have recently emerged as a promising solution for low-background-noise TERS acquisition[10-12]. In these designs, the incident light is converted to SPPs through grating couplers that are fabricated on the probe sidewall a few microns away from the probe apex. Depending on the coupler design, coupling efficiencies have been achieved between 0.1~9%. The excited SPPs propagate toward the probe apex along the

tapered probe and become further compressed by the conical geometries for high-spatial-resolution near-field imaging. Since the SPP excitation region is separated from the Raman acquisition region, the Raman noise from the uncoupled incident light is drastically reduced.

Compared with other TERS techniques, grating-assisted nanofocusing skips the noise reduction steps, such as the background subtraction method or the modulation method[13], and has been used in a broad spectrum of research topics, ranging from optical nano-imaging[14], Raman analysis[11], to nanoscale ultrafast optics[15]. However, the reproducibility of the grating-assisted probes has been the primary challenge to this technique. For example, annealed gold wires, which are the preferred material for fabricating grating-assisted probes due to their high crystallinity and low plasmonic loss, suffer from the low mechanical stiffness as a result of the annealing[16]. The intricate balance between the mechanical stiffness and optical quality of the gold wires requires meticulous control over annealing conditions. Equally tricky is the precise control over the electrochemical etching process used to taper the nanowire (NW) tip, the exact geometry and surface roughness of which is critical for the efficiency of plasmonic nanofocusing and TERS enhancement[17].

Compared with gold, silver is more favorable for TERS experiments due to its stronger plasmonic enhancement and lower fluorescence background. Chemically synthesized crystalline silver nanowires (AgNWs), in particular, is uniquely suited for TERS, due to their nanoscale field confinement[18, 19], mechanical robustness and low plasmonic loss[20, 21], the latter of which both stemming from their poly-twined crystalline nature. In addition, AgNW SPPs can be excited easily using a variety of methods, from prism or grating

couplers[22], near-field coupling[21, 23, 24], to as simple as tip, defect and nano-antenna scattering[25, 26], making them uniquely suited for remote-excitation TERS as an easy alternative to the grating-assisted nanofocusing technique.

3.2 Fabrication of the Remote-Exited TERS probe

I found that the synthesis of AgNWs that have ultra-sharp conical tips with nanometer-scale tip curvature, and their integration with commercial AFM probes for topographical imaging[20]. In this chapter, we demonstrate that high-resolution remote-excitation TERS imaging can also be realized with an AFM mounted sharp-tip AgNW. This RE-TERS probe utilizes colloidal silver nanocubes (AgNCs) attached to the AgNW probe to couple visible light into SPPs on the latter[27]. Benefiting from the low plasmonic loss of the free-standing AgNW at the visible wavelengths[21], the propagation loss of SPPs along the NW can be maintained at less than 1 dB when the AgNC is placed only a few microns away from the tip apex. The conical taper at the AgNW tip leads to the further compression of SPPs modes and the generation of a plasmonic hot spot at the tip apex to allow high spatial resolution TERS imaging. Adding to the inherent low background noise of the remote-excitation scheme, the AgNC antenna is insensitive to the polarization of the incident light, which allows the use of linearly polarized light with the electric field parallel to the metallic substrate to further reduce the background Raman noise from stray beams. With the AgNC-AgNW RE-TERS probe, we demonstrated the TERS imaging of monolayer molybdenum disulfide (MoS_2) domains and estimated the spatial resolution around 41 nm and TERS

contrast around 100. The spatial resolution can be further pushed to ~10 nm when a single-walled carbon nanotube (SW-CNT) sample is characterized.

As illustrated in **Figure 3.1 a**, the RE-TERS probe was installed on a commercial AFM-TERS system (SmartSPM^{TM} 1000, AIST-NT) with modifications to enable polarization adjustment of the incident laser. To launch the SPPs into the AFM-mounted AgNW probe, a linearly polarized laser (532nm, *s*-polarization) was focused on the AgNC attached to the side wall of a NW at an incident angle of ~ 25° by a microscope objective (100×) with a numerical aperture (NA) of 0.7 and a long working distance of 6 mm. The excited SPPs propagate along the NW and get further compressed by the conical geometry of the NW tip to generate a nano-sized hot spot at the tip apex for TERS excitation. The TERS signal scattered by the AgNW tip is then collected through the same objective lens. To maintain the remote-excitation condition, the NC needs to be at least several micrometers away from the NW tip (**Figure 3.1 b**), so that the tip sits well outside the laser focus (~1 μm × 0.9 μm). By raising the laser focus away from the sample and choosing the s-polarization for excitation, the background noise from direct illumination of the sample is minimized.

AgNCs used here were prepared according to a previously reported polyol synthesis method with slight modification[28]. These AgNCs display high size monodispersity[29] and have an edge length of ~ 200 nm (**Figure 3.1 c**). Sharp-tip AgNWs were synthesized following our previously reported method[20]. The crystalline AgNW has smooth surfaces that minimize the propagation loss to ~0.4 dB/μm[21] for the 200nm-in-diameter AgNW used in **Figure 3.1 b**. Given an average of ~3μm distance between the AgNC and the AgNW

tip, the propagation loss of the SPPs was around 1.2 dB. The conical tip tapered to an ultra-sharp apex (tip radius ~15 nm, **Figure 3.1 d**). The AgNC-AgNW bundle was fabricated by incubating a mixture of AgNW and AgNC colloidal solutions for 12 hrs, during which AgNCs self-assembled on the AgNW surface and the density was adjusted by their relative concentrations (details in Supporting Information). The mixture was then drop-casted on a polydimethylsiloxane (PDMS) substrate, from which a single AgNC-AgNW bundle was picked up with a tungsten tip mounted on a micromanipulator. Any excess AgNCs were removed by gently wiping the AgNW with the tungsten tip before picking it up. Then, the AgNC-AgNW bundle with a single AgNC was assembled to the sidewall of the pyramidal tip of a conventional silicon AFM cantilever (Olympus, Model# AC160TS-R3), as shown in **Figure 3.1 b**. This procedure has been demonstrated in our previous report as a simple yet effective fabrication method to prepare high-resolution, high aspect-ratio AFM probes with good stability and performance[20]. The adhesion between a clean AgNW and the silicon tip is sufficient for both AFM tapping mode and contact mode operations. As shown in **Figure 3.1 e**, when a laser beam is tightly focused on the AgNC (marked by the red arrow), the light coupled out from the AgNW tip 6μm away from the laser appears clearly as a bright spot (marked by the yellow arrow), demonstrating the successful launching of AgNW SPPs and their propagation to the tip apex. It is worth noting that both the colloidal AgNCs and sharp-tip AgNWs are synthesized in milliliter to liter volumes and the probe fabrication process can be completed under an optical microscope without the need for cost-consuming equipment such as focused ion beam (FIB) etching.

Here I provides some details of the fabrication method of the sharp-tip AgNWs, different size of AgNCs, assemble of the AgNW-AgNC RE-TERS bundle and the qualities of the bundle control method.

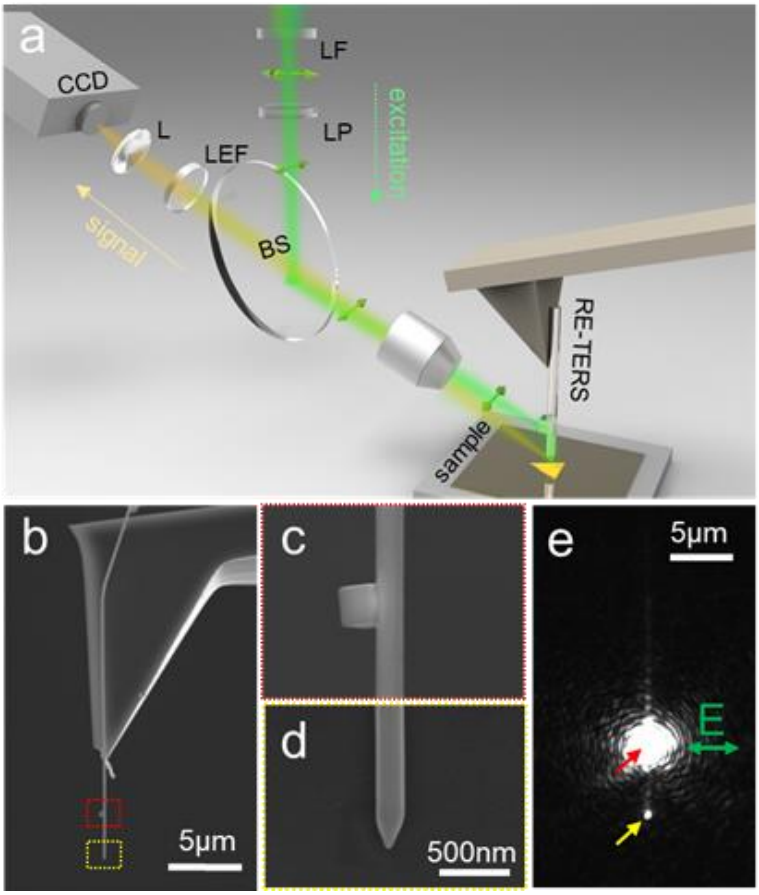

Figure 3.1 Remote-excitation tip-enhanced Raman spectroscopy (RE-TERS). **a,** Schematic illustration of the RE-TERS setup. The green excitation laser beam (532 nm) is sent through a laser line filter (LF), a linear polarizer (LP) and a beam splitter (BS) to an objective lens, which focuses it on an AgNC to excite SPPs on the AgNW waveguide. The SPPs propagate toward the tapered tip to excite TERS signals, which are collected through the same objective lens, filtered by a long-pass edge filter (LEF) and collected by a CCD spectrometer. **b,** SEM image of a RE-TERS probe. **c** and **d,** Close-up SEM images of the AgNC-AgNW junction **c** and sharp AgNW tip **d**. **e,** An image obtained in bright field optical microscopy showing the coupling between the 532nm excitation laser beam (polarization along the green arrow) and the AgNC-AgNW junction coupler (red arrow). The yellow arrow marks the position of the AgNW tip.

3.2.1 The size control of AgNCs

Nanoparticle sizes were controlled by varying the reaction time while maintaining concentrations and feeding rates of $AgNO_3$ and PVP constant throughout the synthesis process. Increased reaction time led to more solution above silicone oil bath causing temperature gradient, which gave a slightly larger size distribution as a result. However, in our nanoparticle synthesis, we were able to control the size distribution within 20 nm even with the largest nanoparticles synthesized. By accounting number of 200~300 AgNCs for each size in SEM image, the dimension distribution of different size AgNCs could be provided as shown in **Figure 3.2**. The size of ~180nm AgNC is the best for the RE-TERS probe fabrication.

3.2.2 The diameter distribution of sharp-tip AgNWs

The diameter of the sharp-tip AgNWs can be controlled as well. **Figure 3.3 a** shows the dimension distribution of ~200nm diameter AgNW. We were able to control the size distribution within 60 nm. The SEM image (**Figure 3.3 a and b**) shows the productivity and quality of the sharp-tip AgNWs.

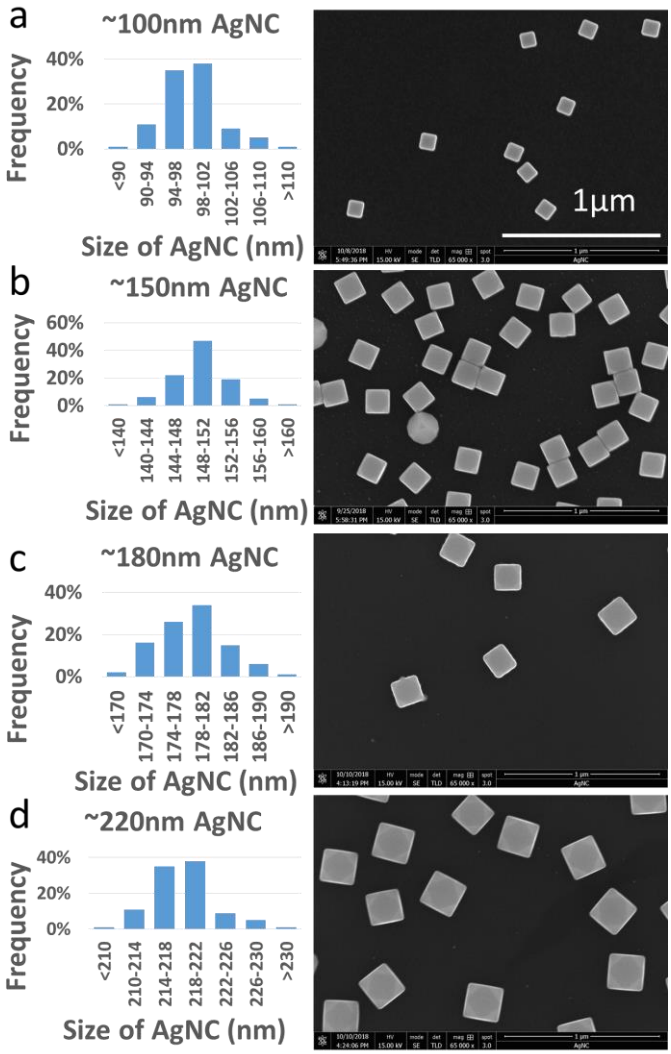

Figure 3.2 The dimension distribution and SEM images (same scale bar of 1 µm) of different size AgNCs. **a,** the 100nm AgNC, **b,** the 180nm AgNCs, **c,** the 150nm AgNCs and **d,** the 220nm AgNCs.

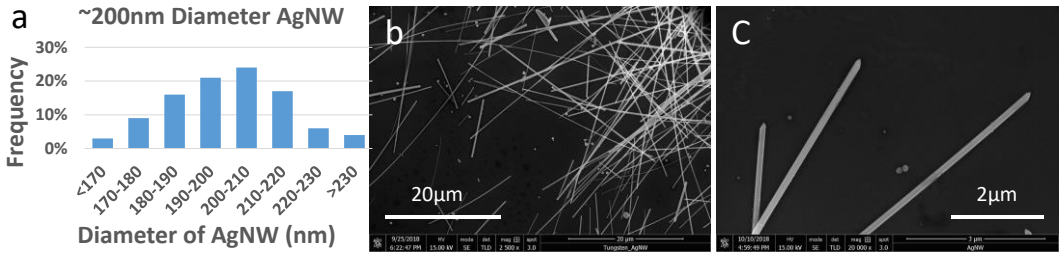

Figure 3.3 The diameter distribution of AgNW. **a,** the distribution of diameter of sharp-tip AgNWs. **b** and **c,** SEM images of the sharp-tip AgNWs.

3.2.3 AgNC-AgNW bundle synthesis and probe preparation

The AgNW solution (concentration ~10^8/mL, solved in ethanol) and AgNC solution (concentration ~10^{11}/mL, solved in ethanol) were mixed and then incubated for 48hrs at room temperature to form AgNC-AgNW bundles. After incubation, the top clean solution was removed and the bottom solution containing bundles was casted on a PDMS substrate and dried with nitrogen. The averaged AgNC density on an AgNW can be controlled by varying the volume ratio of AgNW and AgNC solutions, as shown in **Figure 3.4**. The final AgNC density of ~0.7 μm^{-1} (on AgNW) was used in this experiment, which gave the highest chance to find a single AgNC around 2~6μm away from the AgNW tip. The bundle samples on PDMS substrate were then examined under a dark-field optical microscope (Nikon Eclipse Ni-U, 50× objective lens)[30, 31] and a sCMOS camera (Zyla 5.5, Andor). With proper contrast settings in the camera, the AgNCs can be identified from the AgNW. A sharp tungsten probe controlled by a high-precision motorized micromanipulator (Sutter Instrument Co.) was then used to gently wipe along the selected AgNW to remove the unnecessary AgNCs from the AgNW, then pick it up and mount onto the side wall of a conventional silicon AFM cantilever (Olympus, Model# AC160TS-R3). The prepared probe was usually used within three days of fabrication to avoid oxidization.

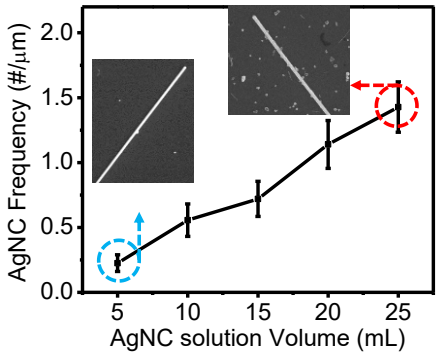

Figure 3.4 Frequency of AgNCs attached on AgNW. Inset **a** and **b,** are SEM images of AgNC-AgNW bundles with low and high AgNC densities.

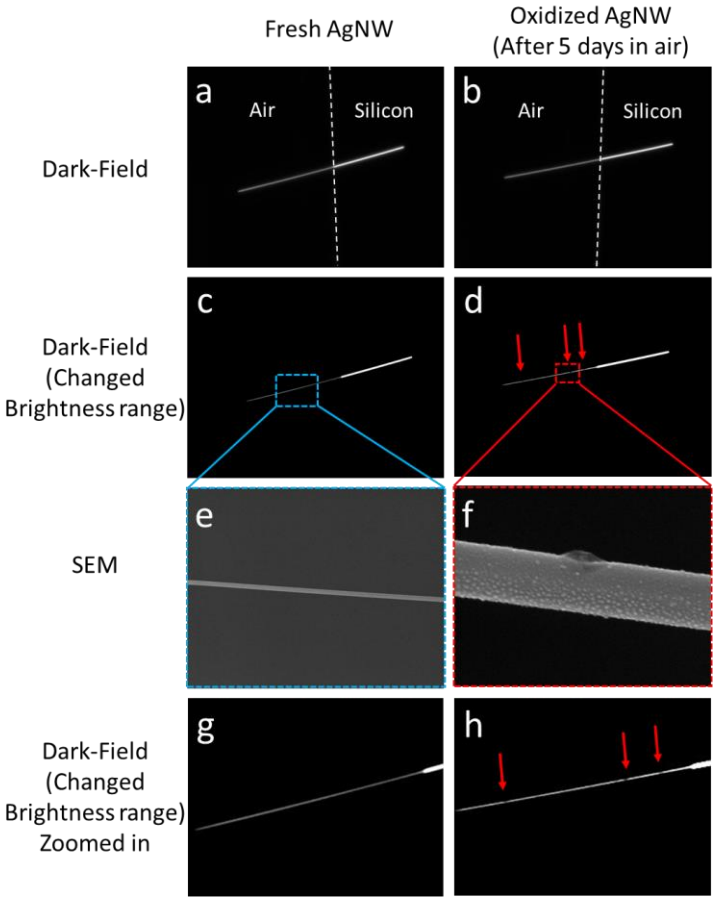

Figure 3.5 Dark-field image of a fresh AgNW at the edge of the silicon wafer. **a,** when it was fresh and **b,** after 5 days. **c** and **d,** are the images with changed brightness range corresponding to **a** and **b**, respectively, **e** and **f,** the SEM image for zoomed-in details, **g** and **h,** the zoomed-in dark-field image of **c** and **d**.

3.2.4 AgNC-AgNW bundle synthesis and probe preparation

Dark-field microscopy provides a way enabling higher contrast image [30, 31]. Combining with a 16bits CCD camera (16 bit, Zyla 5.5, Andor), the dark-field microscopy can examine the quality of the RE-TERS probe. **Figure 3.5 a** and **b** are the dark-field images with a full range of brightness. By changing the range of brightness, defects on AgNW could be seen clearly, as shown in **Figure 3.5 h**, the dark points noted by red arrows. We put fresh AgNW at the edge of a piece of a silicon wafer (**Figure 3.5 a**), there is no obvious dark point by changing the range of brightness and the input light power. After exposing in the air for 5 days, AgNW would be oxidized and generate lots of roughness on the surface. The dark points in the changed brightness range dark-field image are the oxidation points, which has been confirmed by the SEM (**Figure 3.5 f**).

3.2.5 Removing excessive AgNCs from a AgNW

Since only the closest AgNC to the AgNW tip is used as the coupler, the rest of AgNCs are not needed in the probe. On the other hand, these excessive AgNCs can potentially reduce both the adhesion force and the friction force between the AgNW and the cantilever, making the probe more vulnerable during scanning. Therefore, removing the unneeded AgNCs from the bundle is necessary. Benefiting from the weak adhesion between AgNC and AgNW, they can be easily removed by simply wiping a tungsten tip along the nanowire. **Figure 3.6** shows the process. The AgNC-AgNW bundle is mounted on the edge of a PDMS substrate here for better optical image quality. Examined under dark-field optical

microscopy with proper contrast parameters used in the CCD camera, the AgNCs can be located on the AgNW. A sharp-tip tungsten probe mounted on a motorized micro-manipulator was used to remove the AgNCs (**Figure 3.6 b**).

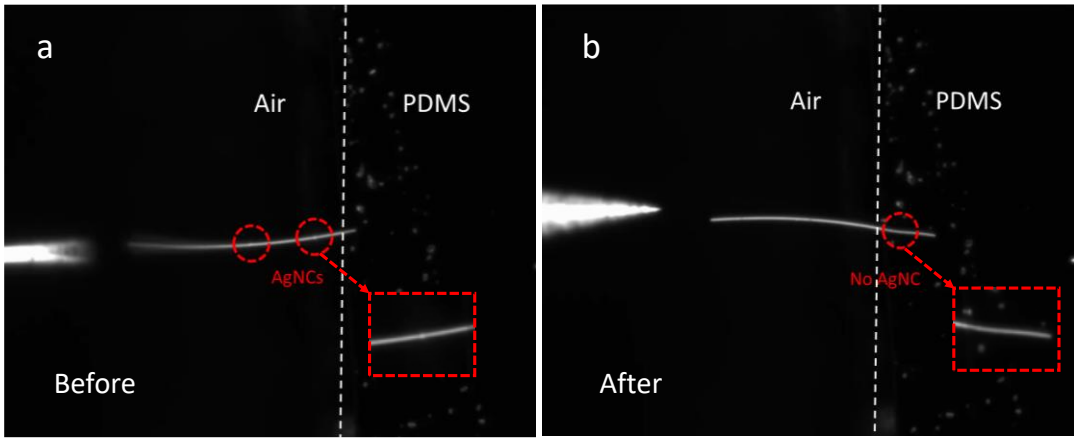

Figure 3.6 Removal of the extra AgNC**. a** and **b,** show before and after AgNCs wiped off by the tungsten probe.

3.3 Simulations and calculations of the Remote-Exited TERS probe

The coupling efficiency from the far-field excitation to the AgNW SPP modes has strong dependence on the coupling conditions, including the size of the AgNC and the wavelength, polarization and coupling angle of the incident laser[32]. Finite element analysis (FEA) simulations using commercial software (COMSOL Multiphysics 5.1) was implemented to study the influence of the afore mentioned effects to optimize the coupling efficiency, which is defined as the ratio between the electromagnetic energy flux propagating along the AgNW and the power of incident beam.

3.3.1 COMSOL simulation for the coupling efficiency of the Remote-Exited TERS probe

Figure 3.7 illustrates the parameters used in the simulation. The incident angle (θ) of 65° with respect to the AgNW is pre-defined by the equipment, and therefore kept constant in the simulation. The azimuth angle ϕ is defined as the angle between the normal direction of the AgNW sidewall that is attached to the AgNC and the projection of the polarized Gaussian beam (beam waist = 1 μm) incidence direction. Because the AgNW has a pentagonal cross-section, its sidewalls are flat [11] facets and allow the AgNC to sit with one face in complete parallel with one of its sidewalls. As shown in **Figure 3.7 b**, the *s*-polarization excitation (electric field perpendicular to the AgNW axis) generally gives higher coupling efficiency than the *p*-polarization, in particular near 532nm wavelength, which benefits from the strong plasmonic enhancement of AgNWs in response to the *s*-polarization[25, 33]. For 532nm excitation (**Figure 3.7 c**), the optimized AgNC size around 200nm gives coupling efficiency near 4%, which is about 4 times higher than that of *p*-polarization. The azimuthal angle dependence study in **Figure 3.7 d** reveals that the coupling efficiency varies between 2~4% when the incident light is focused on the AgNW-AgNC junction from different directions (ϕ), providing a robust fabrication tolerance when attaching the bundle to the AFM cantilever.

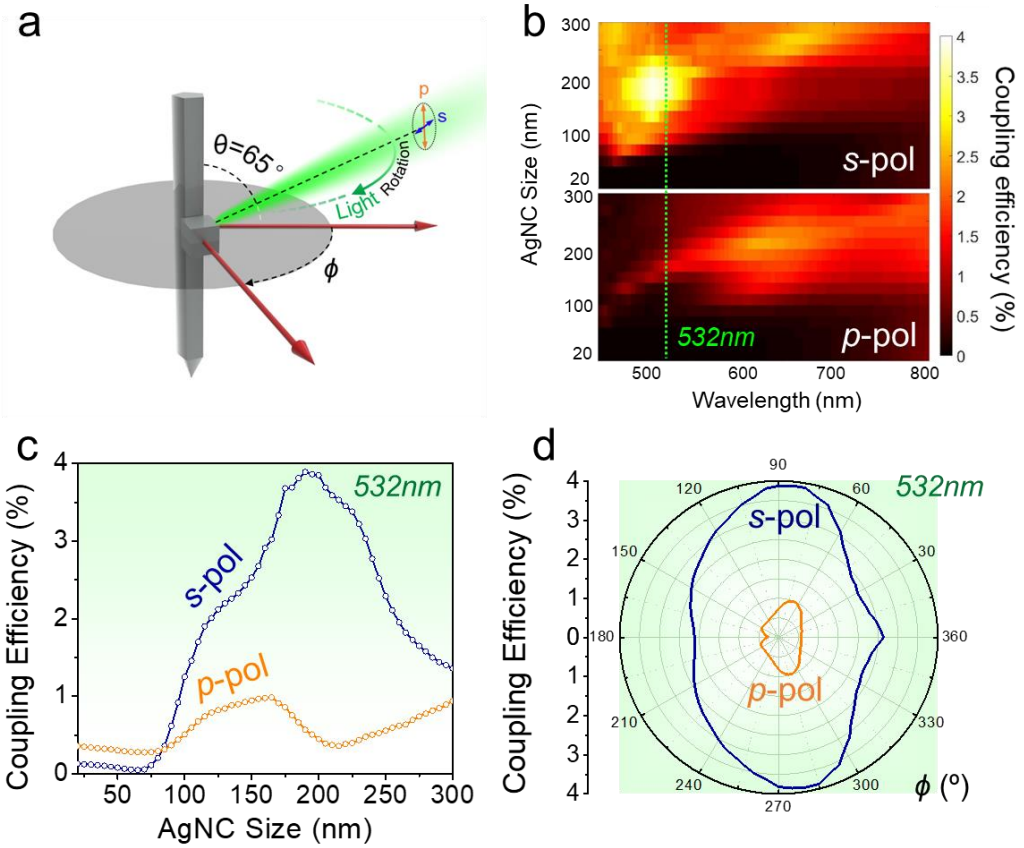

Figure 3.7 Optimization of the RE-TERS coupling efficiency. **a,** Schematic diagram showing the parameters used to optimize in numerical simulations. The laser beam maintains a 65° incident angle with respect to the AgNW, as restricted by the equipment, while it can rotate around the AgNW (green arrow) and change the coupling angle (ϕ). The orientation of the *s*- and *p*-polarizations are marked by the navy blue and orange arrows. **b,** Numerical simulations showing the coupling efficiency (%) as functions of incident light wavelength (450 ~ 800 nm) and AgNC size (20 ~ 300 nm) for both *s*- (top) and *p*- (bottom) polarizations. The green dashed line marks the laser wavelength (532 nm) used in the experiments, with the profiles shown in **c**. **d,** Coupling efficiency dependence on the coupling angle (ϕ) for both polarizations.

3.3.2 TERS enhancement factor and the signal-noise ratio (contrast) calculation for the Remote-Exited TERS probe

The chemical sensitivity of a TERS probe in the direct-excitation configuration is typically characterized by the enhancement factor (*EF*), as given by the following equation:

$$EF = \left(\frac{I_{engaged} - I_{retracted}}{I_{retracted}}\right)\frac{A_{background}}{A_{TERS}} \quad \textbf{eq. 3.1}$$

where $I_{engaged}$ and $I_{retracted}$ are Raman peak intensities measured with the tip in contact and retracte, $A_{background}$ is the area of the excitation laser spot, and A_{TERS} is the effective area of the TERS enhancement region, giving that the molecular density is a constant during the measurement. The difference between $I_{engaged}$ and $I_{retracted}$ is the Raman signal generated due to the tip enhancement, or $I_{TERS} = I_{engaged} - I_{retracted}$. It can be seen from this equation that molecules under the direct laser excitation will contribute to $I_{retracted}$, but only those under the nano-sized TERS spot, which depends on the tip radius and tip-substrate distance, will contribute to the TERS signal (I_{TERS}) that has nanoscale spatial resolution. Therefore, most of the molecules within the excitation laser spot become part of the background which limits both the TERS sensitivity and the spatial resolution. In remote excitation configuration, however, this diffraction-limited background is suppressed, because the laser focus is vertically separated from the scanning region, and the far-field radiation density reaching the detection spot is therefore reduced. This has been observed in other remote-excitation configurations, including grating couplers[34]. Apart from background suppression, the RE-TERS can also produce stronger signal compared to the conventional direct-excitation (DE) configuration under the same incident power. Although not yet experimentally demonstrated, the signal enhancement is theoretically possible when the

power of optical excitation injected into the near-field region through the SPPs outweighs the antenna effect of the tip in DE-TERS, with the apex capturing light over a cross-section exceeding its geometric dimensions. Nevertheless, this requires efficient optical coupling and low propagation loss of the RE-TERS configuration, which has been challenging to achieve.

In order to calculate the EF of the remote-excited TERS probe can produce and make a comparison between the RE-TERS probe and conventional scattering TERS probe, the commercial finite element analysis (COMSOL Multiphysics) has been carried out and the results are shown in **Figure 3.8**. The electrical field (the z component) distribution in three configurations, sharp-tip AgNW (5nm diameter the apex) with and without metal substrate and regular tip AgNW (50nm diameter the apex) with the silver substrate, has been analyzed. The s- and p- polarization excited light with 532nm wavelength were focused on the AgNW-AgNC junction, excited SPPs ($\overrightarrow{k_{sp}}$) in the AgNW and propagated towards its tapered tip, where they were further compressed at the 1nm gap (in the with gap configurations) or re-excited light (in the without gap configuration). **Figure 3.8 a** shows that the largest E-field intensity has been achieved in the sharp-tip AgNW with metal substrate configuration and s- polarization exited light compared with the other configurations and polarization, which results in the large $|E_Z|^2 / |E_0|^2$ ($\sim 1.4\times10^5$) and implies greatly enhanced Raman signal.

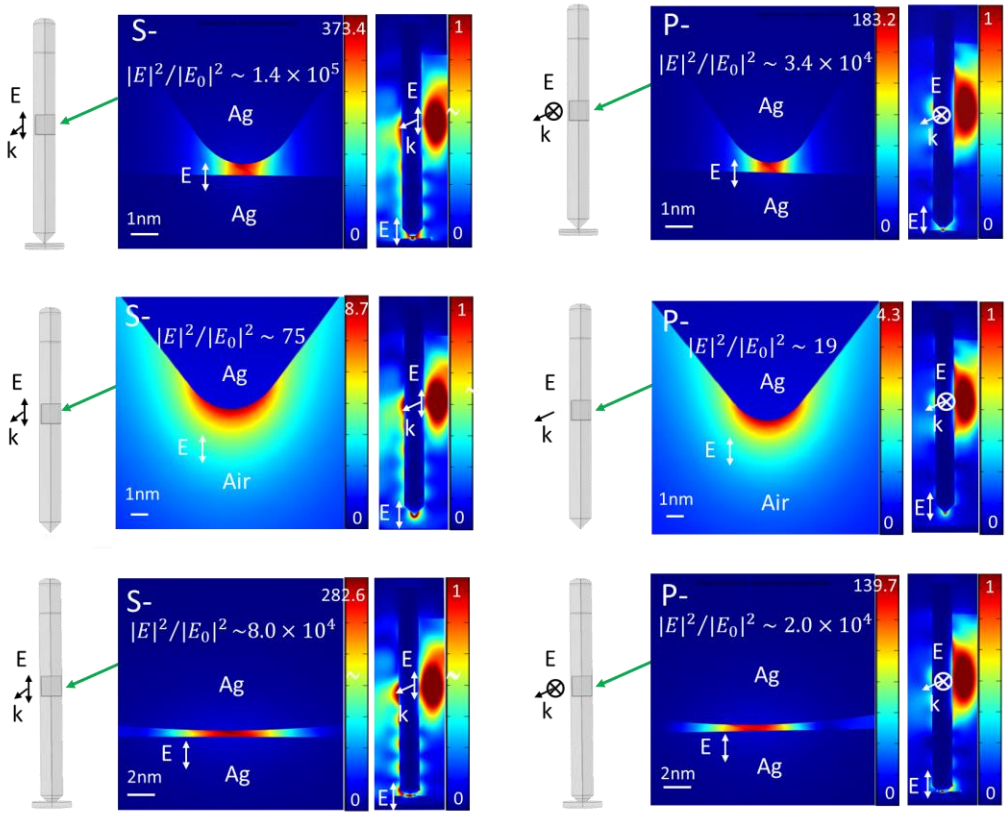

Figure 3.8 Electric field (the z component) distribution at the apex of an AgNW with the coupled 532nm laser by the AgNW-AgNC coupler, the exited light propagating along the direction labeled by the green arrow. **a** s- **b** p- polarization excited, respectively. Electrical field distribution in the gap between sharp-tip AgNW with 5nm diameter tip and surface of silver sample, **c** and **d** at the apex of a sharp-tip AgNW with 5nm diameter, **e** and **f** in the gap between regular tip AgNW with 50nm diameter tip and surface of silver sample. The gaps are 1nm.

3.4 Performance of the Remote-Excited TERS probe demonstration by measuring the 4-ATP self-assemble monolayer (SAM)

The self-assemble monolayers (SAMs) are the good candidate for demonstrating the TERS performance, because of their nanometer scale thickness providing small gap between the probe tip and the supported metal surface (Ag, for example). The self-assemble monolayer (SAMs) of 4-ATP on Ag film was prepared by incubating the Ag films (on Si substrate) in

20mL 4-ATP solution (1mM) for 24 hours. After incubation, the Ag substrate was rinsed with pure ethanol multiple times to remove the excessive 4-ATP molecules.

In the comparative characterization of the RE- and DE-TERS shown in **Figure 3.9**, we demonstrated that the AgNC-AgNW based RE-TERS probe can provide the benefit of both background suppression and signal enhancement, thus significantly improve the TERS contrast. **Figure 3.9 a-b** illustrate the RE- and DE-TERS measurement configuration. The same probe and laser power (6mW) were used for all the measurements in **Figure 3.9**. In the RE-TERS experiment, the incident laser is focused on the AgNC, whereas in DE-TERS, the laser is focused directly on the AgNW tip. To ensure substrate and sample homogeneity, we used a self-assemble monolayer (SAM) of 4-aminothiophenol (4-ATP) on an ultra-smooth Ag thin film as the standard sample. The ultra-smooth Ag thin film was fabricated following the protocol and will be illustrated in next chapter. With both s- and p-polarized incident light, the background ($I_{retracted}$) is significantly reduced in RE-TERS, with a background reduction ratio ($I_{retracted,RE}/I_{retracted,DE}$) of 0.26 and 0.52, respectively. Similarly, for both polarizations, enhancement of the TERS signal in RE opposed to DE excitation were observed, featuring a signal enhancement ratio ($I_{engaged,RE}/I_{engaged,DE}$) of 12.2 (*s*-pol) and 3.3 (*p*-pol). Both calculations are based on the Gaussian fitting of the 1446cm^{-1} peak. The signal enhancement from more efficient power injection than tip-scattering and the background reduction from the separation of the excitation and detection spots work synergistically to significantly increase the TERS contrast. Compared to the EF, the calculation of which is often based on many estimations, the TERS contrast, given by $C =$

$\frac{I_{engaged}}{I_{retracted}}$[35-37], is based purely on experimental data and is a direct measure of the signal increase by the tip and the image quality that can be obtained in a TERS experiment[38]. Therefore, *C* is of more practical relevant and has been adopted as the industrial standard for benchmarking the performance of TERS probe. Here, we have seen a $C_{RE\text{-}TERS}$ ~ 100 for the *s*-polarization, which is enhanced from that of the same probe in the DE-TERS configuration by ~47-fold. Even for the *p*-polarization that is not optimized for RE-TERS coupling, we still saw a 6-fold increase in TERS contrast with a $C_{RE\text{-}TERS}$ ~ 20.

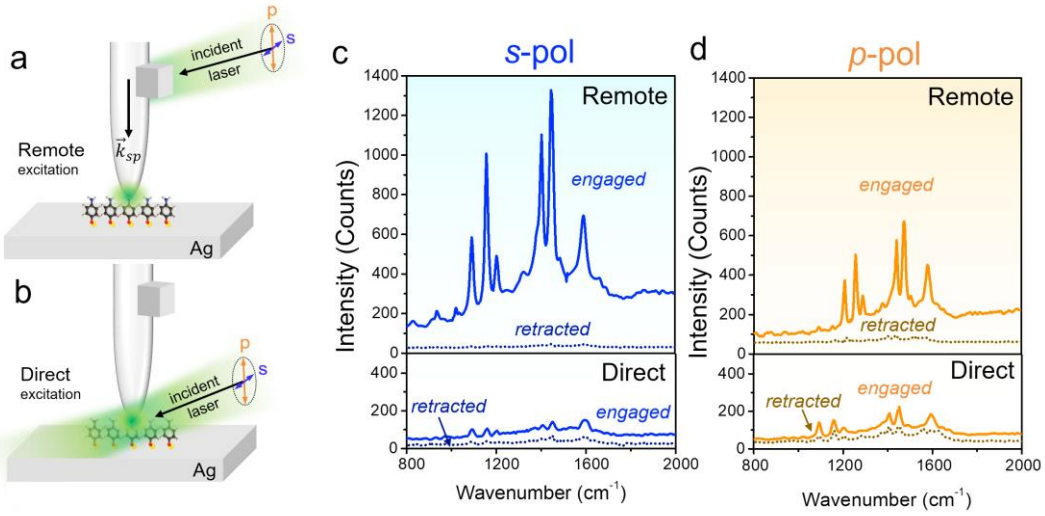

Figure 3.9 Comparison between RE-TERS with DE-TERS. **a** and **b,** Schematics showing the remote **a** and direct **b** excitation methods. In both cases, *s*- and *p*- polarizations were examined on a self-assembled monolayer (SAM) of 4-ATP on an ultra-smooth Ag substrate. **c** and **d,** 4-ATP Raman spectra measured with RE- and DE-TERS with incident lasers with *s*- **c** and *p*- **d** polarizations in both engaged (light color, solid lines) and retracted (dark color, dashed lines) modes. Excitation: 532nm, 6 mW. Integration time=2s.

Figure 3.11 shows RE-TERS spectra as a function of tip-substrate distance (*d*) for 4-ATP SAM on ultra-smooth Ag thin film using an incident laser power of 6 mW at λ=532 nm. The tip was first brought in contact with the substrate (define as 0 nm), then the tip was gradually lifted by adjusting the set point in the feedback system of the contact mode AFM.

Figure. 3.10 shows the relationship between contact mode AFM set-point and the tip-to-substrate distance. The variable range of the set point was 1.63×10^3 to 1.75×10^3. By choosing different set point value from this range, the corresponding tip-to-substrate distance between 0 to 6nm could be achieved. The TERS signal dropped drastically when the gap distance increased beyond 2 nm and barely showed any Raman signature of 4-ATP at 6 nm, clearly demonstrating the near-field origin of the signal. We also note that although positions of the major Raman peaks stay constant at different gap distance, the relative peak intensity changed noticeably. At larger tip-substrate distances (>2nm), the 1089 cm^{-1} peak corresponding to C-S stretching (v(CS), 7a) and the 1593 cm^{-1} peak corresponding to C=C stretching (v(CC), 8a) are the dominating peaks[39], as marked by the purple arrows in **Figure 3.11**. Both vibrations belong to a_1 symmetry of the 4-ATP, which has a C_{2v} symmetry point group. This is consistent with the surface selection rule, which dictates that for an adsorbed molecule with C_{2v} symmetry and its C_2 axis perpendicular to the metal surface, the electromagnetic enhancement should obey the relationship of $a_1>b_2, b_1>a_2$[39-41]. However, for small tip-substrate distances (≤2 nm), the vibrations with b_2 symmetry at 1156 cm^{-1} (δ(CH), 9b) and the 1450 cm^{-1} (v(CC)+ δ(CH), 19b) quickly grow stronger than the a_1 peaks. Such strong anomaly has been previously observed in systems with tight optical confinement, such as hollow plasmonic nanoparticles[42] or nanogaps[43, 44], and can be attributed to the chemical enhancement effects, such as photo-induced charge transfer through the Herzberg−Teller contribution[39, 43, 45, 46]. **Figure 3.11** clearly demonstrates the dependence of the "b_2 enhancement" on the gap size or the degree of confinement.

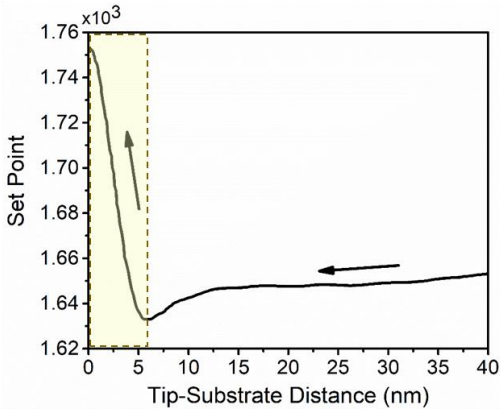

Figure 3.10 The relationship between the contact-mode AFM set point and the tip-substrate distance. The tip-to-substrate distance can be controlled by varying the set point.

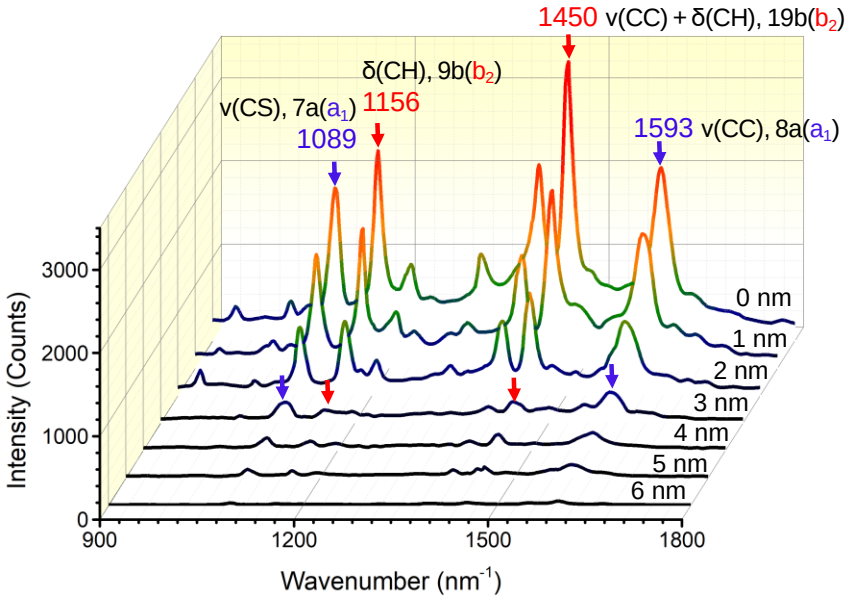

Figure 3.11 Dependence of RE-TERS signals on tip-to-substrate distance. As tip gets closer to the 4-ATP SAM sample, the overall signal increases drastically. At large tip-substrate distances, the peaks marked by blue arrows (1089 cm^{-1} and 1593 cm^{-1}) have the highest intensities, consistent with regular SERS spectrum, whereas at smaller distances, the peaks marked by the red arrows (1156cm^{-1} and 1450 cm^{-1}) become dominating.

3.5 Probe reproductively: TERS performance examination

We characterized five RE-TERS probes to examine the Raman enhancement performance variation. The TERS measurements were carried out on a self-assembled monolayer of 4-ATP on a silver substrate (532 nm excitation, 0.2mW at sample surface, accumulation time was 2 second). **Figure 3.12** shows a representative Raman spectrum, and a list of prepared probes including their TERS performance. It is noticeable that the probe quality is relatively consistent. Taking the highest peak at 1450 cm^{-1} for example, the standard derivation (std) of the peak intensities are 200 counts (cts.), which is about 15% of the averaged intensity (~1365 cts.). Consequently, we conclude that the probe fabrication technique is reproducible.

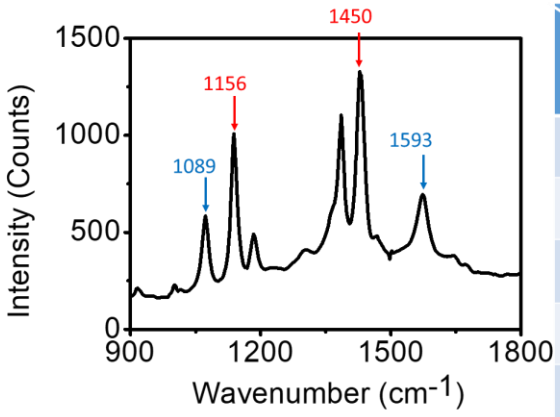

Peak(cm^{-1}) / Probe Number	1089 (cts.)	1156 (cts.)	1450 (cts.)	1593 (cts.)
Probe 1	584.3	1007.6	1327.8	694.2
Probe 2	719.0	1143.8	1679.2	841.8
Probe 3	673.3	1025.1	1427.3	779.4
Probe 4	524.5	895.2	1235.4	594.8
Probe 5	471.0	832.6	1159.2	536.7

Figure 3.12 The intensity data of 4-ATP Raman peak from different RE-TERS probes.

3.6 Conclusions

In summary, using AgNCs with proper size as an efficient plasmonic antenna to convert the excitation laser beam into the surface plasmon polaritons on a sharp-tip AgNW

waveguide. The RE-TERS probes can be fabricated through a facile, robust and reproducible method, which requires only economical benchtop techniques. This polarization-insensitive antenna design allows the choosing of laser polarization that has weak interaction with the sample substrate for the further reduction of background noise. We expect that the remote-excitation plasmonic probe offers new routes for applications in disciplines where high resolution and sensitivities are needed, for example, in near-field scanning optical imaging and sensing.

3.7 References

1. Stockle, R. M.; Suh, Y. D.; Deckert, V.; Zenobi, R. *Chem Phys Lett* **2000,** 318, (1-3), 131-136.

2. Hayazawa, N.; Inouye, Y.; Sekkat, Z.; Kawata, S. *Opt Commun* **2000,** 183, (1-4), 333-336.

3. Anderson, M. S. *Appl Phys Lett* **2000,** 76, (21), 3130-3132.

4. Pettinger, B.; Picardi, G.; Schuster, R.; Ertl, G. *Electrochemistry* **2000,** 68, (12), 942-949.

5. Zrimsek, A. B.; Chiang, N.; Mattei, M.; Zaleski, S.; McAnally, M. O.; Chapman, C. T.; Henry, A.-I.; Schatz, G. C.; Van Duyne, R. P. *Chemical reviews* **2016,** 117, (11), 7583-7613.

6. Richard-Lacroix, M.; Zhang, Y.; Dong, Z.; Deckert, V. *Chemical Society Reviews* **2017,** 46, (13), 3922-3944.

7. Li, Z. Y. *Advanced Optical Materials* **2018,** 6, (16), 1701097.

8. Chiang, N.; Chen, X.; Goubert, G.; Chulhai, D. V.; Chen, X.; Pozzi, E. A.; Jiang, N.; Hersam, M. C.; Seideman, T.; Jensen, L. *Nano letters* **2016,** 16, (12), 7774-7778.

9. Zhang, R.; Zhang, Y.; Dong, Z. C.; Jiang, S.; Zhang, C.; Chen, L. G.; Zhang, L.; Liao, Y.; Aizpurua, J.; Luo, Y.; Yang, J. L.; Hou, J. G. *Nature* **2013,** 498, (7452), 82-86.

10. Ropers, C.; Neacsu, C. C.; Elsaesser, T.; Albrecht, M.; Raschke, M. B.; Lienau, C. *Nano Letters* **2007,** 7, (9), 2784-2788.

11. De Angelis, F.; Das, G.; Candeloro, P.; Patrini, M.; Galli, M.; Bek, A.; Lazzarino, M.; Maksymov, I.; Liberale, C.; Andreani, L. C.; Di Fabrizio, E. *Nat Nanotechnol* **2010,** 5, (1), 67-72.

12. Berweger, S.; Atkin, J. M.; Olmon, R. L.; Raschke, M. B. *J Phys Chem Lett* **2010,** 1, (24), 3427-3432.

13. Yu, J.; Saito, Y.; Ichimura, T.; Kawata, S.; Verma, P. *Appl Phys Lett* **2013,** 102, (12), 123110.

14. Wang, Y.; Srituravanich, W.; Sun, C.; Zhang, X. *Nano Letters* **2008,** 8, (9), 3041-3045.

15. Kravtsov, V.; Ulbricht, R.; Atkin, J.; Raschke, M. B. *Nat Nanotechnol* **2016,** 11, (5), 459.

16. Schambach, P., *Tip-enhanced Raman spectroscopy in ultra-high vacuum*. 2013.

17. Yasuhiko, F.; Peter, W.; Steven De, F.; Hiroshi, U.-i. *Japanese Journal of Applied Physics* **2016,** 55, (8S1), 08NA02.

18. Russell, K. J.; Liu, T.-L.; Cui, S.; Hu, E. L. *Nature Photonics* **2012,** 6, 459.

19. Tao, A.; Kim, F.; Hess, C.; Goldberger, J.; He, R.; Sun, Y.; Xia, Y.; Yang, P. *Nano Letters* **2003,** 3, (9), 1229-1233.

20. Ma, X. Z.; Zhu, Y. Z.; Kim, S.; Liu, Q. S.; Byrley, P.; Wei, Y.; Zhang, J.; Jiang, K. L.; Fan, S. S.; Yan, R. X.; Liu, M. *Nano Letters* **2016,** 16, (11), 6896-6902.

21. Kim, S.; Bailey, S.; Liu, M.; Yan, R. X. *Nano Res* **2017,** 10, (7), 2395-2404.

22. Ditlbacher, H.; Hohenau, A.; Wagner, D.; Kreibig, U.; Rogers, M.; Hofer, F.; Aussenegg, F. R.; Krenn, J. R. *Physical Review Letters* **2005,** 95, (25), 257403.

23. Yan, R.; Pausauskie, P.; Huang, J.; Yang, P. *Proceedings of the National Academy of Sciences of the United States of America* **2009,** 106, (50), 21045-21050.

24. Wang, W.; Yang, Q.; Fan, F.; Xu, H.; Wang, Z. L. *Nano Letters* **2011,** 11, (4), 1603-1608.

25. Knight, M. W.; Grady, N. K.; Bardhan, R.; Hao, F.; Nordlander, P.; Halas, N. J. *Nano Letters* **2007,** 7, (8), 2346-2350.

26. Sanders, A. W.; Routenberg, D. A.; Wiley, B. J.; Xia, Y.; Dufresne, E. R.; Reed, M. A. *Nano Letters* **2006,** 6, (8), 1822-1826.

27. Ma, X.; Zhu, Y.; Yu, N.; Kim, S.; Liu, Q.; Apontti, L.; Xu, D.; Yan, R.; Liu, M. *Nano Letters* **2018,** 19, (1), 100-107.

28. Tao, A.; Sinsermsuksakul, P.; Yang, P. *Nat Nanotechnol* **2007,** 2, 435.

29. Tao, A. R.; Huang, J.; Yang, P. *Accounts of Chemical Research* **2008,** 41, (12), 1662-1673.

30. Itoh, T.; Yamamoto, Y. S.; Kitahama, Y.; Balachandran, J. *Physical Review B* **2017,** 95, (11), 115441.

31. Itoh, T.; Yamamoto, Y. S.; Suzuki, T.; Kitahama, Y.; Ozaki, Y. *Applied Physics Letters* **2016,** 108, (2), 021604.

32. Wei, H.; Hao, F.; Huang, Y. Z.; Wang, W. Z.; Nordlander, P.; Xu, H. X. *Nano Letters* **2008,** 8, (8), 2497-2502.

33. Fang, Y. R.; Wei, H.; Hao, F.; Nordlander, P.; Xu, H. X. *Nano Letters* **2009,** 9, (5), 2049-2053.

34. Berweger, S.; Atkin, J. M.; Olmon, R. L.; Raschke, M. B. *The Journal of Physical Chemistry Letters* **2010,** 1, (24), 3427-3432.

35. Stöckle, R. M.; Suh, Y. D.; Deckert, V.; Zenobi, R. *Chem Phys Lett* **2000,** 318, (1), 131-136.

36. Pettinger, B.; Ren, B.; Picardi, G.; Schuster, R.; Ertl, G. *Physical Review Letters* **2004,** 92, (9), 096101.

37. Christoph, M.; Sebastian, H.; Markus, J.; Sebastian, M.; Bernd, D.; Konrad, S.; Vasily, M. *Journal of Raman Spectroscopy* **2017,** 48, (1), 46-52.

38. Stadler, J.; Schmid, T.; Zenobi, R. *Nanoscale* **2012,** 4, (6), 1856-1870.

39. Osawa, M.; Matsuda, N.; Yoshii, K.; Uchida, I. *The Journal of Physical Chemistry* **1994,** 98, (48), 12702-12707.

40. Creighton, J. A. *Surface Science* **1986,** 173, (2), 665-672.

41. Zheng, J.; Zhou, Y.; Li, X.; Ji, Y.; Lu, T.; Gu, R. *Langmuir* **2003,** 19, (3), 632-636.

42. Wang, Y.; Chen, H.; Dong, S.; Wang, E. *The Journal of Chemical Physics* **2006,** 125, (4), 044710.

43. Qun, Z.; Xiaowei, L.; Qiang, F.; Xingxia, Z.; Junwei, Z. *Angewandte Chemie International Edition* **2006,** 45, (24), 3970-3973.

44. Fromm, D. P.; Sundaramurthy, A.; Kinkhabwala, A.; Schuck, P. J.; Kino, G. S.; Moerner, W. E. *The Journal of Chemical Physics* **2006,** 124, (6), 061101.

45. Cat, C.; L., B. R.; R., L. J. *ChemPhysChem* **2008,** 9, (11), 1617-1623.

46. Naoki, M.; Katsumasa, Y.; Ken-ichi, A.; Masatoshi, O.; Tomokazu, M.; Isamu, U. *Chemistry Letters* **1992,** 21, (7), 1385-1388.

Chapter 4 Sample preparation: Capillary-force-assisted clean-stamp transfer of two-dimensional materials

A simple and clean method to transfer two-dimensional (2D) materials plays a critical role in the fabrication of 2D electronics, in particular, the heterostructure devices based on the artificial vertical stacking of various 2D crystals. Currently, clean transfer techniques rely on sacrificial layers or bulky crystal flakes (e.g., hexagonal boron nitride) to pick-up the 2D materials. Here, we develop a capillary-force-assisted clean-stamp technique that uses a thin layer of evaporative liquid (e.g., water) as an instant glue to increase the adhesion energy between 2D crystals and polydimethylsiloxane (PDMS) for the pick-up step. After the liquid evaporates, the adhesion energy decreases, and the 2D crystal can be released. The thin liquid layer is condensed to the PDMS surface from its vapor phase, which ensures the low contamination level on the 2D materials and largely remains their chemical and electrical properties. Using this method, we prepared graphene-based transistors with low charge-neutral concentration (3×10^{10} cm^{-2}) and high carrier mobility (up to 48,820 cm^2 V^{-1} s^{-1} at room temperature), and heterostructure optoelectronics with high operation speed. Finally, a capillary force model is developed to explain the experiment.

4.1 Introduction

Two-dimensional (2D) materials, such as graphene and transition metal dichalcogenides (TMDs), have stimulated extensive research efforts in the fields of nano-electronics and optoelectronics due to their exceptional electrical and optical properties [1, 2]. By stacking different 2D material layers in van der Waals (vdW) heterostructures, new device concepts

with outstanding functionalities have been demonstrated [3-6]. Both the full exploration of 2D material properties and the fabrication of heterostructures require a clean and intact transfer technique, to move these layered materials from the preparation substrates onto target positions without compromising their properties or qualities, and in particular, without any contamination. So far, polymethyl methacrylate (PMMA) has been widely used as the holder for transferring, owing to the simple yet versatile procedure[7]. However, PMMA always leaves a thin layer of long-chain molecules on the 2D material surfaces, even after exhaustive rinse with various organic solvents [8]. This residual contaminates the sample surfaces and has become a major limiting factor restricting the device performance. To solve this problem, sacrificial layers, such as a thin metal[9, 10] or polylactic acid (PLLA) film[11], have been used to separate PMMA from the 2D materials. However, it introduces extra fabrication steps including deposition, dissolving, and washing, which are tedious in particular in the preparation of heterostructures. Polydimethylsiloxane (PDMS)-based stamp transfer method has been exploited as a dry-transfer technique for nano-electronics [12, 13]. So far, it cannot peel off 2D monolayers directly from silicon dioxide (SiO_2) substrate because the adhesion energy between PDMS and 2D monolayers (~7 mJ/m^2 for graphene)[14] is far weaker than the vdW energy between 2D materials and SiO_2 (~240 mJ/m^2 for graphene) [15]. To increase the bonding energy between the dry-transfer stamp and 2D monolayers, atomically flat surfaces of hexagonal boron nitride (h-BN) flakes have been recently introduced [16-18]. As a trade-off, removing this BN layer to expose the functional 2D materials is challenging.

In this chapter, it report a simple and universal capillary-force-assisted clean-stamp method to transfer 2D materials[19]. We demonstrate the flexibility and quality of this approach for single/multi- layer materials by the fabrication and characterization of a graphene-based field effect transistor (Gr-FET) and a vertically-stacked heterostructure photodetector. The key concept of this technique is the utilization of a thin liquid film between a PDMS stamp and 2D monolayers as a dynamic bonding enhancer. The thin liquid film acts as an instant glue between the PDMS stamp and 2D materials, and subsequently peels them off from the substrates. After the thin liquid layer evaporates, the capillary force vanishes and leaves the 2D monolayers ready to be released onto new substrates. The transient adhesion-enhancing mechanism bypasses the tradeoff between the peeling-off step and the releasing step, where the increase in adhesion fosters the peeling-off but hinders the releasing step[20]. Since this method uses a distilled volatile liquid film instead of a solid sacrificial layer, both physical damage and chemical contamination are minimized in this process. In addition, the 2D monolayers can be released to a target area on the receiving substrate by aligning the PDMS stamp under an optical microscope, since they can be located optically or with the help of a marker. Using this method, we fabricated a Gr-FET by the direct transfer of an exfoliated graphene monolayer onto palladium-gold electrodes, which demonstrated a near-zero charge-neutral voltage and a high electron mobility of ~48,820 $cm^2V^{-1}s^{-1}$ under room temperature, indicating an ultra-low surface doping and defect level incorporating from the transfer process. It is worth noting that this mobility level is the highest for graphene monolayers on SiO_2 surfaces, several times higher than those achieved by PMMA-based wet transfer with low-residue sacrificial layers, the previous best

performers on SiO_2[21]. We also demonstrate the versatility of this quick and clean transfer technique in the fabrication of high-performance 2D heterostructure devices and have achieved fast optical response with a graphene/MoS_2/graphene heterostructure photodetector. A capillary force model is discussed to reveal the role of liquid in this technique.

4.2 Transfer process

The capillary-force-assisted clean transfer process is illustrated in **Figure 4.1**. A thin PDMS film is first held over a beaker with boiling deionized (DI) water (or other solvents) for 3~5 seconds, to condense water on the PDMS surface. The PDMS is then quickly yet gently placed on the substrate with 2D monolayers, which are prepared by the mechanical exfoliation method and confirmed by Raman spectroscopy. After forming a conformal contact with the SiO2 substrate, the PDMS is quickly peeled off, starting from one side and maintaining a small angle between the PDMS and the substrate during the process. Firmly pulled by the capillary force, the 2D monolayers now adhere to the PDMS and are ready to be transferred onto the target substrate. Under an optical microscope, the PDMS stamp is aligned to the target substrate using a translation stage, so that the transferred 2D monolayers precisely overlap with the target region on the substrate. A simple pressing step will release the 2D monolayers. Since the soft PDMS is gently placed on the substrate, this releasing process will not damage the existing surface structures on the target substrate, such as microelectrodes and other 2D monolayers. By simply repeating this transfer process, 2D heterostructures can be built layer by layer.

To show the determining role of the capillary force in this new method, we compare the effectiveness of transferring MoS_2 flakes by dry and vapor-wet PDMS stamps in **Figure 4.1 b**. The dry PDMS stamp can hardly pick up any MoS_2 flake from the substrate (**Figure 4.1 b, red path**), whereas the vapor-wet PDMS stamp was able to transfer all flakes underneath to a clean SiO_2/Si substrate (**Figure 4.1b, green path**). It is also worth noting that this quick and easy process requires minimal instrumentation and time. Moreover, in the case where the target material is sensitive to water, other volatile liquids can be used. (e.g. ethanol has been tried to transfer graphene in **Figure 4.2**). Water has larger coefficients of surface tension (~72.9 mN/m at 20°C) than most liquids (e.g. methanol-air, ethanol-air and acetone-air are 22.5, 22.4 and 24.0 mN/m at 20°C, respectively). It is thus preferred in the capillary-force-assisted transfer technique. On the other hand, ethanol and methanol can also be good choices since they are highly hydrophilic to many materials, including PDMS, SiO_2 and 2D materials. **Figure 4.2** shows the graphene transferred by using ethanol. The major difference between using ethanol (methanol) and water in this technique is that the former needs shorter time interval between condensing the liquid and covering PDMS on the target substrate, since the condensed ethanol (methanol) dries fast after leaving the beaker.

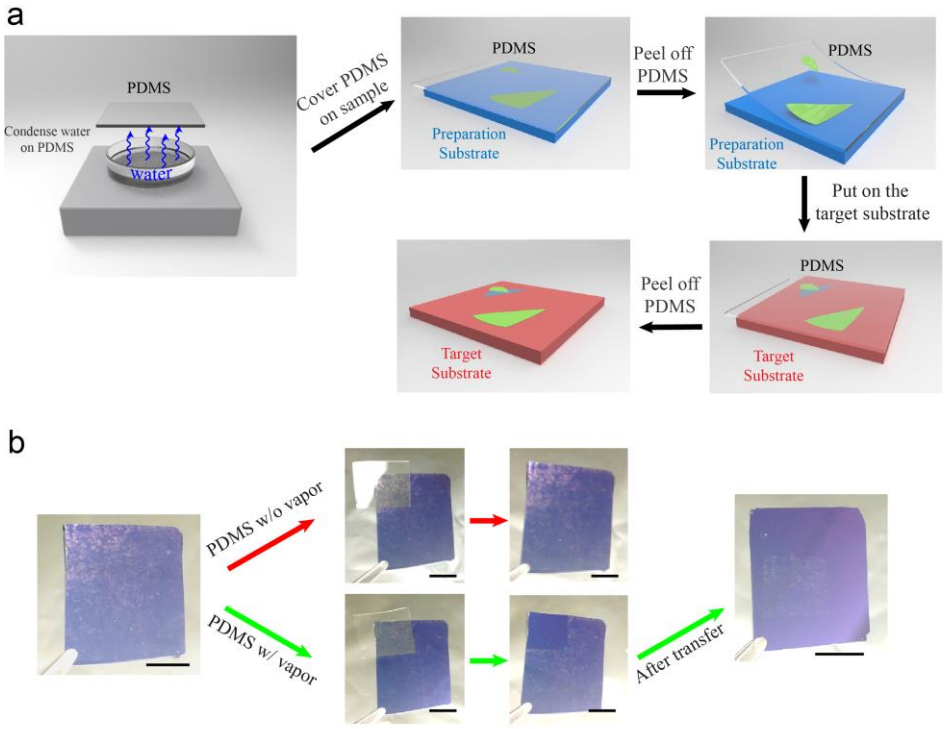

Figure 4.1 The transfer process. **a,** Schematic diagram of the capillary-force-assisted transfer procedure. **b,** the comparison between the adhesion capability of a dry polydimethylsiloxane (PDMS) film and a wet PDMS film. The dry one cannot peel off any molybdenum disulfide (MoS_2) flakes from the SiO_2 substrate (upper row, red path), while a wet PDMS film can pick up all flakes (lower row, green path). The picked-up flakes can be transferred to the target substrate (right). All scale bars are 1cm. A standard PMMA-assisted method can be found in Supporting Information for comparison.

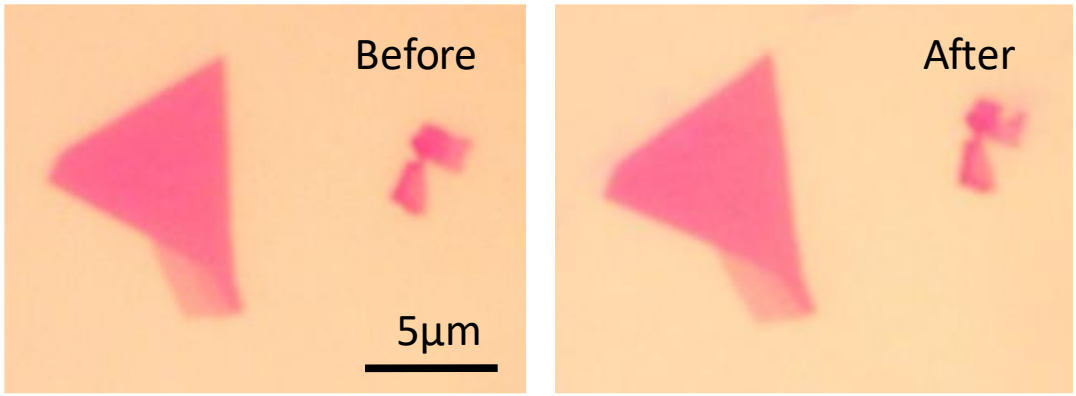

Figure 4.2 Using ethanol in the capillary-force-assisted transfer method to transfer a multi-layer graphene flake.

4.3 Two-dimensional materials transfer results

4.3.1 Transfer of exfoliated two-dimensional materials

Figure 4.3 shows the optical microscope images and atomic force microscopy (AFM) characterization of the transferred results. Large-area graphene flakes containing both single and multilayer regions were transferred with high fidelity from a 290nm-SiO_2/Si substrate (**Figure 4.3 a**) to another SiO_2/Si substrate (**Figure 4.3 b**). The AFM image (**Figure 4.3 c**) shows that both monolayer and multilayer regions of the graphene flake are

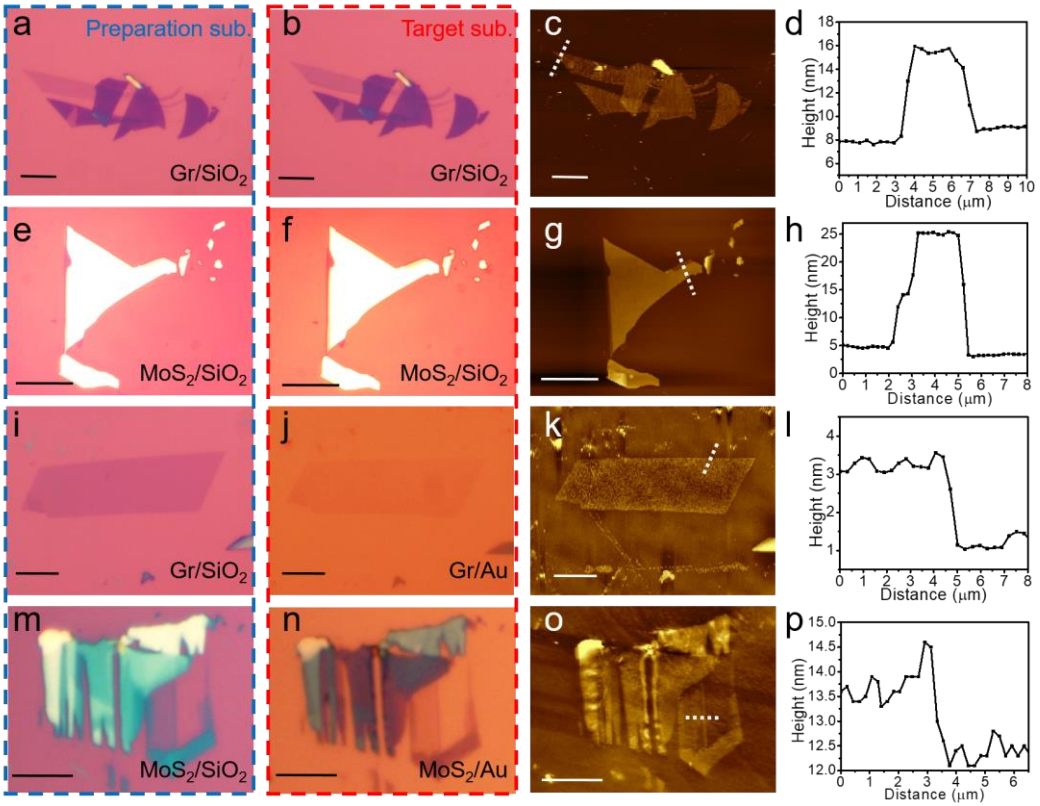

Figure 4.3 Optical microscope images and atomic-force microscope (AFM) cross-section images of graphene and MoS_2 flakes transferred from the preparation substrates (290nm-SiO_2/Si, labeled as SiO_2) to the target substrates (290nm-SiO_2/Si and super-flat gold substrates). All scale bars are 10 μm.

wrinkle and crack free after the transfer. The low roughness of the flake surface indicates that it is clean of any particle or organic residues. Owing to the low adhesion energy on a dry PDMS, the graphene flakes can also be released to other types of substrate, such as a freshly peeled ultra-flat gold substrate (**Figure 4.3 i~k**, surface roughness 0.6 nm), prepared by the fabrication method introduced elesewhere[22, 23]. This transfer technique can be applied not only to hydrophilic materials like graphene but also to hydrophobic materials, such as molybdenum disulfide (MoS_2). **Figure 4.3 e** and **m** show the optical microscope images of MoS_2 flakes transferred to a 290nm-SiO_2/Si substrate and a gold substrate with high fidelity, respectively.

4.3.2 Transfer of chemical vapor deposition (CVD) two-dimensional materials

We have tested this new transfer technique on CVD-prepared graphene samples. The CVD graphene is synthesized following typical CVD recipes, as reported elsewhere[24]. The average domain size is ~ 10μm. We find that only a portion of the graphene can be transferred, as shown in **Figure 4.4**. This low transfer ratio may originate from the large adhesion energy between graphene monolayer and Cu film (~720 mJ/m^2 [25]), and also the non-uniform adhesion energy distribution. For example, the rich sp^3 bonds near domain boundaries may give higher adhesion energy than the basal planes.

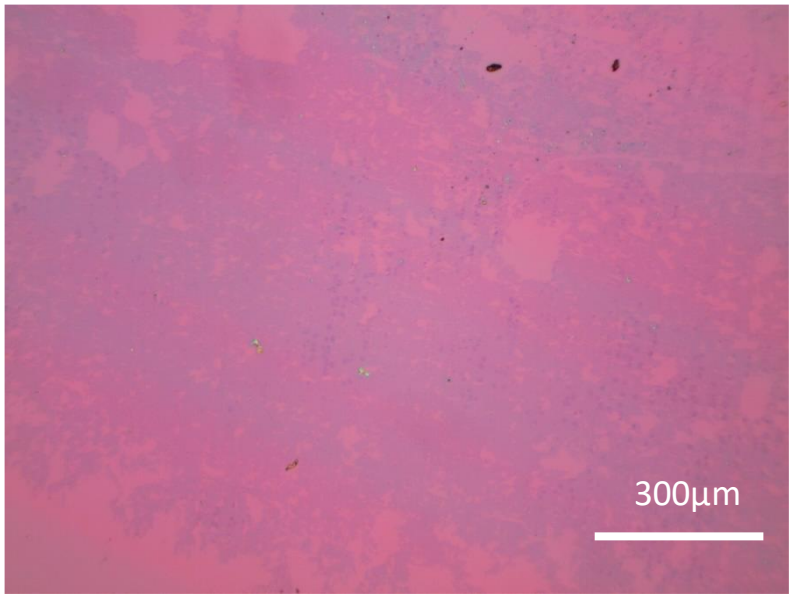

Figure 4.4 Optical microscopy image of the CVD graphene transferred results. It was transferred from the original copper film to a 290nm-SiO_2/Si wafer.

We have tested this new transfer technique on CVD-prepared MoS_2 samples as well. The CVD MoS_2 is synthesized following typical CVD recipes, using sulfide vapor and MoO_2 as sources. The average domain size is 5~20 μm. Unfortunately, there are only a few leading groups have this capability and we have no access to wafer-sized samples. We tried to grow MoS_2 with our own CVD to transfer, as shown in **Figure 4.5**. The result is very promising and we believe that the same technique should work for large-scale CVD MoS_2 as well.

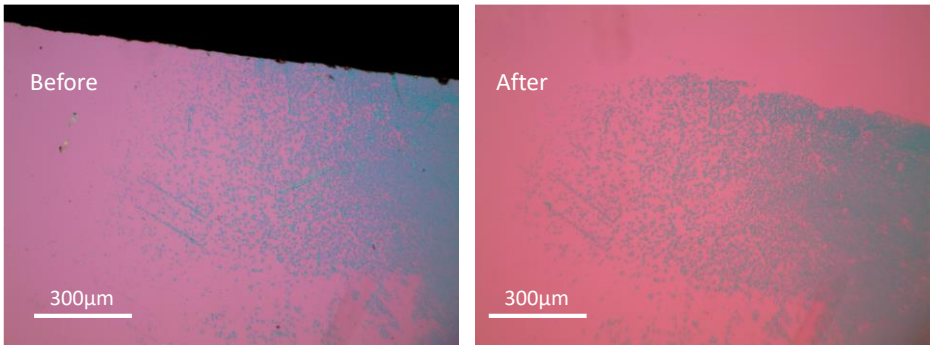

Figure 4.5 Optical microscopy image of the CVD MoS_2 transferred results (Left: before and Right: after transfer). It was transferred from one corner of the original SiO_2/Si wafer to the center of another 290nm-SiO_2/Si wafer.

4.4 Keys influenced the transfer method

4.4.1 Influence of water thickness to the transferred results

The thickness of water film is not playing a critical role in peeling off the 2D flakes from the substrate. However, we do notice that the 2D flakes have poorer fidelity if a large amount of water is condensed on PDMS (eg. the PDMS looks frosted). We suppose that the distortion happens after peeling off. If there is still much water between 2D flakes and PDMS, the surface tension may distort the 2D flakes. **Figure 4.6** shows the transferred results with a thick water film.

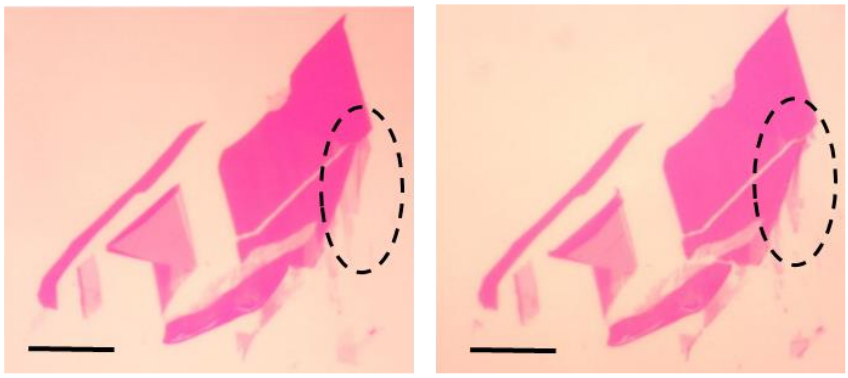

Figure 4.6 A graphene flake transferred by thick water layer on PDMS. The change in film morphology may due to the random floating of graphene flakes on the water film surface, after it was peeled off from the substrate. Scale bar is 10µm. Left: before transfer. Right: after transfer.

4.4.2 Role of water in transferring

In order to exclude other effects like force from water (polarity) modification, etc., we record a video. **Figure 4.7** includes the screenshots from the video to explain the experiment. In the 1st row (**Figure 4.7 a~c**), we show that a dry PDMS film cannot transfer graphene flakes. In the 2nd row (**Figure 4.7 d~f**), the surfaces of both the PDMS and the substrate were shortly covered with water and then naturally dried. The graphene flakes still cannot be picked up from the substrate, demonstrating that the adhesion force is not from any potential surface chemical modification induced by water. In the last row (**Figure 4.7 g~i**), with the presence of water, the graphene flakes are attached to the PDMS film and move out of the microscope focus (meanwhile the meniscus is still under focus, to show that it is not due to changing of microscope focus). This comparison clearly shows that the capillary force is the major source of the adhesion.

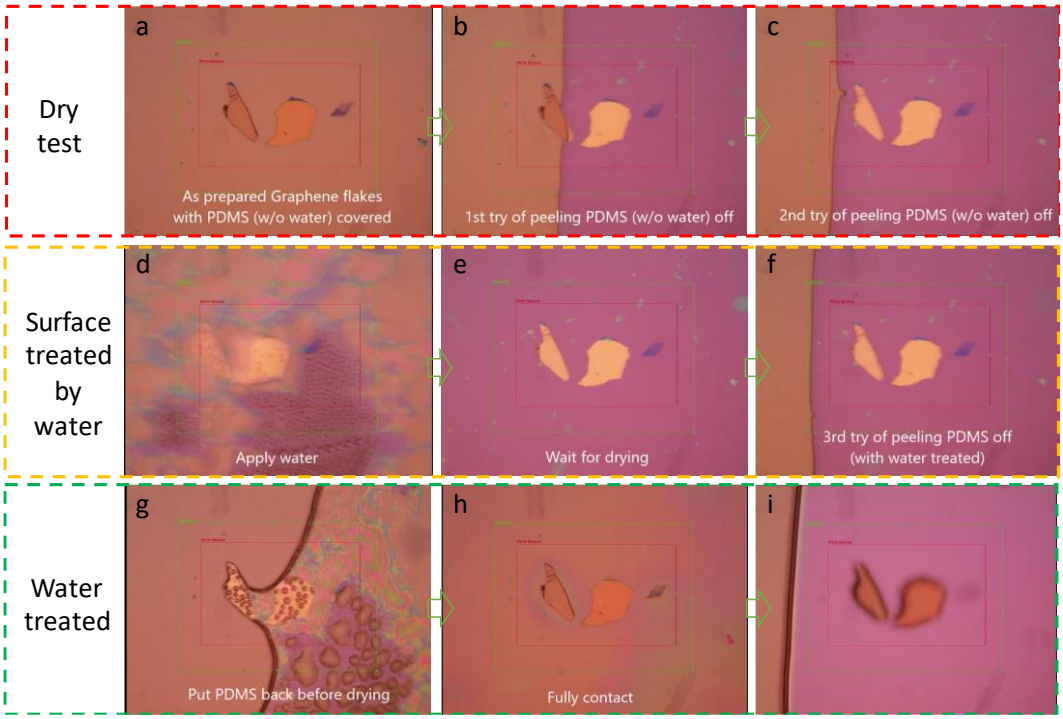

Figure 4.7 Screenshots of a supporting information video. **a-c**, a piece of dry PDMS cannot pick up graphene flakes from the substrate. **d-f**, after water changed the surface conditions of PDMS and substrate, the flakes still cannot be picked up. **g-i**, when a thin water film is sandwiched between PDMS and sample substrate, the graphene flakes are picked up by the PDMS and start to move out of the microscope focus. Note that the meniscus line is still under focus in **i**.

4.4.3 Role of water in transferring

Thicker MoS_2 flakes may need larger capillary force to pick up. This extra force can be estimated from the mechanical energy stored in a bent MoS_2 flake.

The elastic coefficient k of a rectangular MoS_2 flake with one side fixed and one side free is:

$$\mathrm{k} = E\frac{wh^3}{4l^3} \qquad \textbf{eq. 4.1}$$

Here E is Young's modulus (bulk MoS_2 is 238Gpa [26, 27]), l is the flake length, h is the flake thickness, and w is the width[28]. Assuming the displacement of the free end is x, the mechanical energy stored in this bent cantilever is

$$E\text{nergy}=\frac{1}{2}kx^2 \qquad \textbf{eq. 4.2}$$

Considering a MoS_2 flake with 50μm in width, 50μm in length, and 10nm in thickness (about 20 layers). Bending degree α=10° gives $x=8.7\mu m$. The calculated mechanical energy in the flake is 3.6mJ/m^2, which is much smaller than adhesion energy generated by capillary force (~600mJ/m^2).

4.5 Device fabrication

It is very easy to fabricate two-dimensional materials devices, including van der waal's (vdW) heterostructure using this new vapor-assisted PDMS clean stamp transfer method. Using a microscopy and a 3D manipulator, the 2D nano devices can easies fabricated directly as shown in the **Figure 4.8**. In the section, I will introduce two kind of 2D materials using this method to show the convenience and cleanness of this method.

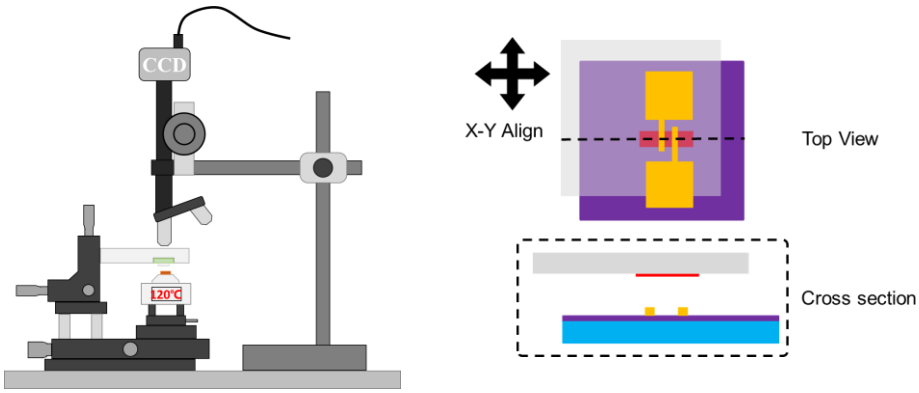

Figure 4.8 The 2D materials devices fabrication set-up.

4.5.1 Graphene back gate FET fabrication and characterization

A three-terminal back-gated graphene field-effect transistor (Gr-FET) was fabricated to characterize the electrical properties of graphene monolayers prepared by this method. The device layout is shown in **Figure 4.9 a**. It was prepared by transferring a graphene monolayer directly onto pre-patterned electrodes (10nm/80nm/3nm Pd/Au/Cr, from top to bottom), which were defined by standard photolithography and metal deposition. This fabrication process avoids the direct contact of the graphene monolayer with any polymer solution, such as PMMA or photoresist, and thus minimizes the contamination from polymer residuals. The quality of the transferred graphene was confirmed by Raman spectroscopy. As shown in **Figure 4.9 c**, the spectrum features a symmetric Lorentzian-shaped G band centered at 1584.0 cm^{-1} and a 2D band at 2675.4 cm^{-1}, with narrow peak widths at FWHMs (full width at half-maximum) of 11.6 cm^{-1} and 27.6cm^{-1}, respectively. The absence of the D' band at 1620 cm^{-1} indicates a low density of random impurities or surface charges. This is also evidenced in the undetectable D band, which is caused by the disorders in sp^2 hybridized carbon system. The average intensity ratio of the 2D/G is larger than 2, further confirming the high-quality of the monolayer graphene. No PMDS peak (~1410cm^{-1}) shows up in the spectrum. All of these Raman characterization results are in good consistency with the high-quality monolayer graphene reported in the literature.

The cleanliness of the transferred graphene monolayer is also evidenced in the current-voltage characteristic of the Gr-FET device. **Figure 4.9 b** shows the room-temperature conductivity as a function of the back-gate voltage (V_{BG}) of the device. The V_{BG} for the

charge neutral point (CNP) is very close to zero ($V_{BG,CNP}$ = 0.45 V with 300-nm SiO_2 as gate oxide) in the as-prepared device, revealing a charge-neutral doping level (n_{CN}) of ~3×10^{10} cm^{-2}, where $n_{CN}=\alpha V_{BG,CNP}$, with $\alpha=7.2\times10^{10}$ $cm^{-2}V^{-1}$ derived from a parallel-plate capacitor model. The carrier mobility of the device can be extracted from a device model with the contact resistance and considered[29]. The mobility is found ~ 48,820 cm^2 V^{-1} s^{-1} at room temperature.

The transportation characteristics of the device are measured at room temperature using a two-terminal method. The total device resistance R_{tot} is the sum of contact resistance $R_{contact}$ and graphene channel resistance $R_{channel}$. We analysis the circuit following the model proposed by Banerjee *et al.*:[29]

$$R_{tot} = R_{contact} + R_{channel} = R_{contact} + \frac{N_{sq}}{n_{tot} e m} = R_{contact} + \frac{N_{sq}}{\sqrt{n_0^2 + n[V_{BG} - V_{CNP}]^2}\, e m} \qquad \textbf{eq. 4.3}$$

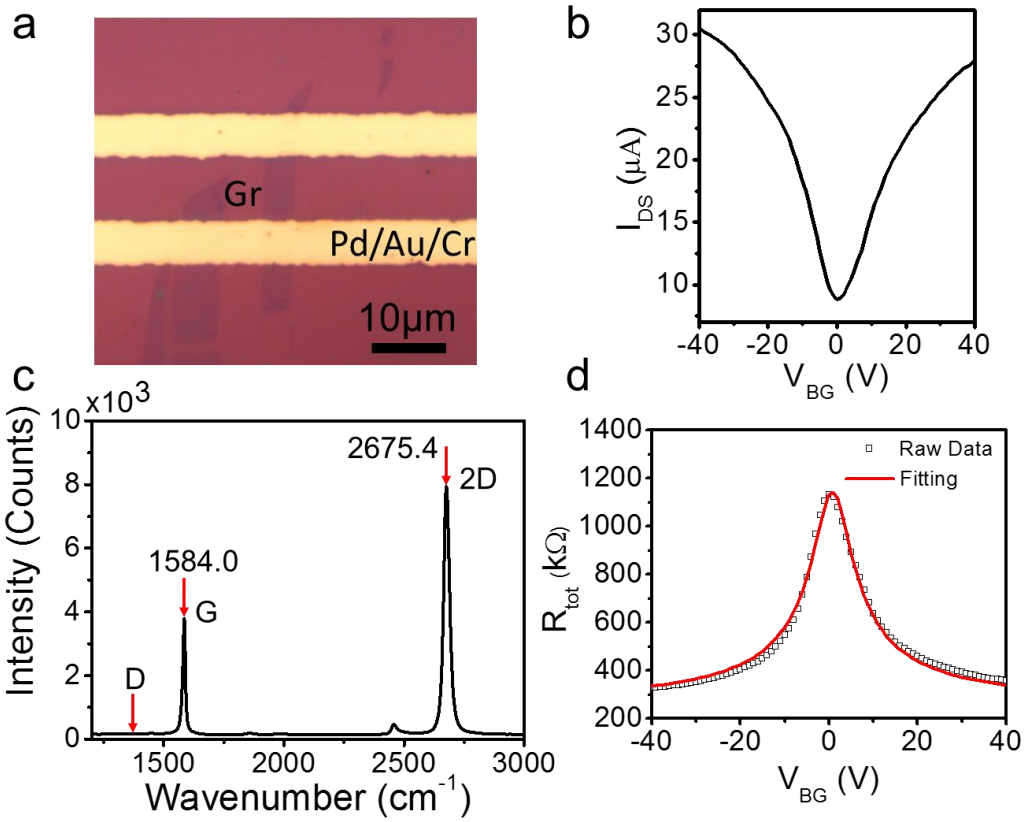

Figure 4.9 Electrical and Raman characteristic of a graphene FET prepared by direct transferring of a graphene monolayer onto electrodes. **a**, the optical microscope image of the device layout. The electrode contains 10nm Pd, 80nm Au, and 3nm Cr. **b**, source-drain current of the Gr-FET vs the back-gate bias V_{BG}, measured under ambient conditions at room temperature. The thickness of the SiO_2 gate oxide is 300nm. V_{DS} is 10mV. The charge-neutral-point gate voltage is 0.45V. **c**, Raman spectrum of the graphene channel region. **d**, The total resistance R_{tot} vs V_{BG} with both experiment data (squares) and modeling result (line).

Here N_{sq} represents the length-to-width ratio of the graphene channel, n_0 is the residual charge carrier concentration, V_{CNP} is the back-gate voltage corresponding to the charge-neutral point, μ is carrier mobility. The expression for the back-gate voltage induced carrier concentration $n[V_{BG} - V_{CNP}]$ can be obtained from a simple parallel plate capacitor model:

$$V_{BG} - V_{CNP} = \frac{e}{C_{ox}} n[V_{BG} - V_{CNP}] \qquad \textbf{eq. 4.4}$$

Here the thickness of gate oxide is 300nm. By fitting **eq. 4.3** to the measured data in **Figure 4.9 d**, parameters including $R_{contact}$, n_0, and μ can be derived. We find that the modeling results agree well with the experiment data (squares). The derived parameters are: residual charge carrier $n_0 = 3.25\times10^{10} cm^{-2}$, the carrier mobility $\mu = 48820 cm^2/Vs$, the contact resistance $R_{contact} = 237.2\Omega$, and the charge neutral voltage is 0.453V.

4.5.2 Graphene-MoS_2-graphene photodetector fabrication and characterization

Due to the simplicity of the transfer procedure, the exceptional cleanness of the sample surface, and the capability for repeated stacking of various 2D monolayers, this technique can also be used to prepare high-performance vertically stacked vdW heterostructures. Heterostructure devices have been demonstrated for several applications, including graphene stacked on h-BN for high-mobility FETs[30], tunneling field effect transistors (TFETs) and photodetectors[31, 32]. Previous demonstrations of heterostructure applications mainly rely on PMMA-assisted transfer[30] where the complete removal of polymer residues is challenging, or h-BN-assisted hot-pickup technique where the exposure of 2D materials to electrodes or environments is difficult. The capillary-force-assisted transfer demonstrated here is a quick and convenient method to build them.

As a proof-of-concept, graphene/MoS_2/graphene (Gr/MoS_2/Gr) vdW heterostructure devices (**Figure 4.10 a**) were fabricated and characterized. The active regions were prepared by the successive transfers of a single-layer graphene film (yellow outlined area in **Figure 4.10 b**), a 6nm-thick MoS_2 flake (green color region), and another single-layer

graphene film (blue outlined area) from their original substrates onto pre-patterned electrodes. The positions of the transferred 2D flakes are carefully adjusted through a translation stage during each film transfer, to ensure a large Gr/MoS_2/Gr sandwich area (the overlap of the blue and yellow outlined areas). In this region, the photon-generated electron-hole pairs in the MoS_2 layer can be separated and collected by the top and the bottom graphene electrodes (Gr_T and Gr_B) according to two driving mechanisms. One is the force from the external electric field applied between Gr_T and Gr_B, and the other is from the built-in electric field created by the asymmetric band structures. **Figure 4.10 c** shows the photocurrent as a function of time measured under the alternating 532 nm-laser illumination (spot size ~ 1μm) at four different optical powers (45, 90, 160 and 225μW). The photocurrents have fast temporal responses at both the rising edges (from OFF to ON) and the falling edges (from ON to OFF), and are stable at the "ON" states over long-term (~60 s) measurements. Such clear switching steps and the stable ON current indicate the absence of trapped states at the interfaces, which usually leads to a gradual change of photocurrent due to the slow charge transfer process. The fast photoresponse leads to the high operation speed as a photodetector. To characterize its high-speed performance (**Figure 4.10 d**), we used a mechanical chopper to modulate the laser beam from 1k to 10kHz and used a lock-in amplifier (Stanford Research Systems, SR830) to analyze the short-current photoresponse signals. We observed no drop in photoresponsivity within our experimental temporal resolution (up to 10 kHz). Both V_{DS} and V_{BG} were set to zero during the measurement.

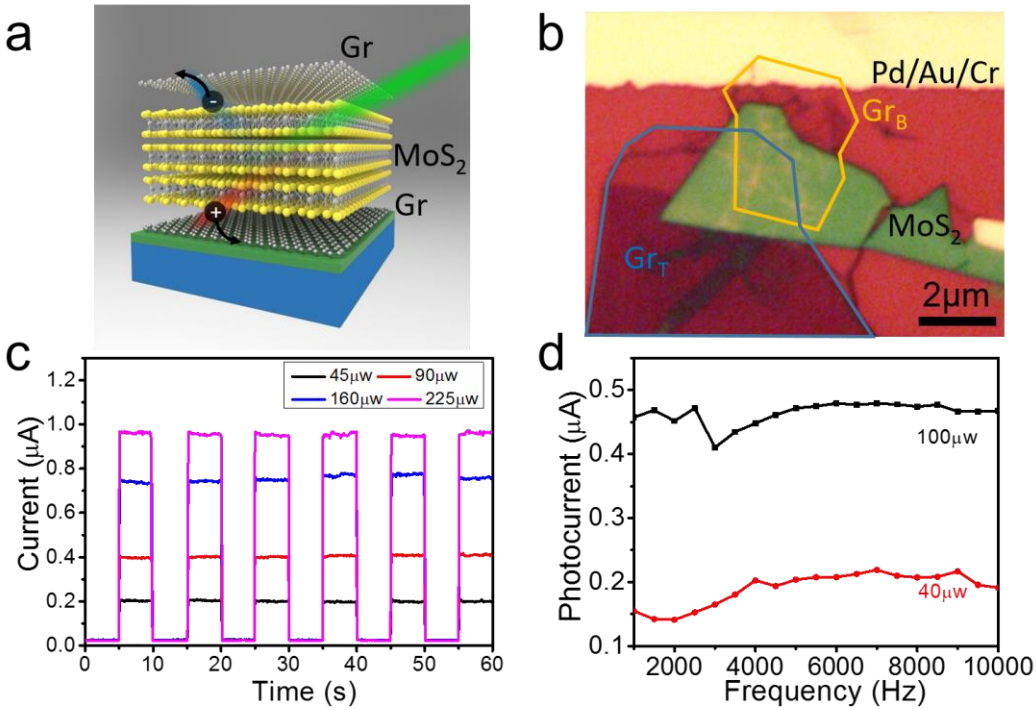

Figure 4.10 Photocurrent generation in a vertically-stacked graphene-MoS_2-graphene heterostructure. **a**, the schematic illustration of the heterostructure device layout. **b**, an optical microscope image of the device, prepared by successive transferring of a monolayer graphene bottom electrode (yellow-outlined region), a few-layer MoS_2 flake, and a graphene top electrode (blue-outlined region) onto the electrode. **c**, the photocurrent measurement of the sandwiched region (intersection of the blue- and yellow-outlined regions), excited by a 532-nm laser with various powers. The characterizations were performed under ambient conditions, with both the bias voltage (V_{DS}) and the back-gate voltage (V_{BG}) set zero. **d**, the frequency-dependent photocurrent measurement.

4.6 Model and theoretical calculation of this transfer method

To verify this capillary force model, we measured the adhesion force between a thin PDMS film and various substrates under dry and wet conditions. A theoretical calculation has been made and both the experimental measurement and the model meet with each other well.

4.6.1 Experimental measurement

A laboratory-developed peeling-off apparatus is used to record the peeling-off force (F_{peel}) needed to separate a PDMS strip from different substrates at velocity v. As shown in **Figure 4.11 b**, a typical specimen contains SiO_2 regions and a 4 mm-wide HOPG region, which is formed of thin HOPG flakes flattened on the SiO_2 substrate. The optical microscopy image of the HOPG flake surface as shown in **Figure 4.12**. Before measuring the dry-condition F_{peel}, the freshly prepared PDMS strips were placed on the substrate directly, followed by 1-hour of relaxation to release stress. To measure the wet-condition F_{peel}, the PDMS strip was hung over a beaker with boiling water for a few seconds to condense water, and then placed on the sample substrate for the immediate measurement. F_{peel} is measured at a low peeling-off rate of 100μm/s. Both the mechanical energy stored in the PDMS film[33] and the influence from the weight change in the vertical part of the PDMS strip were compensated in the data analysis. The black curve in **Figure 4.11 c** shows the F_{peel} at the dry condition. It starts at around 550mN/m on SiO_2 and drops steeply to ~40 mN/m when the separation region reaches the SiO_2-to-HOPG boundary. At the HOPG-to-SiO_2 boundary, F_{peel} gradually returns to 550 mN/m. Then the separation front starts to move on again and F_{peel} remains at around 550 mN/m. Since the F_{peel} on glass stays at the similar level throughout the operation of the experiment (~3min), we believe that the swelling effect in PDMS, which is at the time scale of hours[34], can be ignored here. The adhesion energy between HOPG and PDMS (~40 mJ/m^2) is much lower than that between a graphene monolayer and SiO_2 (~240 mJ/m^2)[15], which explains why PDMS cannot pick up a graphene monolayer directly from a SiO_2 substrate. In the wet-condition measurement,

F_{peel} is lowered to ~450 mN/m on the SiO_2 surface, but on HOPG surface it significantly increases to ~200 mN/m. It is large enough to overcome the binding energy between graphene and SiO_2, leading to the peeling-off of graphene from the substrate. Moreover, the F_{peel} in our experiment is limited by the large surface roughness of HOPG flakes (more details in Supporting Information), which increases the average a and lowers F_{peel}. The adhesion energy on a flat graphene surface can be larger than 200 mJ/m^2, which may be

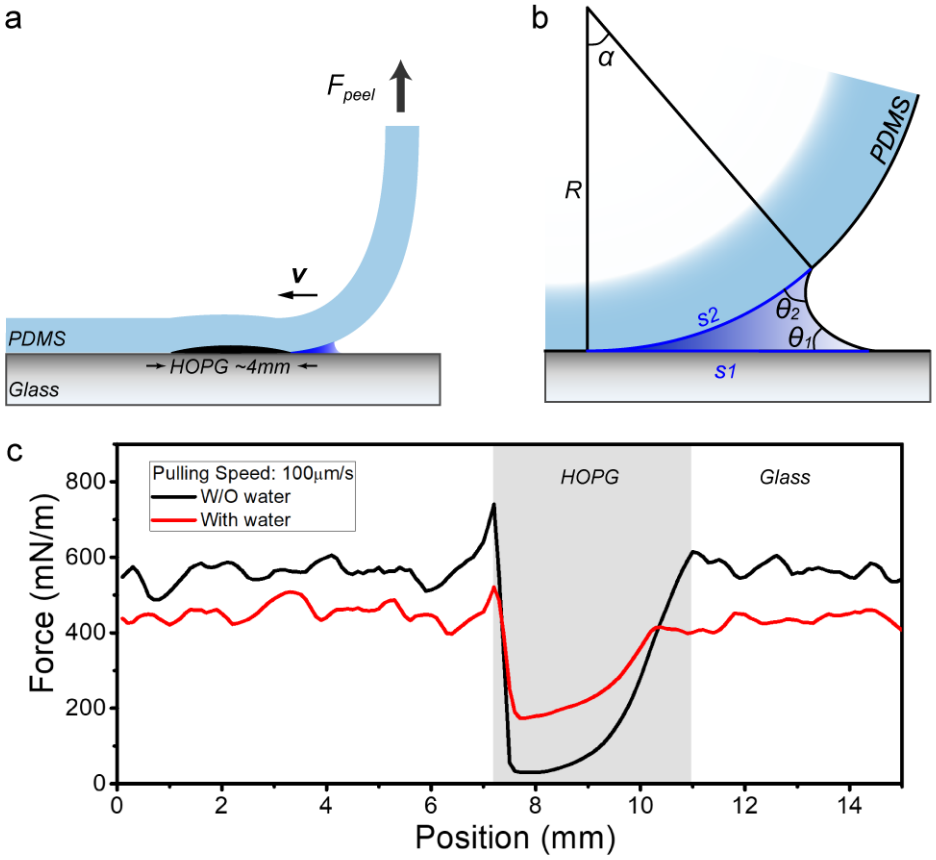

Figure 4.11 Capillary force model analysis and experimental measurement. **a**, schematic of the adhesion force measurement using a thin PDMS stipe stamp on the target substrate, which contains a 4 mm-wide highly-oriented pyrolytic graphite (HOPG) region. **b**, mechanism schematic of capillary interaction between PDMS and substrate. **c**, adhesion force measurement under dry and wet conditions, measured at a peeling-off rate of 100μm/s. The adhesion force on HOPG is dramatically increased under the presence of a meniscus bridge.

utilized to transfer 2D materials from more adhesive substrates, such as metals. We tested this transfer method on graphene monolayers and MoS_2 monolayer domains prepared by chemical vapor deposition (CVD) methods on copper films and SiO_2 substrates, respectively. Since the adhesion energy between graphene and Cu surface is high (~720 mJ/m^2 [25]), only about half of the total area was transferred. (**Figure 4.4**). In the CVD-MoS_2 case, all MoS_2 domains were transferred (**Figure 4.5**).

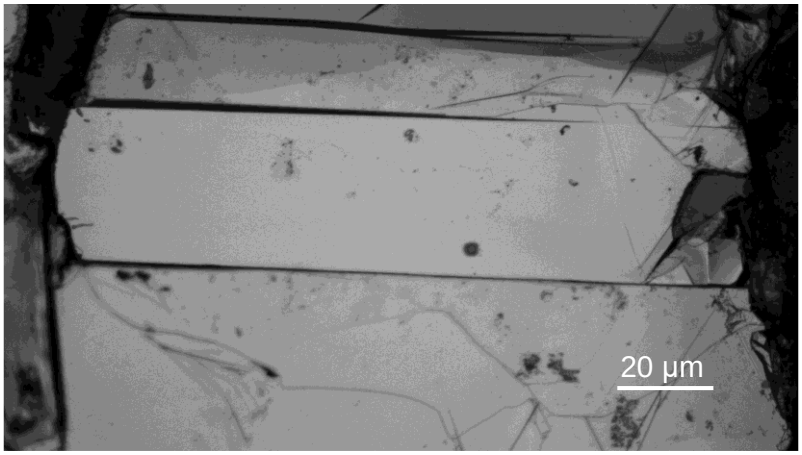

Figure 4.12 Optical microscope image of the HOPG flake sample used for the peel-off force measurement.

4.6.2 Capillary force model and equation derivation

We develop a model for the capillary force analysis, as shown in **Figure 4.11 b**. Here in **Figure 4.13**, more parameters are labeled for the equation derivation. The water meniscus is formed between the PDMS strip and the substrate, originating from the water condensed onto the PDMS surface before the transfer. Here, we assume that the curled PDMS strip has a radius of R, and the fragment of the meniscus region (s_2) corresponds to an angle α.

Note that since R is much larger than s_2, α is a small number and is consequently used here to simplify the equations. The meniscus has a radius ρ.

According to the Laplace formula, the difference between the pressure in liquid and air (atmospheric pressure) is:

$$\Delta P = \gamma_L(\frac{1}{\rho} - \frac{1}{R}) \approx \frac{\gamma_L}{\rho}, (\rho << R) \qquad \textbf{eq. 4.5}$$

This pressure is applied to both s_1 and s_2. Due to the balance of the vertical forces in this system, the peel-off force equals to the Laplace force on s_1, which has the length of:

$$s_1 = (2\sin\frac{\alpha}{2}R)\cos\frac{\alpha}{2} + l$$

Since in this case α is a small number, this equation can be simplified as

$$s_1 = \alpha R + l$$

Where $$l = \sqrt{(2\rho\cos(\frac{\theta_1+\theta_2+\alpha}{2})^2 - (2\alpha R\sin^2\frac{\alpha}{2})^2} \approx 2\rho\cos(\frac{\theta_1+\theta_2}{2})$$

On the other hand, the meniscus radius ρ can be given by

$$\rho = \frac{2\sin^2\frac{\alpha}{2}R}{\cos(\theta_1)+\cos(\theta_2+\alpha)}$$

Moreover, again, it can be simplified as

$$\rho = \frac{\alpha^2 R}{2(\cos\theta_1+\cos\theta_2)}$$

Consequently, s_1 can be re-written as

$$s_1 = \alpha R + \frac{\alpha^2 R}{2(\cos\theta_1 + \cos\theta_2)} \cos\left(\frac{\theta_1 + \theta_2}{2}\right) \approx \alpha R = s_2$$

As s_1 is close to s_2, the vertical force on s_1 has the similar amplitude (but opposite direction) as the force on s_2, which can be given by

$$F = \Delta P \cdot s_2 = \Delta P \cdot \alpha R = \frac{\gamma_L}{\rho} \alpha R = \frac{2\gamma_L (\cos\theta_1 + \cos\theta_2)}{\alpha} \qquad \textbf{eq. 4.6}$$

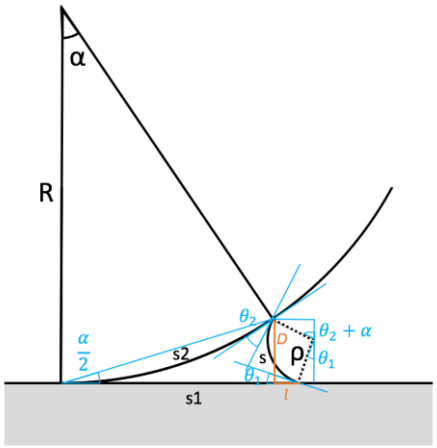

Figure 4.13 Schematic of the capillary force analysis model.

To measure the static contact angles, deionized water droplets were placed on the sample substrates by a syringe needle, and a microscope camera was used to take pictures from the side for the measurement (**Figure 4.14 d~f**). To measure the dynamic contact angle, the substrates were placed vertical, and water was fed to the droplet via the syringe needle. When the weight of the droplet is larger than the pressure difference between the wetting and dewetting edges, the droplet starts to move downward due to the gravitational force and both wetting and dewetting angles can be measured (**Figure 4.14 a~c**). Three types of substrates, including PDMS, glass, and HOPG, are measured. All the dewetting angles are significantly smaller than their corresponding static contact angle.

As shown in equation **eq. 4.6**, the contact angle α between the PDMS film and the substrate directly determines the amplitude of the capillary force. To measure α, we utilize the interference pattern formed at the gap region, as shown in **Figure 4.15**. The interference pattern was created by the interference of the light (532nm in wavelength) reflected from the upper surface of the glass and that from the bottom surface of the PDMS film (**Figure 4.15 a**). Since the refractive indices of water, PDMS and glass are similar, the reflections from water/PDMS and water/glass interfaces are weak, and no interference pattern was observed in the water bridge region (the PDMS/Water/Glass region). The interference pattern near the water meniscus front line can be used to calculate α directly. Using this method, we find that α is in the range of 5° ~ 30°, which is mainly determined by the pulling direction on the free-standing-end of the PDMS film.

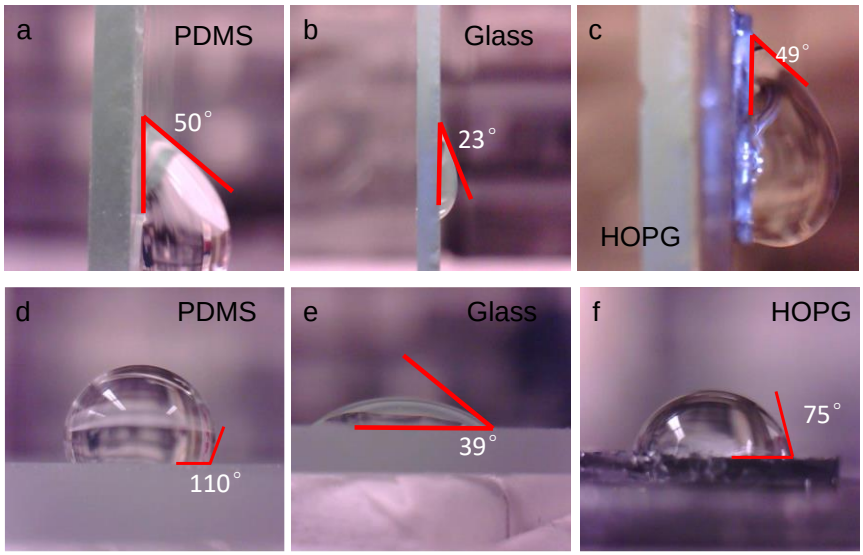

Figure 4.14 The water contact angle **a-c**, the dewetting contact angles of water on PDMS, glass and HOPG, respectively. **d-f,** the static contact angles on the same substrates. Note that the dewetting angles are drastically smaller than the static contact angles in both hydrophobic and hydrophilic cases.

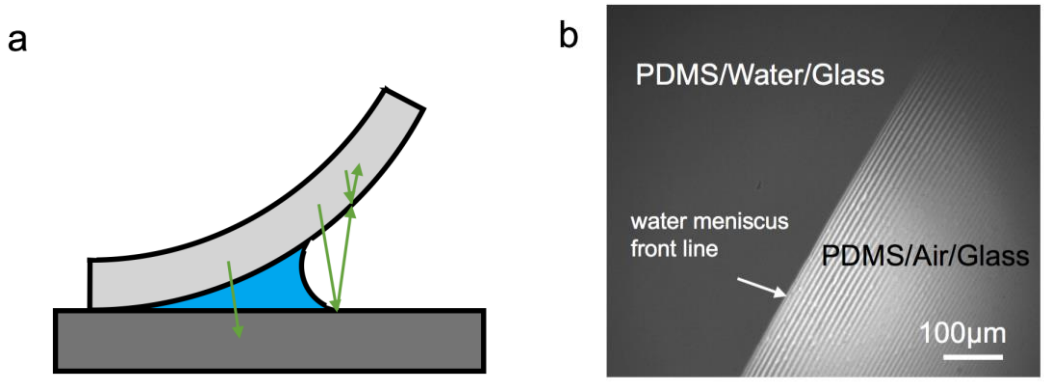

Figure 4.15 The optical interference method used to measure the angle α between PDMS and the glass substrate. **a,** schematic illustration of the interference mechanism. **b,** optical microscope image of the interference pattern formed at the PDMS/Air/Glass region, formed by the light reflected from the PDMS/Air and Air/Glass interfaces. The illumination light has the wavelength of 532 nm. The measured α in this case is ~6°.

4.7 Summary

In summary, a simple and clean stamp transfer method for 2D materials is developed. Using a thin layer of water as an instant yet temporary glue, the adhesion energy between PDMS and 2D materials can be significantly increased during the peeling off process and restored shortly to facilitate the releasing process. The Gr-FET device characterization reveals a very low impurity level on graphene monolayer after the transfer. High-quality Gr/MoS_2/Gr vertical heterostructures with clean interfaces are fabricated to show the convenience of this method for constructing complicated heterostructures. Moreover, the mechanism model study discloses that higher capillary force can be achieved by using smaller contact angle α between PDMS and the substrate, which will stimulate further investigation of using this method for transferring large-scale 2D materials, and accelerate the development of 2D material studies.

4.8 References

1. Huang, X.; Yin, Z. Y.; Wu, S. X.; Qi, X. Y.; He, Q. Y.; Zhang, Q. C.; Yan, Q. Y.; Boey, F.; Zhang, H. *Small* **2011,** 7, (14), 1876-1902.

2. Novoselov, K. S.; Fal'ko, V. I.; Colombo, L.; Gellert, P. R.; Schwab, M. G.; Kim, K. *Nature* **2012,** 490, (7419), 192-200.

3. Zhang, Y.; Zheng, B.; Zhu, C.; Zhang, X.; Tan, C.; Li, H.; Chen, B.; Yang, J.; Chen, J.; Huang, Y.; Wang, L.; Zhang, H. *Advanced Materials* **2015,** 27, (5), 935-939.

4. Toth, P. S.; Velický, M.; Bissett, M. A.; Slater, T. J. A.; Savjani, N.; Rabiu, A. K.; Rakowski, A. M.; Brent, J. R.; Haigh, S. J.; O'Brien, P.; Dryfe, R. A. W. *Advanced Materials* **2016,** 28, (37), 8256-8264.

5. Shi, J. P.; Liu, M. X.; Wen, J. X.; Ren, X. B.; Zhou, X. B.; Ji, Q. Q.; Ma, D. L.; Zhang, Y.; Jin, C. H.; Chen, H. J.; Deng, S. Z.; Xu, N. S.; Liu, Z. F.; Zhang, Y. F. *Advanced Materials* **2015,** 27, (44), 7086.

6. Li, Q.; Zhao, Z.; Yan, B.; Song, X.; Zhang, Z.; Li, J.; Wu, X.; Bian, Z.; Zou, X.; Zhang, Y.; Liu, Z. *Advanced Materials* **2017,** 29, 1701325.

7. Suk, J. W.; Kitt, A.; Magnuson, C. W.; Hao, Y. F.; Ahmed, S.; An, J. H.; Swan, A. K.; Goldberg, B. B.; Ruoff, R. S. *Acs Nano* **2011,** 5, (9), 6916-6924.

8. Liang, X. L.; Sperling, B. A.; Calizo, I.; Cheng, G. J.; Hacker, C. A.; Zhang, Q.; Obeng, Y.; Yan, K.; Peng, H. L.; Li, Q. L.; Zhu, X. X.; Yuan, H.; Walker, A. R. H.; Liu, Z. F.; Peng, L. M.; Richter, C. A. *Acs Nano* **2011,** 5, (11), 9144-9153.

9. Kidambi, P. R.; Boutilier, M. S. H.; Wang, L.; Jang, D.; Kim, J.; Karnik, R. *Advanced Materials* **2017,** 29, (19), 1605896.

10. Desai, S. B.; Madhvapathy, S. R.; Amani, M.; Kiriya, D.; Hettick, M.; Tosun, M.; Zhou, Y. Z.; Dubey, M.; Ager, J. W.; Chrzan, D.; Javey, A. *Advanced Materials* **2016,** 28, (21), 4053-4058.

11. Li, H.; Wu, J. M. T.; Huang, X.; Yin, Z. Y.; Liu, J. Q.; Zhang, H. *Acs Nano* **2014,** 8, (7), 6563-6570.

12. Meitl, M. A.; Zhu, Z. T.; Kumar, V.; Lee, K. J.; Feng, X.; Huang, Y. Y.; Adesida, I.; Nuzzo, R. G.; Rogers, J. A. *Nat Mater* **2006,** 5, (1), 33-38.

13. Kim, K. S.; Zhao, Y.; Jang, H.; Lee, S. Y.; Kim, J. M.; Kim, K. S.; Ahn, J. H.; Kim, P.; Choi, J. Y.; Hong, B. H. *Nature* **2009,** 457, (7230), 706-710.

14. Scharfenberg, S.; Rocklin, D. Z.; Chialvo, C.; Weaver, R. L.; Goldbart, P. M.; Mason, N. *Appl Phys Lett* **2011,** 98, (9), 091908.

15. Boddeti, N. G.; Koenig, S. P.; Long, R.; Xiao, J. L.; Bunch, J. S.; Dunn, M. L. *J Appl Mech-T Asme* **2013,** 80, (4), 040909.

16. Pizzocchero, F.; Gammelgaard, L.; Jessen, B. S.; Caridad, J. M.; Wang, L.; Hone, J.; Boggild, P.; Booth, T. J. *Nature Communications* **2016,** 7, 11894.

17. Kim, K.; Yankowitz, M.; Fallahazad, B.; Kang, S.; Movva, H. C. P.; Huang, S. Q.; Larentis, S.; Corbet, C. M.; Taniguchi, T.; Watanabe, K.; Banerjee, S. K.; LeRoy, B. J.; Tutuc, E. *Nano Lett* **2016,** 16, (3), 1989-1995.

18. Wang, L.; Meric, I.; Huang, P. Y.; Gao, Q.; Gao, Y.; Tran, H.; Taniguchi, T.; Watanabe, K.; Campos, L. M.; Muller, D. A.; Guo, J.; Kim, P.; Hone, J.; Shepard, K. L.; Dean, C. R. *Science* **2013,** 342, (6158), 614-617.

19. Ma, X.; Liu, Q.; Xu, D.; Zhu, Y.; Kim, S.; Cui, Y.; Zhong, L.; Liu, M. *Nano letters* **2017,** 17, (11), 6961-6967.

20. Lock, E. H.; Baraket, M.; Laskoski, M.; Mulvaney, S. P.; Lee, W. K.; Sheehan, P. E.; Hines, D. R.; Robinson, J. T.; Tosado, J.; Fuhrer, M. S.; Hernandez, S. C.; Waltont, S. G. *Nano Lett* **2012,** 12, (1), 102-107.

21. Kim, H. H.; Kang, B.; Suk, J. W.; Li, N.; Kim, K. S.; Ruoff, R. S.; Lee, W. H.; Cho, K. *Acs Nano* **2015,** 9, (5), 4726-4733.

22. Nagpal, P.; Lindquist, N. C.; Oh, S. H.; Norris, D. J. *Science* **2009,** 325, (5940), 594-597.

23. Zhu, X. L.; Zhang, Y.; Zhang, J. S.; Xu, J.; Ma, Y.; Li, Z. Y.; Yu, D. P. *Advanced Materials* **2010,** 22, (39), 4345.

24. Li, X. S.; Cai, W. W.; An, J. H.; Kim, S.; Nah, J.; Yang, D. X.; Piner, R.; Velamakanni, A.; Jung, I.; Tutuc, E.; Banerjee, S. K.; Colombo, L.; Ruoff, R. S. *Science* **2009,** 324, (5932), 1312-1314.

25. Yoon, T.; Shin, W. C.; Kim, T. Y.; Mun, J. H.; Kim, T. S.; Cho, B. J. *Nano Lett* **2012,** 12, (3), 1448-1452.

26. Bertolazzi, S.; Brivio, J.; Kis, A. *ACS Nano* **2011,** 5, (12), 9703-9.

27. Feldman, J. *Journal of Physics and Chemistry of Solids* **1976,** 37, (12), 1141-1144.

28. Li, H.; Lal, A.; Blanchard, J.; Henderson, D. *Journal of Applied Physics* **2002,** 92, (2), 1122-1127.

29. Kim, S.; Nah, J.; Jo, I.; Shahrjerdi, D.; Colombo, L.; Yao, Z.; Tutuc, E.; Banerjee, S. K. *Appl Phys Lett* **2009,** 94, (6), 062107.

30. Dean, C. R.; Young, A. F.; Meric, I.; Lee, C.; Wang, L.; Sorgenfrei, S.; Watanabe, K.; Taniguchi, T.; Kim, P.; Shepard, K. L.; Hone, J. *Nat Nanotechnol* **2010,** 5, (10), 722-726.

31. Britnell, L.; Gorbachev, R. V.; Jalil, R.; Belle, B. D.; Schedin, F.; Mishchenko, A.; Georgiou, T.; Katsnelson, M. I.; Eaves, L.; Morozov, S. V.; Peres, N. M. R.; Leist, J.; Geim, A. K.; Novoselov, K. S.; Ponomarenko, L. A. *Science* **2012,** 335, (6071), 947-950.

32. Yu, W. J.; Liu, Y.; Zhou, H. L.; Yin, A. X.; Li, Z.; Huang, Y.; Duan, X. F. *Nat Nanotechnol* **2013,** 8, (12), 952-958.

33. Nase, J.; Ramos, O.; Creton, C.; Lindner, A. *European Physical Journal E* **2013,** 36, (9), 103.

34. Koh, K.-S.; Chin, J.; Chia, J.; Chiang, C.-L. *Micromachines* **2012,** 3, (2), 427-441.

Chapter 5 High-contrast RE-TERS imaging: results and discussions

With this RE-TERS probe, a 10 nm spatial resolution was demonstrated on a single-walled carbon nanotube (SW-CNT) sample, and the strain distribution in a monolayer molybdenum disulfide (MoS_2) was mapped. In this chapter, the high spatial resolution of this probe has been demonstrated by imaging of single-walled carbon nanotube supported on 30nm ultra-smooth gold film. Tension strained monolayer MoS_2 has been transferred onto 30nm ultra-smooth gold film using the clean stretchable stamp transfer method introduced in the chapter 4. The high-contrast RE-TERS mapping has been achieved in this chapter.

5.1 Introduction

As the most important parameter for a TERS probe, the spatial resolution has been demonstrated down to the single molecular scale under the condition of the ultra-high vacuum, low temperature (as low as several tens Kelvin degree) and scanning tunneling microscopy (STM) driven. However, the condition is expensive, time-consuming and high demand of light-path alignment. Moreover, some samples need to be examined by TERS cannot be set to the extremely surrounding, for example, tension strain force stored 2D materials sample cannot maintain the strain force under the ultra-high vacuum and extremely low temperature. On the other hand, although some room temperature and pressure high spatial resolution TERS experiments have demonstrated their high spatial

resolution, including STM and AFM based, side scattering, top scattering, transmission or aperture configurations TERS, which is as high as several nanometers, the large background is hard to be eliminated. Moreover, the STM based TERS require the sample conductive to support its feedback loop, which limited its application value. Thus, high signal to noise ratio (i.e. high contrast) and high spatial resolution room temperature and pressure AFM based TERS is highly needed. In this chapter, in order to have a benchmark for the remote-excited TERS probe introduced in chapter 3. Some experiments have been carried out.

5.2 Devices preparation

In this section, I will illustrate the fabrication process of the ultra-smooth gold film, transferring of strain force stored MoS_2 onto the ultra-smooth gold substrate, transferring of single walled CNTs mesh onto the ultra-smooth gold substrate.

5.2.1 Ultra-smooth gold surface substrate preparation

The ultra-smooth gold surface substrate was preparation using this procedure illustrated in **Figure 5.1**. Apply epoxy instant glue onto the 30nm gold film coated on the SiO_2/Si wafer, then put another SiO_2/Si wafer on it. Appealing off the wafer 2 after waiting for one day. The gold film would follow the epoxy and the smooth side will exposed. The RMS of the surface should be same as the SiO_2 surface (0.32nm).

5.2.2 Fabrication method of the strain force stored MoS_2 supported by the ultra-smooth gold substrate

We used the RE-TERS probe to study the strain field on a stressed MoS_2 monolayer flake, for the demonstration of its high-resolution low-background Raman imaging. Raman spectroscopy and microscopy is one of the most powerful tools to study strain and strain

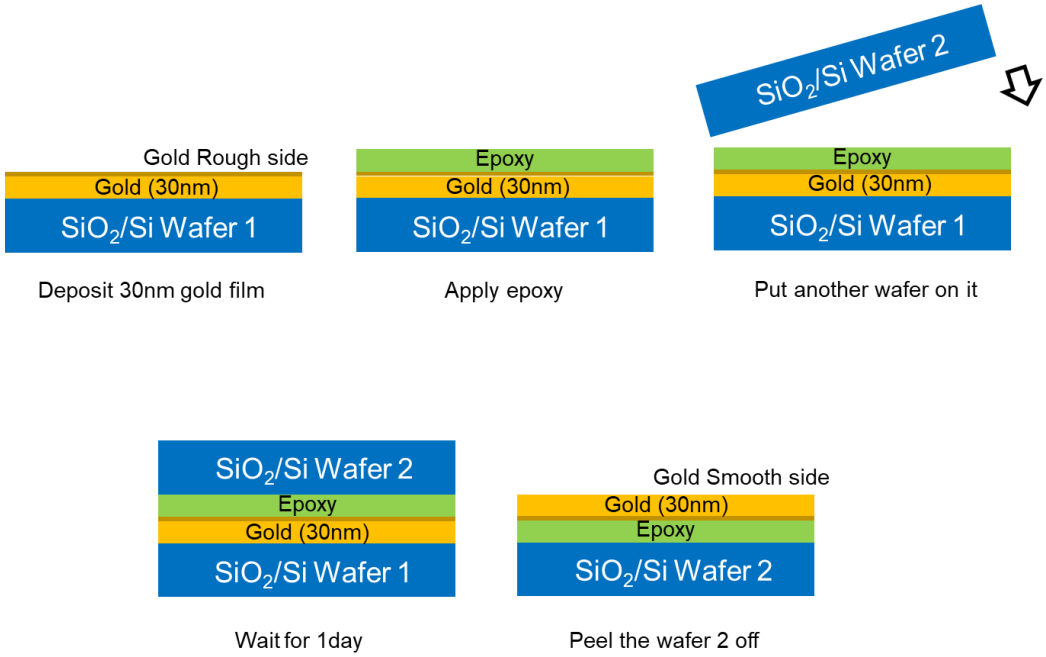

Figure 5.1 The fabrication process of the ultra-smooth surface gold substrate.

distributions in materials[1], and TERS allows for the visualization of localized strain field with nanoscale resolution[2-7]. Such nanoscale strain characterization capability is extremely important for the micro- and nanoscale strain engineering in MoS_2 and other transition metal dichalcogenides, whose bandgap and optoelectronic properties can be tuned by applying strains[8-10]. Recently, TERS has been used to probe the strain field of trilayer[11] and monolayer[12] MoS_2 deposited on Au nanocluster arrays, taking advantage of the giant SERS effect from the localized surface plasmon of Au nanoclusters. However, high-resolution

TERS strain mapping on a pre-stressed MoS_2 flake on an ultra-smooth substrate with minimal structural, optical and thermal inhomogeneity has not yet been demonstrated.

The MoS_2 flake was prepared by a standard chemical vapor deposition (CVD) method on a silicon dioxide substrate[13] and transferred onto an ultra-smooth Au thin-film substrate[14] using the capillary-force-assisted clean-stamp transfer technique we recently developed[15]. The flexible PDMS transfer substrate hosting the MoS_2 flake was gently bent before releasing the flake to the Au substrate, to apply a tensile stress on the flake, as shown in **Figure 5.2 a**. **Figure 5.2 b** shows the topographic image of the MoS_2 flake measured with the RE-TERS probe in contact-mode. The stressed MoS_2 flake displayed multiple folds and cracks. The line scan in height (**Figure 5.2 c**) along the white dashed line demonstrates a ~0.8 nm film thickness, corresponding well to a MoS_2 monolayer[16]. The root mean square (rms) roughness of the Au substrate surface was around 0.32 nm, close to that of a Si wafer[14]. The ultra-smooth Au substrates is important for reducing the contribution of roughness-induced SERS, which could results in artifacts in gap-mode TERS imaging[17].

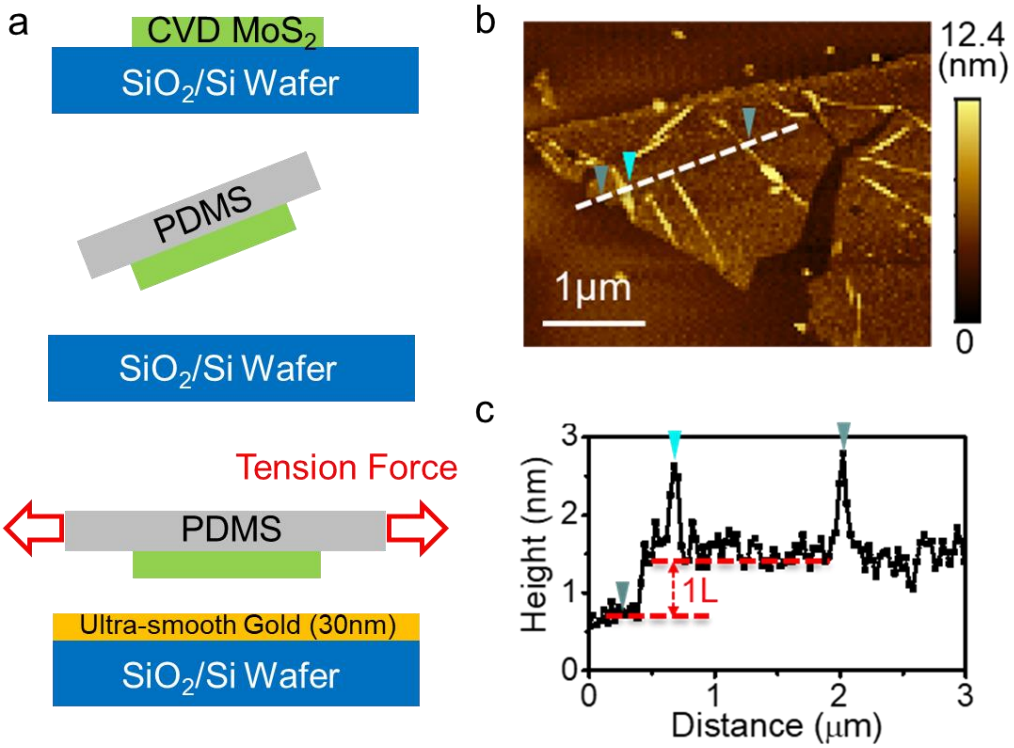

Figure 5.2 Method of stain force apply to MoS_2 flack. **a,** the fabrication process of the tension strained force stored MoS_2 supported by the ultras-smooth gold substrate. **b,** AFM image of the MoS_2 flake. **c,** Line scan profile for the edge of the flake.

5.2.3 Fabrication method of the single walled CNTs supported by the ultra-smooth gold substrate

The SW-CNT was provided by the Sigma-Aldrich Chemistry (St. Louis, United States). Dispersed 1mL the SW-CNTs conductive aqueous ink (791480-25ML, 0.25mg/mL) solution in 20mL deionized water (DI water) followed by sonicated the dilute solution for 30mins. Then sprayed the top solution using a spray gun (Paasche Airbrush) onto the pre-heated (120℃) ultra-smooth gold substrate. **Figure 5.3** shows the AFM image and its line scan profile, 1.03nm diameter demonstrate the single walled of this CNT.

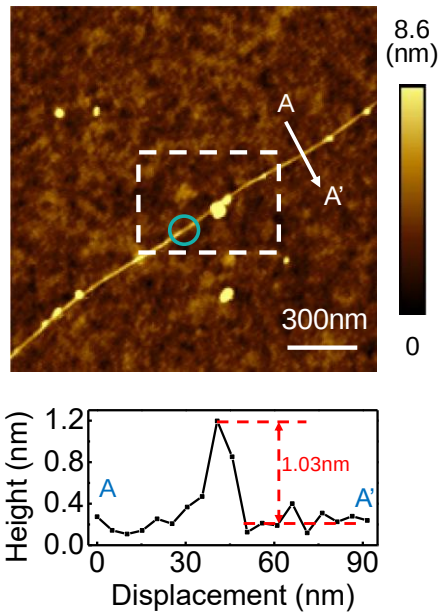

Figure 5.3 AFM image of the single walled CNT supported on the ultra-smooth gold substrate and its line scan profile.

5.3 RE-TERS mapping image of the tension strained force stored MoS_2 flake supported on ultra-smooth gold substrate: result and discussion

Figure 5.4 a-d are the corresponding RE-TERS intensity and Raman shift images of the two major Raman-active modes (E^1_{2g} and A_{1g}) of MoS_2 measured from the same monolayer flake. Near the MoS_2 flake edges, the spectra intensity mapping can be as sharp as one pixel (**Figure 5.4 a**), indicating that the resolution of the TERS probe is at least as good as the step size (50nm, details in Supporting Information). In order to quantify the spatial resolution, we did a line-scan across a domain edge and used the error function to fit the intensity data. 41nm spatial resolution is shown in **Figure 5.5**.

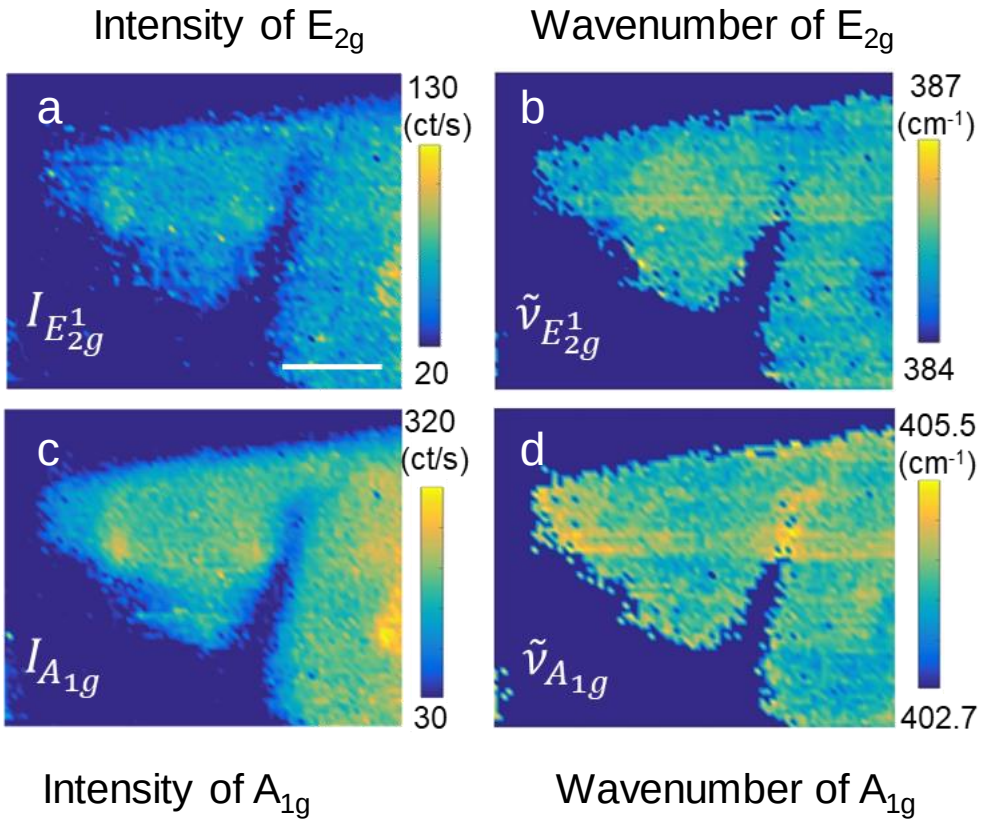

Figure 5.4 RE-TERS mapping image of the strained MoS_2 flake. **a-d,** TERS mapping of the intensities, I (**a** and **c**, in counts per second, ct/s) and the Raman shifts, $\tilde{\nu}$ (**b** and **d**) of the E^1_{2g} and A_{1g} peaks of the MoS_2 flake, respectively. Excitation: 532nm, 0.1 mW at sample surface. Integration time = 1s.

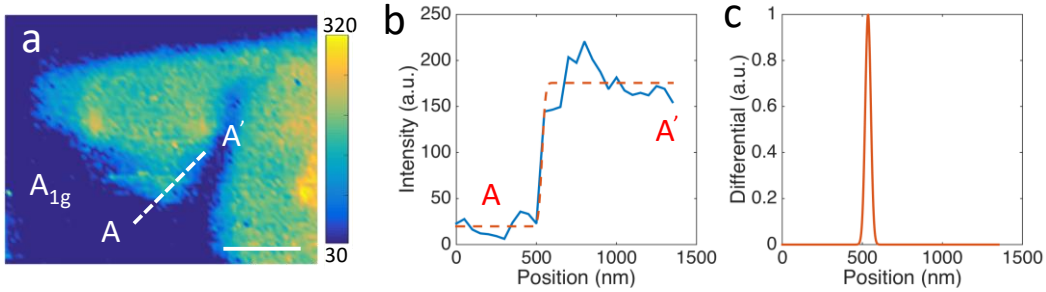

Figure 5.5 The edge of the MoS_2 flake **a,** The A_{1g} Raman peak mapping of MoS_2 flake supported on Au substrate. The image contains 80 by 64 pixels over 4μm by 3.2μm areal. **b,** The blue line is the Raman intensity line scan along the white dashed line from A to A', where the red line is profile of the line scan by performed a step function fitting. **c,** The first derivative of the line fit in **b**. The FWHM shows the spatial resolution of 41nm.

In the TERS images, the E_{2g}^1 peak at 385.4±0.6 cm^{-1} corresponds to the in-plane vibration of the two S atoms and Mo atom in opposite directions, while the A_{1g} peak at 404.1±0.5 cm^{-1} represents the out-of-plane vibration, where the two S atoms move in opposite directions perpendicular to the basal plane. The positions of the two Raman peaks are in good agreement with previous reports of monolayer MoS_2[18-21] and are consistent with the layer thickness measured with the topographical mapping. The intensity maps of the two modes (**Figure 5.4 a and c**) show similar spatial variations that also correspond well with its AFM image: stronger signals were seen where the MoS_2 flake has microscale folds and weaker signal were seen where cracks are found. Such correlations between the MoS_2 morphology and TERS intensity demonstrate the optical uniformity of the ultra-smooth gold substrate. However, the Raman shift maps (**Figure 5.4 c and d**) of the two modes show completely different trends. The peak position of the E_{2g}^1 mode shows consistent red-shifts towards the edges of the flakes and near the cracks, whereas the spatial variation in the A_{1g} mode frequency shows a subtler, but opposite pattern. To better visualize the trend, the frequency difference $\Delta\tilde{\nu}$ ($\Delta\tilde{\nu} = \tilde{\nu}_{A_{1g}} - \tilde{\nu}_{E_{2g}^1}$) between the two modes were plotted in **Figure 5.6 a**. Over the entire flake, $\Delta\tilde{\nu}$ varies from 18.2 to 20.0 cm^{-1}, with an average of ~18.9 cm^{-1}. While all of this value still fall within the monolayer regime[18], there is a strong spatial dependence in $\Delta\tilde{\nu}$, which is ~ 1.8cm^{-1} larger at the edges and near the cracks of the flake than at the center. **Figure 5.6 b** shows a series of 11 TERS spectra collected along the red-arrow pointing from the left edge of the triangular flake to its upper right corner where it was torn due to stress in **Figure 5.6 a**. Spectrum #6 corresponds to the middle of

the arrow and the center position the center of the flake, where appears darkest in **Figure**

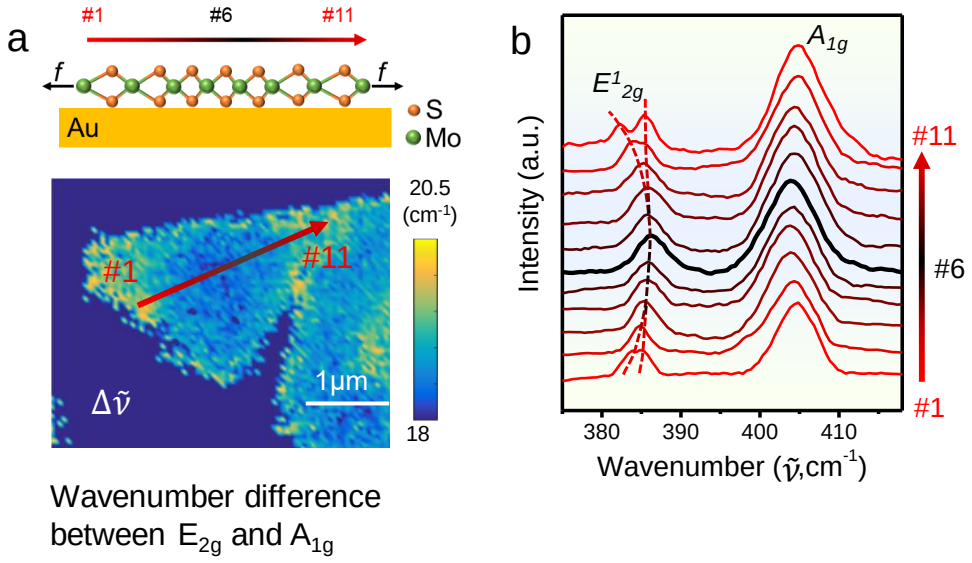

Figure 5.6 Stress-induced Raman peak shifts in MoS_2 monolayer. The bottom panel of **a,** shows the inter-peak spacing, $\Delta\tilde{\nu}$, between the E^1_{2g} and A_{1g} peaks, which changes from ~18 cm^{-1} at the center to ~20.5 cm^{-1} along the edge of the flake. A series of eleven spectra **b**, taken along the red arrow in **a** shows the shifting of both peaks and the splitting of the E^1_{2g} peak towards the edge of the flake (#1 and #11), which is the consequence of the increased tensile stress at the edge as shown in the schematic in the top panel of **a.**

5.6 a with the lowest $\Delta\tilde{\nu}$. Here, the E^1_{2g} and A_{1g} peak positions, line shapes and their frequency difference show typical MoS_2 monolayer characteristics[18]. However, moving towards both edges of the triangular domain (positions #1 and #11), the doubly degenerated E^1_{2g} peak starts to soften and eventually splits into a higher frequency E^+ mode at ~384 cm^{-1} and a lower frequency E^- mode that is significantly red-shifted to ~382cm^{-1}. According to the strain-dependence studies[22], the softening and splitting of the E^1_{2g} mode can be attribute to strain-induced symmetry breaking. The reported E^- mode of 4.5 ± 0.3 cm^{-1}/% uniaxial strain placed that the largest strain stored at the pinned edge of the stressed MoS_2 flake at ~0.9%. In comparison, the out-of-plane A_{1g} mode, which is much less sensitive to

the uniaxial strain, shows only subtle differences along the red-arrow, and the slight blue-shift at the edges may originate from the stronger van der Waals (vdW) interaction between the MoS_2 monolayer and the substrate[23] to sustain the local strain and prevent slipping. Moreover, compared with confocal Raman measurements[24], the TERS results tend to have stronger A_{1g} mode, which may originate from the large vertical component of the electric field ($E_{\perp}$) inside the gap.

One spectral feature that we observed was the selective excitation of the A_{1g} mode in the RE-TERS spectrum compared to the far-field confocal measurement (**Figure 5.7**). In the RE configuration (**Figure 5.7**), the *s*-pol laser was focused on the AgNC excited SPPs ($\overrightarrow{k_{sp}}$) in the AgNW and propagated towards its tapered tip, where they were further compressed at the ~1 nm gap between the AgNW tip apex and the gold substrate. In this small gap, the concentrated electric field have two components, one normal ($E_{\perp}$) to the substrate that selectively drive the out-of-plane A_{1g} vibration in MoS_2, and the other parallel ($E_{\parallel}$) to the substrate that couples more strongly to the in-plane E_{2g}^1 vibration. According to the numerical simulation (**Figure 5.7 c-d**), $E_{\perp}$ is about one order of magnitude stronger than $E_{\parallel}$, giving rise to the strongly enhanced out-of-plane A_{1g} mode.

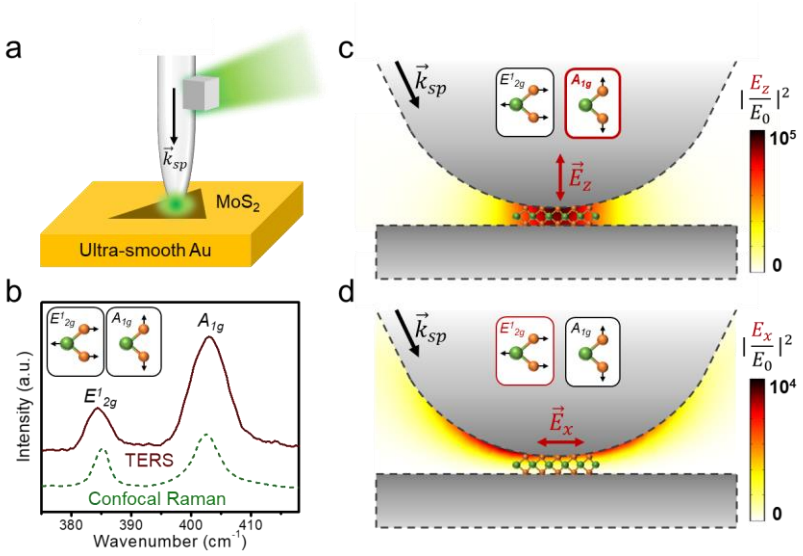

Figure 5.7 Raman mode selectivity of RE-TERS. **a,** Close-up schematic illustrating the remote-excitation scheme. The black arrow shows the direction of SPPs prorogation along the AgNW upon excitation of the incident laser on the AgNC. **b,** Comparison of the MoS_2 Raman spectra measured with RE-TERS vs. conventional confocal Raman. The RE-TERS spectrum features a larger $I_{A_{1g}}$ to $I_{E^1_{2g}}$ ratio, indicating the selectivity towards the A_{1g} peak. **c** and **d,** Numerical simulations show the strength and spatial distribution of the E-field components that are perpendicular ($E_\perp$, **c**) and parallel ($E_\parallel$, **d**) to the substrate at the tip apex. The $E_\perp$ component selectively drives the out-of-plane A_{1g} vibration, whereas the $E_\parallel$ drives the in-plane E^1_{2g} vibration more effectively.

5.4 RE-TERS mapping image of the single-walled CNT supported on ultra-smooth gold substrate: result and discussion

To determine the spatial resolution of RE-TERS in our experimental condition, we acquired high-resolution AFM-TERS images on a single-walled carbon nanotube (SW-CNT) sample, prepared by spraying SW-CNTs solution on an ultra-smooth gold substrate (detailed in Supporting Information), with a step precision of 4 nm as shown in **Figure 5.8**. As depicted by a representative spectrum (**Figure 5.8 a inset**), typical SW-CNT features including scattered D-band, strong G-band, and 2D-band are observed. The spectroscopic images at these bands are illustrated in **Figure 5.8 b**, **d** and **f**, respectively. It is worth noting

that the G-band intensity mapping has relatively stable signals along the CNT throughout the scanning. Such signal stability may benefit from the separation of the light coupling region at the AgNC and the Raman excitation region at tip apex, which generates a

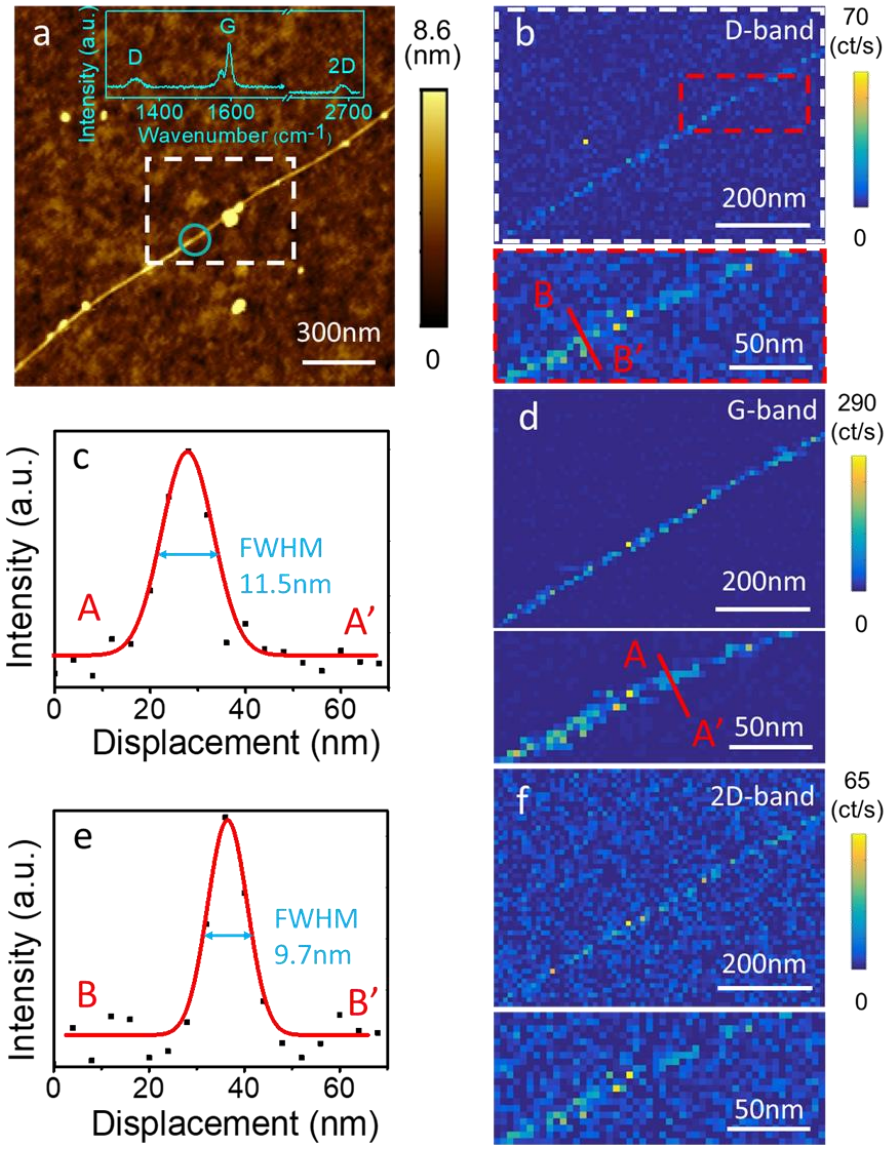

Figure 5.8 The RE-TERS mapping of single-walled CNTs, sprayed on an ultra-smooth Au substrate. **a,** AFM morphology imaging. **b,** D-band, **d,** G-band, and **f,** 2D-band intensity images. Spatial steps are 10nm for top images and 4 nm for the zoom-in at bottom **c** and **e,** line cross-section of the marked regions in **d** and **b**. For all TERS mapping, Excitation: 532nm, 0.1W at sample surface. Integration time = 1s.

relatively stable plasmonic hotspot. Meanwhile in a conventional gap-mode TERS, the gap-SPP coupling efficiency at the tip apex is influenced by the optical index of the sample, leading to an unstable TERS signal. As shown in **Figure 5.8 c** and **e**, a 10 nm resolution can be achieved on the G-band and D-band, which is close to the instrumental limit.

5.5 Conclusions

In summary, using AgNCs with proper size as an efficient plasmonic antenna to convert the excitation laser beam into the surface plasmon polaritons on a sharp-tip AgNW waveguide, we have demonstrated the remote-excitation of tip-enhanced Raman spectroscopy with high TERS contrast (up to 100) and fine spatial resolution (41nm). We mapped the Raman scattering variation within a MoS_2 flake, which reveals the strain distribution stored during the transfer process. The RE-TERS probes can be fabricated through a facile, robust and reproducible method, which requires only economical benchtop techniques. This polarization-insensitive antenna design allows the choosing of laser polarization that has weak interaction with the sample substrate for the further reduction of background noise. We expect that the remote-excitation plasmonic probe offers new routes for applications in disciplines where high resolution and sensitivities are needed, for example, in near-field scanning optical imaging and sensing.

5.6 References

1. Liu, Z.; Amani, M.; Najmaei, S.; Xu, Q.; Zou, X. L.; Zhou, W.; Yu, T.; Qiu, C. Y.; Birdwell, A. G.; Crowne, F. J.; Vajtai, R.; Yakobson, B. I.; Xia, Z. H.; Dubey, M.; Ajayan, P. M.; Lou, J. *Nat Commun* **2014,** 5, 5246.

2. Kazemi-Zanjani, N.; Kergrene, E.; Liu, L.; Sham, T.-K.; Lagugné-Labarthet, F. *Sensors* **2013,** 13, (10), 12744.

3. Hermann, P.; Hecker, M.; Chumakov, D.; Weisheit, M.; Rinderknecht, J.; Shelaev, A.; Dorozhkin, P.; Eng, L. M. *Ultramicroscopy* **2011,** 111, (11), 1630-1635.

4. Tarun, A.; Hayazawa, N.; Motohashi, M.; Kawata, S. *Review of Scientific Instruments* **2008,** 79, (1), 013706.

5. Norihiko, H.; Masashi, M.; Yuika, S.; Hidekazu, I.; Atsushi, O.; Taro, I.; Prabhat, V.; Satoshi, K. *Journal of Raman Spectroscopy* **2007,** 38, (6), 684-696.

6. Saito, Y.; Motohashi, M.; Hayazawa, N.; Iyoki, M.; Kawata, S. *Appl Phys Lett* **2006,** 88, (14), 143109.

7. Pozzi, E. A.; Goubert, G.; Chiang, N.; Jiang, N.; Chapman, C. T.; McAnally, M. O.; Henry, A.-I.; Seideman, T.; Schatz, G. C.; Hersam, M. C.; Duyne, R. P. V. *Chemical Reviews* **2017,** 117, (7), 4961-4982.

8. Lloyd, D.; Liu, X.; Christopher, J. W.; Cantley, L.; Wadehra, A.; Kim, B. L.; Goldberg, B. B.; Swan, A. K.; Bunch, J. S. *Nano Letters* **2016,** 16, (9), 5836-5841.

9. He, K.; Poole, C.; Mak, K. F.; Shan, J. *Nano Letters* **2013,** 13, (6), 2931-2936.

10. Jariwala, D.; Sangwan, V. K.; Lauhon, L. J.; Marks, T. J.; Hersam, M. C. *ACS Nano* **2014,** 8, (2), 1102-1120.

11. Rahaman, M.; Rodriguez, R. D.; Plechinger, G.; Moras, S.; Schüller, C.; Korn, T.; Zahn, D. R. T. *Nano Letters* **2017,** 17, (10), 6027-6033.

12. Milekhin, A. G.; Rahaman, M.; Rodyakina, E. E.; Latyshev, A. V.; Dzhagan, V. M.; Zahn, D. R. T. *Nanoscale* **2018,** 10, (6), 2755-2763.

13. van der Zande, A. M.; Huang, P. Y.; Chenet, D. A.; Berkelbach, T. C.; You, Y.; Lee, G.-H.; Heinz, T. F.; Reichman, D. R.; Muller, D. A.; Hone, J. C. *Nature Materials* **2013,** 12, 554.

14. Nagpal, P.; Lindquist, N. C.; Oh, S.-H.; Norris, D. J. *Science* **2009,** 325, (5940), 594.

15. Ma, X.; Liu, Q.; Xu, D.; Zhu, Y.; Kim, S.; Cui, Y.; Zhong, L.; Liu, M. *Nano Letters* **2017,** 17, (11), 6961-6967.

16. Wakabayashi, N.; Smith, H. G.; Nicklow, R. M. *Physical Review B* **1975,** 12, (2), 659-663.

17. Zhang, W.; Cui; Yeo, B.-S.; Schmid, T.; Hafner, C.; Zenobi, R. *Nano Letters* **2007,** 7, (5), 1401-1405.

18. Lee, C.; Yan, H.; Brus, L. E.; Heinz, T. F.; Hone, J.; Ryu, S. *ACS Nano* **2010,** 4, (5), 2695-2700.

19. Chen, S.-Y.; Zheng, C.; Fuhrer, M. S.; Yan, J. *Nano Letters* **2015,** 15, (4), 2526-2532.

20. Carvalho, B. R.; Malard, L. M.; Alves, J. M.; Fantini, C.; Pimenta, M. A. *Physical Review Letters* **2015,** 114, (13), 136403.

21. Rahaman, M.; Rodriguez, R. D.; Plechinger, G.; Moras, S.; Schüller, C.; Korn, T.; Zahn, D. R. *Nano letters* **2017,** 17, (10), 6027-6033.

22. Conley, H. J.; Wang, B.; Ziegler, J. I.; Haglund, R. F.; Pantelides, S. T.; Bolotin, K. I. *Nano Letters* **2013,** 13, (8), 3626-3630.

23. Zhou, K. G.; Withers, F.; Cao, Y.; Hu, S.; Yu, G. L.; Casiraghi, C. *Acs Nano* **2014,** 8, (10), 9914-9924.

24. Li, H.; Zhang, Q.; Yap, C. C. R.; Tay, B. K.; Edwin, T. H. T.; Olivier, A.; Baillargeat, D. *Advanced Functional Materials* **2012,** 22, (7), 1385-1390.

6. Conclusion

The ultra-sharp tip AgNWs have been synthesized and attached on conventional AFM cantilever for high-aspect-ratio (HAR) and high-resolution (HR) AFM. A single walled carbon nanotube (SWCNT) has been used as a reverse probe to test the high resolution of the probe and a 6nm lateral resolution and sub-1 nm horizontal resolution have been proved. A PMMA patterned deep trench grating sample has been used to test the high-aspect-ratio and larger than 7:1 HAR has been demonstrated. In addition, a AgNC has been attached on side of the AgNW of the probe, a remote-excited TERS probe has been fabricated and achieved. By separating the excited point and Raman scattered point, large TERS contrast (more than 100) has been achieved due to the largely suppressed background Raman signal. Besides of those works, the water-assisted clean stamp PDMS transfer has been developed. Using this method, we prepared graphene-based transistors with low charge-neutral concentration (3×10^{10} cm^{-2}) and high carrier mobility (up to 48 820 cm^2 V^{-1} s^{-1} at room temperature with SiO_2 supported, which is keeping the world record) and heterostructure optoelectronics with high operation speed.